Comparison of the Reactivity of Various Mn-Oxides with Cr^{III}_{aq}: Microscopic and Spectroscopic Observations of Dissolution, Cr-sorption and Cr and Mn Redox Interactions

Robert M. Weaver

Dissertation submitted to the faculty of the Virginia Polytechnic Institute and State University in partial fulfillment of the requirements for the degree of

Doctor of Philosophy in Geological Sciences

Committee

Michael F. Hochella, Jr., Chair
David F. Cox
Gerald V. Gibbs
Jeffery E. Post
J. Donald Rimstidt

September 19, 2001
Blacksburg, Virginia

Keywords: Manganese oxide, chromium, reduction, oxidation, microscopy, spectroscopy, AFM, FESEM, XPS

Abstract- Chapter 1

Dynamic Processes Occurring at the Cr^{III}_{aq} – Manganite (γ-MnOOH) Interface: Simultaneous Adsorption, Microprecipitation, Oxidation/Reduction and Dissolution

Robert M. Weaver

The complex interaction between Cr^{III}_{aq} and manganite (γ-MnOOH) was systematically studied at room temperature over a pH range of 3 to 6, and within a concentration range of 10^{-4} to 10^{-2} M $CrOH^{2+}_{aq}$. Solution compositional changes during batch reactions were characterized by ICP and UVvis. The manganites were characterized before and after reaction with XPS, SEM, high-resolution FESEM, and EDS analysis. Fluid-cell AFM was used to follow these metal-mineral interactions in situ. The reactions are characterized by 1) sorption of Cr^{III} and the surface-catalyzed microprecipitation of Cr^{III}-hydroxy hydrate on manganite surfaces, 2) the acidic dissolution of the manganite, and 3) the simultaneous reductive dissolution of manganite coupled with the oxidation of Cr^{III}_{aq} to highly toxic Cr^{VI}_{aq}. Cr^{III}-hydroxy hydrate was shown to precipitate on the manganite surface while still undersaturated in bulk solution. The rate of manganite dissolution increased with decreasing pH due both to faster acid-promoted and Mn-reduction-promoted dissolution. Due to direct redox coupling with Mn reduction, Cr oxidation was most rapid in the lower pH range. Neither Mn^{II} nor Cr^{VI} were ever detected on manganite surfaces, even at the maximum rate of their generation. At the highest pH's of this study, Cr^{III}_{aq} was effectively removed from solution to form Cr^{III}-hydroxy hydrate on manganite surfaces and in the bulk solution, and manganite dissolution and Cr^{VI}_{aq} generation were minimized. All interface reactions described above were heterogeneous across the manganite surfaces. This heterogeneity is a direct result of the heterogeneous semiconducting nature of natural manganite crystals, and is also an expression of the proximity effect, whereby redox processes on semiconducting surfaces are not limited to next nearest neighbor sites.

Abstract- Chapter 2

Comparison of the Reactivity of Various Mn-Oxides with Cr^{III}_{aq}: Microscopic and Spectroscopic Observations of Dissolution, Cr-sorption and Cr and Mn Redox Interactions

Robert M. Weaver

The interaction between Cr^{III}_{aq} and seven different Mn-oxides (6 monomineralic, 1 synthetic) has been observed in pH 4.4 HNO_3 and pH 4.4 ~10^{-4} M Cr^{III}_{aq} solutions. For each mineral-solution interaction, the aqueous chemical concentrations (e.g. $[Mn]_{aq}$, $[Cr]_{aq}$, $[Cr^{VI}_{aq}]$) were measured with time. Reacted samples were examined by XPS to determine if, and to what extent, the surface chemical states of Cr, Mn and O had changed. Microscopic observations of the reacted surfaces were obtained using AFM and high-resolution, low-voltage FESEM. The solubility of the Mn-oxides in the acidic, non-Cr bearing solutions varied inversely with the average Mn valence, but did not show systematic behavior with respect to the mineral structure type (e.g. tunnel, layer, framework). This trend was interpreted as resulting from the relative ability of an adsorbed proton to polarize surface Mn-O bonds, with the polarizability being in the order Mn^{2+}-O > Mn^{3+}-O > Mn^{4+}-O. For samples reacted with Cr^{III}_{aq}, the rate and extent of reductive dissolution was always greater than for acidic dissolution during the initial time period. The measured ratios of the $[Mn]_{aq}$: $[Cr^{VI}]_{aq}$ were approximately in agreement with the values expected from the proposed stoichiometric reactions. Cr-uptake was observed to occur in undersaturated solutions as a result of adsorption, absorption and surface catalyzed precipitation. The chromium as detected by XPS was predominately Cr^{III}, however pyrolusite contained both Cr^{III} and Cr^{VI}. Previous studies have implicated a chromium surface precipitate to be responsible for the cessation of the Cr^{III}_{aq} oxidation reaction. Our surface sensitive FESEM and AFM observations tend to suggest that Cr-uptake is by isolated site binding, very small (<30 nm) surface clusters or monolayer scale films. Cr-uptake was followed by slow Cr-release on several of the solids (particularly the layered solids) after a substantial portion of the total aqueous Cr had been converted to Cr^{VI}_{aq}.

The oxidizing ability of the different Mn-oxides for Cr^{III}_{aq} is evaluated with regards to the energy level of the redox couple (i.e. the redox potential) as compared with the Fermi energy level of the Mn-oxide. Although these energies were calculated rather than directly measured, the results indicate that electrons originating from adsorbed Cr^{III} ions may be transferred into the conduction band or more likely, into available surface states. The presence of an initial limited quantity of electron accepting surface states likely explains the observation of a rapid initial Cr^{III}-oxidation followed by much slower oxidation. The Mn-oxides that exhibited the greatest and longest lasting Cr^{III}-oxidizing power were the Mn-oxides containing Mn^{3+}, and in particular those containing Mn^{3+} and Mn^{2+}. It is believed that the combined presence of a reducible Mn ion (e.g. Mn^{3+}) and a highly soluble Mn^{2+} ion facilitates a sustained Cr^{III}-oxidation reaction because fresh surface is exposed during the reaction.

Acknowledgements

There are many people I owe a deep debt of gratitude for their efforts in helping to make this day possible. Most especially though I would like to thank my bride to be, Christine, for all of the love she has given to me over the years, always understanding the purpose of the long hours that have kept me away from home. The most exciting prospect of completing my dissertation has been the knowledge that I will be able to spend more time with her.

I would also like to especially thank my advisor, Mike Hochella. Mike has given me the great gift of freedom of choice in defining, designing and implementing my research, while at the same time always being available to provide insightful advice and guidance. Through his style of advisement Mike has allowed me to develop into an independent scientist and this has given me a great deal of confidence as I enter into my professional career. I would also like to thank the other members of my committee, Dave Cox, Jerry Gibbs, Jeff Post, Paul Ribbe and Don Rimstidt as well as Don Bloss. Each of these scientists have through their own very successful careers, provided me with a standard of excellent which to strive. It is also my great pleasure to acknowledge the many past and present members of our excellent research group, Russ, Udo, Barry, Tracy, Jeanne, Treavor, Steven, Andy, Erin, Eric, John, Kevin, Jodi, and Chris from who I have learned a great deal and shared four years of enjoyable experiences, and hopefully many more.

This research would also certainly not have been possible without abundant support from the faculty and staff of this department, led wisely by our chairman, Cahit Coruh. I would like to thank Bob Bodnar, Jim Craig, Mike Kowaleski, Don Rimstidt and Bob Tracy for providing me access to their analytical facilities, I thank all of the ladies in the main office, Linda, Connie, Mary and Carolyn for keeping me on track with all of my academic and financial needs, Susan Enksson for providing mineral samples, Mark Fortney for sharing with me his knowledge of photography, Mark Lemon and Eric Wonderley for maintaining my computers and Dan Smith for his skillful machining. I would also like to acknowledge Eugene Ilton, Steve McCartney and Frank Cromer for their help with XPS and FESEM measurements.

Table of Contents

Table of Figures

Chapter 1:

Chapter 2:

Table of Tables

Chapter 1:

Chapter 2:

CHAPTER 1: Dynamic Processes Occurring at the Cr^{III}_{aq} - Manganite (γ-MnOOH) Interface: Simultaneous Adsorption, Microprecipitation, Oxidation/Reduction and Dissolution

Abstract

The complex interaction between Cr^{III}_{aq} and manganite (γ-MnOOH) was systematically studied at room temperature over a pH range of 3 to 6, and within a concentration range of 10^{-4} to 10^{-2} M $CrOH^{2+}_{aq}$. Solution compositional changes during batch reactions were characterized by ICP and UVvis. The manganites were characterized before and after reaction with XPS, SEM, high-resolution FESEM, and EDS analysis. Fluid-cell AFM was used to follow these metal-mineral interactions in situ. The reactions are characterized by 1) sorption of Cr^{III} and the surface-catalyzed microprecipitation of Cr^{III}-hydroxy hydrate on manganite surfaces, 2) the acidic dissolution of the manganite, and 3) the simultaneous reductive dissolution of manganite coupled with the oxidation of Cr^{III}_{aq} to highly toxic Cr^{VI}_{aq}. Cr^{III}-hydroxy hydrate was shown to precipitate on the manganite surface while still undersaturated in bulk solution. The rate of manganite dissolution increased with decreasing pH due both to faster acid-promoted and Mn-reduction-promoted dissolution. Due to direct redox coupling with Mn reduction, Cr oxidation was most rapid in the lower pH range. Neither Mn^{II} nor Cr^{VI} were ever detected on manganite surfaces, even at the maximum rate of their generation. At the highest pH's of this study, Cr^{III}_{aq} was effectively removed from solution to form Cr^{III}-hydroxy hydrate on manganite surfaces and in the bulk solution, and manganite dissolution and Cr^{VI}_{aq} generation were minimized. All interface reactions described above were heterogeneous across the manganite surfaces. This heterogeneity is a direct result of the heterogeneous semiconducting nature of natural manganite crystals, and is also an expression of the proximity effect, whereby redox processes on semiconducting surfaces are not limited to next nearest neighbor sites.

1. INTRODUCTION

In natural environments manganese oxides are frequently recognized for their extraordinary sorption capacity and strong oxidizing ability (McKenzie, 1967; 1980; Murray et al., 1968; Chao and Anderson, 1974; Means et al., 1978; Burns and Burns, 1979; Murray and Dillard, 1979; Dillard et al., 1981; Hem et al., 1989; Fendorf et al., 1992). In addition, Mn-oxides have repeatedly been shown to be the only naturally occurring, inorganic phases capable of oxidizing Cr^{III}_{aq} (e.g. $CrOH^{2+}_{aq}$) to Cr^{VI}_{aq} species (e.g. $HCrO_4^-$, chromate) (Gray and Malati, 1979; Amacher and Baker, 1982; Eary and Rai, 1987; Fendorf and Zasoski, 1992). The potential for Cr^{III}_{aq} oxidation by Mn-oxides is of great concern not only because chromium is the most common, redox-active inorganic groundwater contaminant in the United States and several other industrialized countries, but Cr^{VI}_{aq} is more labile than Cr^{III}_{aq} and is carcinogenic even at low concentrations (e.g. < 50 ppb, Nriagu et al., 1988; Kavanaugh, 1994).

The interaction between Cr^{III}_{aq} and Mn-oxides is complex not only because chromium uptake and oxidation occurs, but also because depending on the solution conditions, the Mn-oxide surface undergoes simultaneous reductive dissolution and acidic dissolution. Previous studies in this system have focused on Cr^{III}_{aq} oxidation kinetics by synthetic pyrolusite (β-MnO_2) (Eary and Rai, 1987), synthetic manganite (γ-MnOOH) (Johnson and Xyla, 1991), synthetic birnessite (δ-MnO_2) (Fendorf and Zasoski, 1992; Chung et al., 1994; Chung, 1998; Silvester 1995), synthetic hausmannite (Mn_3O_4) and synthetic bixbyite (Mn_2O_3) (Rophael and Boulis, 1982; Malati and Rophael, 1999). Other Cr^{III}_{aq}-Mn-oxide studies have investigated: 1) the sorption and oxidation of Cr^{III}_{aq} with the concomitant solid state reduction of synthetic birnessite studied with X-ray photoelectron spectroscopy (XPS) (Banerjee and Nesbitt, 1999); 2) bulk atomic structural changes (e.g. bond length and angle) of synthetic birnessite accompanying reaction with Cr^{III}_{aq} studied by extended X-ray absorption fine structure (EXAFS) and X-ray absorption near edge spectroscopy (XANES) (Manceau and Charlet, 1990; Manceau and Charlet, 1992) and, 3) Cr^{III}_{aq} oxidation by synthetic δ-MnO_2 as elucidated by high resolution transmission electron microscopy (HRTEM), electron energy loss spectroscopy (EELS) and energy dispersive spectroscopy (EDS) (Fendorf et al., 1992).

Even with this vast base of experimental observations, in-situ microscopic observations at the Cr^{III}_{aq}–Mn-oxide interface are not available. Considering this gap, it was our primary goal to

obtain such observations of the surface reactions. Of near equal importance was the need to measure how the composition of the Mn-oxide surface and the contacting aqueous solution changed during the reaction, and to do this using natural, not synthetic, crystals. We chose to study Cr^{III}_{aq}-manganite interactions because manganite, like other Mn^{3+}-oxides, such as feitknecktite (β-MnOOH) and hausmannite (Mn_3O_4), is a common intermediate product of Mn^{2+}_{aq} oxidation or $MnO_{\sim 2(s)}$ disproportionation (Hem, 1981; Hem et al., 1982; Murray et al., 1985; Lind, 1988; Junta and Hochella, 1994). Manganite was also chosen because it is one of the few Mn-oxides that naturally forms relatively large, cleavable crystals suitable for our instrumental methods.

To study this complex interaction, manganite cleavage surfaces and powders were reacted with Cr^{III}_{aq}, and the aqueous and solid products were analyzed using microscopies (atomic force microscopy (AFM), scanning electron microscopy (SEM)) and surface-sensitive and bulk spectroscopies (XPS, EDS, inductively coupled plasma spectroscopy (ICP) and ultraviolet-visible spectrophotometry (UVvis)). Fluid-cell AFM was used to observe the uptake of Cr and the dissolution of manganite in-situ. The reacted surfaces were also examined using field-emission SEM (FESEM) at high resolution and low accelerating voltage, without applying a conductive coating. The bulk solution experiments were not intended to provide an exhaustive study of Cr^{III}_{aq} oxidation and manganite dissolution kinetics, but instead they provide background data to compliment our microscale AFM, SEM and XPS experiments. Finally, the local electronic behavior of the manganite cleavage surfaces before reaction were studied with scanning tunneling microscopy (STM).

Our experiments were conducted over a range of aqueous conditions for which the activity of Cr^{III}_{aq} was controlled primarily by the equilibrium between $CrOH^{2+}_{aq}$ and $Cr(OH)_3 \cdot 3H_2O_{(s)}$. This stability was studied in detail by Rai et al. (1987) and is generally described by Equation 1 and Figure 1

$$CrOH^{2+}_{aq} + 5H_2O = Cr(OH)_3 \cdot 3H_2O_{(s)} + 2H^+ \qquad \log K = -5.78 \qquad (1)$$

(Note that, although Rai et al. (1987) suggested that the Cr precipitate was amorphous $Cr(OH)_3$, we have found this phase to be crystalline $Cr(OH)_3.3H_2O$; see section 3.1 of this article). The points plotted in Figure 1 show the solution conditions we employed in each of our experiments.

As can be seen, with the exception of the one set of experiments performed in 10^{-2} M Cr^{III}_{aq}, all of the results presented were performed in 10^{-3} M or 10^{-4} M $CrOH^{2+}_{aq}$ and over a pH of 3 to 6. Under these conditions the saturation index (SI) for $Cr(OH)_3 \cdot 3H_2O$ ranges from –0.46 to 0.14. This SI range corresponds to 6000x undersaturated to 600x oversaturated with respect to $Cr(OH)_3 \cdot 3H_2O$.

2. METHODS AND MATERIALS

2.1 Manganite characterization and aqueous solutions

The manganite (γ-MnOOH) samples used in this study were from Ilfeld, Germany and Pawling Mine, NY (Virginia Polytechnic Institute Museum #R706 and #Ma5). Structural and chemical characterization with X-ray diffraction (XRD), XPS, EDS and wavelength dispersive spectroscopy (WDS) (data not presented) confirmed the manganites to be highly crystalline with minor amounts (<1%) of Ca and Fe. Trace element chemistry was not investigated.

Samples for AFM, SEM and STM observations/experiments were cleaved from larger manganite crystals using a pestle or scalpel. The resulting (010) and (110) surfaces were locally optically flat and often exhibited twinning. Although the surfaces were stable in air (as observed by AFM and XPS), it was standard practice to use freshly exposed surfaces (i.e. < 1 day).

Fine-grained manganite was prepared by grinding samples in a McCrone micronizing mill (crushing action is primarily by shear stress) for 10 minutes. XRD patterns of the ground powder showed no loss in crystallinity. The surface area of the powder, as measured by N_2 BET, was 8.9 ±0.1 m^2/g. A PZC of 5.4 ±0.2 was determined from surface titrations conducted at five ionic strengths ranging from ~0 to 0.1M $NaNO_3$.

All chemicals were of reagent grade or higher and solutions were prepared from distilled, deionized water obtained from a Millipore Synthesis A10 water system (18MΩ, 1 ppb total organic carbon (TOC), UV light treated, ultrafiltration membrane, 0.2 μm filtered). All glassware and high-density polyethylene (HDPE) containers were rinsed with 0.01M HNO_3 and water before use. Standardized Cr^{III}_{aq} solutions were prepared fresh (<12 hours) for each experiment. All experiments were conducted at room temperature (23 ± 2°C) and solutions were

assumed to be in equilibrium with air. Previous work has shown that Cr^{III}_{aq} is not significantly oxidized by O_2 even after one month (Schroeder and Lee, 1975; Van Der Weijden and Reith, 1982; Eary and Rai, 1987).

2.2 Batch Experiments for Aqueous Chemical Analysis by ICP and UV-Vis

Reactions were performed in parafilm covered, 500 mL HDPE containers in solutions held at a constant pH of 3, 4, 5, or 6 (±0.02) by automatic titration (Radiometer ABU 901 autoburette) of 0.1 M HNO_3. Solutions were stirred vigorously (300 rpm) by an overhead Teflon paddle. Immediately before reaction, an aliquot of the manganite suspension and the Cr^{III}_{aq} stock solution was sampled to measure the initial concentrations of manganese and chromium. Reactions were initiated by adding pH adjusted, 10^{-3} M $Cr(NO_3)_3 \cdot 6H_2O$ (17.77 mL) to 160 mL of the stirred preequilibrated manganite suspension. The final reacting solutions contained 10^{-4} M Cr^{III}_{aq}, 0.005M $NaNO_3$ and 0.45g/L manganite (~4.0 m^2/L). Samples were periodically extracted using a HDPE syringe, filtered through 0.2 μm nitrocellulose, analyzed for Cr^{VI}_{aq} with UVvis and then stored in capped HDPE containers awaiting ICP analysis.

Additional control experiments were performed to measure the extent of: 1) sorption of chromium to the HDPE surfaces; 2) acidic dissolution of manganite; and 3) Cr^{III}_{aq} oxidation by Mn^{III}_{aq} in the absence of manganite. The extent of chromium uptake by HDPE over a 24 hour period was found to be negligible. For the acidic dissolution study, the reacting solutions contained 0.005M $NaNO_3$, 0.45g γ-MnOOH/L, were stirred vigorously (300 rpm) and held at pH 3, 3.5, 4, 5 and 6 ±0.05 by automatic addition of 0.1 N HNO_3. Samples were collected after approximately 10 min., 1 hr. and 8 hr. of reaction, centrifuged (2500 rpm) and filtered through 0.2 μm nitrocellulose. To measure the extent of Cr^{III}_{aq} oxidation by Mn^{III}_{aq} a standardized Mn^{III}_{aq} stock solution was prepared by acidically dissolving manganite in 0.1 N HNO_3. The solution obtained was then titrated with NaOH to pH 3, centrifuged (3500 rpm), filtered two times through 0.1 μm nitrocellulose and Mn^T was measured by ICP. The resulting Mn^{III}_{aq} solution had an absorption maximum at 300 nm. The amount of chromate produced by reaction of this Mn^{III}_{aq} solution (0.5 mL, 9 x 10^{-4} M) with Cr^{III}_{aq} (0.5 mL, 3 x 10^{-4} M) at pH 3 for 32 hr. was found to be less than 2 x 10^{-7} M Cr^{VI}_{aq} (i.e. < 1%). At these Cr^{III}_{aq} and Mn^{III}_{aq} concentrations, Cr^{VI}_{aq} was only

produced at pH >3.5 when it was evident that Mn-oxide precipitation was occurring. For this reason it was concluded that the amount of Cr^{VI}_{aq} produced by the direct reaction between Mn^{III}_{aq} and Cr^{III}_{aq} was negligible (i.e. < 1%) compared to the amount produced by direct reaction at the Mn-oxide surface.

2.3 Batch Experiments for Surface Analysis by XPS

Manganite samples for XPS analysis were recovered from their respective reaction vessels by centrifugation and decantation rather than filtration, to avoid contamination and allow for near complete recovery of the solids. For these reasons reactions were carried out in 50 mL HDPE centrifuge tubes which were rotated end over end (~60 rpm). The reacting solution contained 0.45 g γ-MnOOH/L (~4.0 m^2/L), 10^{-4} M $CrCl_3 \cdot 6H_2O$ and 0.005 M NaCl. The manganite powder was preequilibrated in 0.005 M NaCl electrolyte at pH 4.5 for 24 hr. Reactions were initiated by the addition of 10 mL of pH 4.5, 2 x 10^{-4} M Cr^{III}_{aq} and continued for 3 min., 30 min., 8 hr. and 20 hr. Solution pH was maintained by manual addition of 0.05 M HCl. For the 3 and 30 minute experiments the pH did not exceed 4.61 and for the 8- and 20 hr. experiments the pH did not exceed 4.73. Reactions were ended by centrifugation (2500 rpm) and decantation of the supernate. The manganite powder was then shaken for 20 sec. with 20 mL of pH 4.6 HCl, centrifuged and decanted. This rinsing process was performed five times after which the manganite was dried under low vacuum (10^{-5} Torr), dispersed onto a tin sheet with a razor, pressed and analyzed by XPS. The $Cr2p^{3/2}$ region was scanned first to minimize potential X-ray beam-induced reduction of Cr^{6+} (Halada and Clayton, 1991; Ilton et al., 1997).

2.4 In-situ Fluid-Cell AFM and ex-situ SEM Experiments

Manganite cleavage fragments were mounted on Al or glass discs using a carbon-based adhesive (AFM fluid-cell experiments) or reacted without mounting (SEM experiments) in a HDPE container with 20 mL of standardized Cr^{III}_{aq} solution. We attempted to remove submicron cleavage fragments adhering to the surface using a high velocity N_2 stream and/or sonification in pH 5.0 HNO_3. However, it was determined that these cleaning procedures were not entirely

effective and furthermore, that the particles did not significantly affect our observations. For this later reason, the surface cleaning steps were eventually deemed unnecessary. Prior to reaction, manganite surfaces were examined by Nomarski differential interference contrast (DIC) microscopy and AFM, to document surface features (e.g. microtopography, terrace roughness, twinning). Samples were then placed in the AFM fluid-cell or a HDPE container and reacted with Cr^{III}_{aq}.

For the AFM fluid-cell experiments, Corning vacuum grease was applied between the o-ring and the sample disc to prevent leaks and to minimize image distortion caused by friction between the o-ring and sample. When AFM images were not being obtained, the tip was lifted ~50 μm from the sample surface (to not influence the reaction) and solution flow was resumed. Solutions were pumped at a speed of ~0.4 mL/min (i.e. ~1 cell volume flush every 10 sec.) through Pt-cured silicone tubing. In most of the AFM fluid-cell experiments, the manganite was first exposed to a HCl or HNO_3 solution to observe the process of acidic dissolution. These observations allowed us to be confident that the solution was free of particulate contaminants that might be mistaken for $Cr(OH)_3 \cdot 3H_2O$ precipitates. After observing the manganite surface under exposure to acid, the feed solution was switched to a 10^{-3} or 10^{-4} M $CrOH^{2+}_{aq}$ solution and AFM imaging was resumed. Upon removal from the AFM, the sample was dried in a high velocity N_2 stream and analyzed by XPS, SEM and/or EDS. For XPS observations, the sample was remounted on a fresh aluminum or carbon-coated (e.g. HOPG, DAG) surface. This remounting allowed us to be certain that the Cr and Mn XPS signals were originating from the manganite with no contribution from the sample holder.

2.5 Scanning Probe Microscopy

AFM images were collected with a Digital Instruments Nanoscope IIIa Multimode Atomic Force Microscope, operating in either air or aqueous solution, and in contact or Tapping® mode (TMAFM). The XY scale was calibrated with a 1 μm standard and the Z scale was calibrated against the basal spacing of mica (i.e. 0.995 nm). AFM probes used have a Si tip (nominal radius ~20 nm) on a 100 μm SiN_3 cantilever. The acrylic AFM fluid-cell holds ~0.03-0.07 mL depending on the sample size and the degree of silicone o-ring compression (see Johnsson et al., 1991 for cell schematic).

A Digital Instruments scanning tunneling microscope (STM) was used to characterize the local electronic behavior of manganite. Although a wide range of bias voltages and setpoint currents were tried, and it was possible in some tip-sample approaches to establish a tunneling current, the current was too unstable during scanning for good surface imaging. The implications of this observation to surface reactivity are significant and will be discussed later.

2.6 Electron Microscopy and Spectroscopy

SEM images, EDS spectra and WDS spectra were collected using three different instruments: 1) a LEO 1550 FESEM with IXRF EDS, 2) a Camscan Series II SEM and, 3) a Cameca SX50 electron microprobe. Pertinent imaging conditions are reported in the figure captions. The FESEM images were collected at voltages as low as 1 kV with an 'in-lens' secondary electron detector. Under these conditions the lateral resolution and surface-sensitivity are superior due to enhancement of the SE_I signal (Goldstein, et al. 1992). SEM imaging was also performed by varying the accelerating voltage to obtain voltage contrast SEM images. Voltage contrast images showed the extent of heterogeneous electrical conduction in the sample, an important sample property discussed later.

2.7 X-Ray Photoelectron Spectroscopy

XPS spectra were collected with a Scienta ESCA-300 and a Perkin Elmer 5400. The Scienta XPS utilized monochromatic AlKα X-rays, generated at a power of 1.9 kW, and had an analysis area of 1.0 cm x 300 μm. Photoelectrons were collected from a 90^o take off angle and energy analyzed using a pass energy of 150 eV. Survey scans were collected with a 0.5 eV step size and narrow scans with a 0.1 or 0.05 eV step size. Because manganite is a wide band gap semiconductor, it was necessary to use a flood gun to neutralize the charge that developed on the sample during irradiation. XPS spectra collected with the Perkin Elmer XPS used nonmonochromatic AlKα X-rays and a spot size of either 1.1 mm^2 or a diameter of 600 μm. Survey and regional scans were collected with pass energies of 44.8 eV and 17.9 eV, respectively. Analyses were performed in both instruments at pressures of less than $4x10^{-8}$ Torr.

XPS spectra were charge referenced to adventitious carbon at 284.6 eV. Peak fitting of photolines was performed using a Shirley background correction and Voigt (Gaussian-Lorentzian) curve-fitting function.

2.8 UV-Vis Spectrophotometry

A Beckman Coulter DU640 spectrophotometer was used to record wavelength scans. Solutions were analyzed in a 1 cm path length, quartz or methacrylate cuvet. The measured absorbance for chromate was standardized against known concentrations of analytic grade Cr^{VI}_{aq}, adjusted to pH. Beer's Law behavior was observed for the concentration range measured (Buerge and Hug, 1999). A precision on replicate samples of ±12 ppb was assigned to all peaks.

2.9 Inductively Couple Plasma Spectroscopy

Aqueous concentrations for Cr and Mn were measured on a Spectro Analytical Instruments Inc., SpectroFlame ICP. Cr and Mn standards were prepared from Plasma-pure™ grade reagents diluted with the matrix used in each experiment. Reported ICP measurements are the average of three measurements. A precision of ±20 ppb was observed in replicate measurements.

3. RESULTS

3.1 Solution Compositions with Time and pH

The uptake and oxidation of chromium and the dissolution of manganite was observed over a 15 hour period and pH range from 3 to 6. Within the first several minutes of each reaction a substantial portion of the total chromium uptake had already occurred (Fig. 2). However, after an additional 30 minutes a small amount (0.2 to 3.9 %) of the chromium was released back into solution. In general, the amount of chromium removed from solution was greatest for the higher

pH experiments. For example, after 15 hours of reaction at pH 3 approximately 13% of the initial total aqueous chromium ($[Cr]^{T}_{aq}$) was removed from solution, whereas at pH 6, over the same 15 hour period, ~76% of the initial $[Cr]^{T}_{aq}$ was removed. The most substantial change in chromium uptake occurred between pH 5 and 6, when the solution became supersaturated with respect to $Cr(OH)_3 \cdot 3H_2O$ and bulk precipitation occurred. The bulk precipitate was identified by XRD, as $Cr(OH)_3 \cdot 3H_2O$ (JCPDS #16-817) in a separate experiment conducted at pH 6.5, 10^{-4} M Cr^{III}_{aq} in the absence of manganite. The solubility data of Eary and Rai (1987) were used to calculate that $Cr(OH)_3 \cdot 3H_2O_{(s)}$ saturation occurs at pH 4.9 for a 10^{-4} M $CrOH^{2+}$ solution (see Eqn. 1). Using this $Cr(OH)_3 \cdot 3H_2O_{(s)}$ stability data we can attribute, to at least a first approximation, chromium uptake at pH > 4.9 to $Cr(OH)_3 \cdot 3H_2O_{(s)}$ precipitation and at pH < 4.9 to chromium adsorption and/or surface catalyzed precipitation.

Accompanying the removal of chromium from solution is the oxidation of Cr^{III}_{aq} to Cr^{VI}_{aq}. The production of Cr^{VI}_{aq} is initially very rapid and nonlinear for all pH's, but eventually slows and approaches linearity (Fig. 3). The conversion is most efficient at lower pH's. For example, at pH 3, 90% of the initial $[Cr]^{T}_{aq}$ is oxidized to Cr^{VI}_{aq} within ~15 hours, whereas at pH 6, only 14% of the initial $[Cr]^{T}_{aq}$ was oxidized to Cr^{VI}_{aq} after 15 hours. By comparing the $[Cr^{VI}]_{aq}$ to that of $[Cr]^{T}_{aq}$ after 15 hr. of reaction at pH 3, it was found that the reaction at pH 3 had reached completion (i.e. $[Cr^{VI}]_{aq} = [Cr]^{T}_{aq}$ after 15 hr.) whereas, at pH 4, 5 and 6 after 15 hr. of reaction approximately 72%, 41% and 59% of the $[Cr]^{T}_{aq}$ occurs as Cr^{VI}_{aq}. The percentage at pH 6 increases to 59% due to $Cr(OH)_3 \cdot 3H_2O_{(s)}$ precipitation.

The amount of manganite dissolution by simultaneous reductive dissolution and acidic dissolution is greatest at pH 3 (Fig. 4). Figure 4 also shows the change in the total aqueous manganese, with time and pH, caused by acidic dissolution alone. It can be seen that at pH 3 the rate of acidic dissolution exceeds that for acidic plus reductive dissolution. However, at pH 4 the rate of acidic dissolution is less than the rate of acidic plus reductive dissolution. This behavior demonstrates that for pH's less than ~3.5, chromium inhibits the rate of manganite dissolution relative to chromium-free solutions. A similar inhibition of the dissolution rate by chromium was observed by Banerjee and Nesbitt (1999) for δ-MnO_2 at pH 4.6. However, Eary and Rai (1987) observed that for β-MnO_2 the rates of acidic dissolution and reductive plus acidic dissolution were approximately the same at pH 4, but the rate of reductive plus acidic dissolution was faster at pH 3. In Fig. 4, the reductive plus acidic dissolution curves have an initial period of

nonlinearity (recall, so did the chromate curves, Fig. 3), whereas the acidic dissolution curves are linear with time after just a few minutes. Comparing the results of Figs. 3 and 4 for the first 6 hours of reaction, the $[Mn]^{T}_{aq}$: $[Cr^{VI}]_{aq}$ ratio can be shown decrease with increasing pH, from 4.3 at pH 3, 3.7 at pH 4, 3.0 at pH 5 and 2.1 at pH 6. The significance of this ratio for judging changes in the overall reaction stoichiometry with pH and time are discussed later.

3.2 Surface Compositions with Time

XPS spectra obtained from manganite powders reacted with Cr^{III}_{aq} (Fig. 5) show an increase in surface bound chromium with reaction time, as was suggested by the solution data (see Fig. 2). The concentrations of surface chromium relative to surface manganese (as determined from ratios of $Cr2p^{3/2}$: $Mn2p^{3/2}$ photopeak areas) increases with reaction time up to the 8 hr. sample, then does not change for the sample reacted for 20 hr. This increase in surface bound chromium suggests that surface saturation with respect to chromium is reached in less than 8 hr. However, this disagrees with the solution data for $[Cr]^{T}_{aq}$ with time (Fig. 2) which suggests that at pH 4.5 Cr-uptake occurs throughout the reaction period. The reason for this discrepancy between the Cr-aqueous and Cr-solid concentration profiles is not known, but there are at least two possibilities; 1) Cr could be taken up on rough surfaces, not all portions of which are visible to the electron energy analyzer of the XPS instrument; and 2) the rinsing procedures used for the XPS samples, which could have removed some of the adsorbed Cr or $Cr(OH)_3 \cdot 3H_2O_{(s)}$ surface precipitate.

The oxidation state of surface bound chromium was determined to be Cr^{3+} based on three lines of XPS evidence: 1) the magnitude of the Cr2p spin orbit splitting is 9.8 ± 0.1 eV. Reported values for Cr2p splitting of Cr^{3+} compounds (e.g. Cr_2O_3, CrOOH and $Cr(OH)_3 \cdot 0.4H_2O$) are 9.7 - 9.8 eV, whereas splitting for Cr^{6+} compounds (e.g. CrO_3, Na_2CrO_4, $K_2Cr_2O_7$) are 9.2 - 9.3 eV (Ikemoto et al., 1976, Halada and Clayton, 1991); 2) the binding energy of the $Cr2p^{3/2}$ photopeak at 576.7 ± 0.1 eV is consistent with reported values for Cr_2O_3, CrOOH and $Cr(OH)_3 \cdot 0.4H_2O$ which range from 576.45 – 577.00 eV (Fig. 6). Compounds containing Cr^{6+} have binding energies of 578.3 – 579.8 eV, respectively (Banerjee and Nesbitt, 1999 and references therein for $Cr^{3+, 4+, 5+, 6+}$ binding energies); and 3) our raw data is in good agreement

with a $Cr2p^{3/2}$ peak modeled using the theoretical multiplet structure of the Cr^{3+} free ion calculated by Gupta and Sen (1974; 1975) (Fig. 6, Table 1).

Surface manganese was determined to be Mn^{3+} in all reacted samples, based on three lines of evidence: 1) the Mn3s multiplet splitting of 5.5 ± 0.1 eV observed for each reaction period is diagnostic of Mn^{3+} (Fig. 7). The multiplet splitting for Mn^{4+} and Mn^{2+} are 4.5 eV and 6.2 eV, respectively (Evans and Raftery, 1982; Junta and Hochella, 1994); 2) the agreement of the $Mn2p^{3/2}$ photopeak shape with a theoretical model $Mn2p^{3/2}$ photopeak generated using the Mn^{3+} multiplets (slightly modified) calculated by Gupta and Sen (1974; 1975) (Fig. 8, Table 1); and 3) the $Mn2p^{3/2}$ peak position at 641.4 ± 0.1 eV approximates that reported for other Mn^{3+}-oxides (641.7 - 641.9 eV). $Mn2p^{3/2}$ peak positions for $Mn^{4+}O_2$ range from 641.9 – 642.6 eV and Mn^{2+} peak positions range from 640.4 eV to 641.7 (Junta and Hochella, 1994; Banerjee and Nesbitt, 1999).

Oxygen (O1s) XPS spectra show that with increased reaction time, the manganite surface becomes more enriched in OH^- and H_2O relative to O^{2-} (Fig. 9). This increase in OH^- and H_2O correlates with the previously observed increase in chromium with reaction time (Fig. 5) and thus suggests that $Cr(OH)_3{\cdot}3H_2O$ is present at the surface. A control sample, reacted in pH 4.5 HCl for 30 minutes and no Cr^{III}_{aq}, still contained 1:1 (i.e. stoichiometric) quantities of O^{2-} and OH^- with a minor (~12%) amount of adsorbed water (see t = 0 in Fig. 9 and Table 1). This result strongly suggests that changes in the O1s spectra with time are attributable to reaction with aqueous chromium.

3.3 Microscopic Observations of Reacted Surfaces

AFM and SEM images of reacted surfaces indicated that both chromium uptake and manganite dissolution could occur over a range of solution conditions (e.g. pH, $Cr(OH)_3 \cdot 3H_2O_{(s)}$-saturation) and were spatially heterogeneous (Figs. 10 - 14). The images also showed that the extent of Cr-uptake and manganite dissolution were generally related to the degree of $Cr(OH)_3 \cdot 3H_2O$ saturation and pH, as would be expected given the solubility behaviors of $Cr(OH)_3 \cdot 3H_2O$ and manganite. Visual evidence of significant increases in the extent of Cr-uptake was commonly observed in these images when the $Cr(OH)_3 \cdot 3H_2O$ saturation index was

increased from –0.29 to 0.08 (Figs. 10, 11, 12). However, although the results of the batch reactor experiments demonstrated that minor Cr-uptake does occur at low $Cr(OH)_3 \cdot 3H_2O$ saturations (Fig 2), Cr-uptake was not commonly observed under these conditions in the AFM experiments. When Cr-precipitates were observed in undersaturated solutions (e.g. S.I. –0.29, pH 3.5 10^{-4} M Cr^{III}_{aq}), they formed immediately after exposure to Cr^{III}_{aq} and resembled those shown in Fig. 10b, measuring 20 - 80 nm wide and <1.5 nm high. Interestingly, there is no dissolution in this area, and no additional chromium uptake or release was observed over an additional 2 hr. period. At these conditions it was also common to see: 1) rapid homogeneous dissolution with no evidence of chromium binding; and 2) no change in the appearance of the surface.

Under solution conditions closer to $Cr(OH)_3 \cdot 3H_2O$ saturation (SI= -0.06, pH 4.5, 10^{-4} M Cr^{III}_{aq}) Cr-uptake is generally more commonly observed and manganite dissolution is less apparent (Fig. 11). After exposure to Cr^{III}_{aq} for 5 min (Fig. 11b), $Cr(OH)_3 \cdot 3H_2O$ precipitates measuring from 10 - 200 nm wide and 0.3 to 10 nm high are visible, as is fine-scale surface pitting. Similar observations of heterogeneous precipitation and dissolution are seen by FESEM on other samples (Figs. 11c,d). However, it is also apparent that much of the surface has undergone little to no change. Incidentally, the precipitates seen in Fig. 11c,d were barely visible at 15 kV or when viewed with the conventional Everhart-Thornley SE_{II} detector.

Figure 12 illustrates the degree of dissolution heterogeneity that was commonly seen in our experiments. The lower left area of Fig. 12a shows only a few dissolution pits, whereas the lower right area shows abundant pitting on the terraces and the upper central area (enlarged in Fig. 12b) shows extensive dissolution on the terraces and at step edges. There does not appear to be any microprecipitates in this area, but the 30kV accelerating voltage used for these images results in a low degree of surface sensitivity (Goldstein et al., 1992).

The AFM image sequence shown in Fig. 13 shows manganite dissolution and the development of microprecipitates within 4 min. of exposure to a pH 4.5, 10^{-2} M Cr^{III}_{aq} (SI= 0.08) solution. Dissolution pits are elongated along [001] and measure ~40 nm wide, ~150 nm long and ~1 nm deep. The dissolution pits are slightly wider and deeper along the step edge (see Fig. 13c), possibly due to defects generated here during cleavage. Also seen are new topographic highs (bright patches) corresponding to $Cr(OH)_3 \cdot 3H_2O$ precipitates measuring ~7 nm tall. The sample was then removed from the fluid-cell and reacted for 10 hr. in 20 mL of the same

solution, after which the sample was imaged by AFM in air (Fig. 13d). The surface is now covered by microprecipitates, the tallest measuring ~50 nm. XPS analyses of the manganites shown in Figs. 10, 11 and 13 showed small to undetectable quantities of chromium with a $Cr2p^{3/2}$ binding energy of 576.6 ± 0.1 eV, indicative of Cr^{3+}.

The acidic dissolution of manganite was found to be less spatially heterogeneous than dissolution in the presence of chromium (that is, reductive plus acidic dissolution). Figure 14 shows a series of AFM images obtained over a 1 hr. period during exposure to pH 3.5 HNO_3 in the absence of Cr^{III}_{aq}. Prior to reaction (Fig. 14a) the surface contains several steps bounding atomically flat terraces. Within 13 min of exposure the terraces become riddled with randomLy shaped, monolayer deep (~0.5 nm) dissolution pits (Fig. 14b). Dissolution was initially most rapid at the step edges as evidenced by the more expansive pits formed there. Although this seems to be the case, it is interesting to note that some sites along step edges (marked by arrows) undergo little dissolution. With continued reaction, dissolution proceeds primarily at step edges causing the existing pits to become broader and eventually coalesce (Fig. 14c, d). Tip enhanced dissolution during a previous 1 x 1 μm scan is evidenced in Fig. 14d by the 1 μm^2 area near the center of the image. Subsequent 5 μm and 10 μm images collected after Fig. 14d showed that tip- enhanced dissolution in the 2.5 μm scan region of Fig. 14d was minor.

4. DISCUSSION

4.1 Aqueous and surface chemistry

The changes observed in the composition of the aqueous solution (i.e. $[Cr]^{T}_{aq}$, $[Mn]^{T}_{aq}$, $[Cr^{VI}]_{aq}$; Figs. 2, 3, 4) are generally interpretable based on the solubility behaviors of $Cr(OH)_3 \cdot 3H_2O$ and manganite as a function of pH and redox state. While both manganite and $Cr(OH)_3 \cdot 3H_2O$ are solubilized under acidic conditions, manganite is solubilized by reduction and $Cr(OH)_3 \cdot 3H_2O$ is solubilized by oxidation. These differences and similarities in the solubility behaviors account for the observed trends in the concentrations of $Cr(OH)_3 \cdot 3H_2O_{(s)}$, Cr^{VI}_{aq}, Cr^{III}_{aq} and Mn^{T}_{aq}. With decreasing pH the rate of manganite dissolution increases due to

proton promoted dissolution (Eqn. 2) and also due to an increase in the rate of reductive dissolution (Eqn. 3). Although it is clear from our control experiments (see section 2.2) that Mn^{III}_{aq} is not a significant oxidant of Cr^{III}_{aq} when in the absence of manganite, Mn^{III}_{aq} may be capable of oxidizing Cr^{III}_{aq} to Cr^{VI}_{aq} when in the presence of manganite (Eqn. 4).

$$\gamma\text{-MnOOH} + 3H^{+} = Mn^{3+}_{aq} + 2H_2O \quad (2)$$

$$CrOH^{2+}_{aq} + 3\gamma\text{-MnOOH} = HCrO^{-}_{4\,aq} + 3\,Mn^{2+}_{aq} + 3OH^{-} \quad (3)$$

$$CrOH^{2+}_{aq} + 3Mn^{3+}_{aq} + 3OH^{-} + \gamma\text{-MnOOH} = HCrO_4^{-}{}_{aq} + 3Mn^{2+}_{aq} + 3H^{+} + \gamma\text{-MnOOH} \quad (4)$$

Slight to significant amounts of Cr-uptake occurred over the pH range studied. Our observations show that for conditions of $Cr(OH)_3 \cdot 3H_2O$ oversaturation, uptake is due to $Cr(OH)_3 \cdot 3H_2O$ precipitation (Eqn. 1). For undersaturated conditions Cr–uptake is due to Cr-adsorption (Eqn. 5), where'S' indicates surface site and/or surface catalyzed precipitation of $Cr(OH)_3 \cdot 3H_2O$.

$$CrOH^{2+}_{aq} + S\text{-MnOOH} = Cr^{3+}\text{-MnOOH} + OH^{-} \quad (5)$$

For a hypothetical reaction between manganite and Cr^{III}_{aq} in which equal amounts of aqueous manganese are produced by proton promoted and reductive dissolution, and assuming no Cr-uptake, a net reaction may be expressed by combining Eqn. 2 (times three) and Eqn. 3 (Eqn. 6). Under these specific conditions a $[Mn]^{T}_{aq} : [Cr^{VI}]_{aq}$ ratio of 6 is expected and $3Mn^{3+}_{aq}$ are produced.

$$CrOH^{2+}_{aq} + 6\gamma\text{-MnOOH} + 9H^{+} = HCrO^{-}_{4\,aq} + 3\,Mn^{3+}_{aq} + 3Mn^{2+}_{aq} + 3OH^{-} + 6H_2O \quad (6)$$

If we assume that in the presence of manganite each of the three Mn^{3+}_{aq} are reduced during the oxidation of $CrOH^{2+}_{aq}$ to produce $HCrO_4^-{}_{aq}$, then the $[Mn]^T_{aq} : [Cr^{VI}]_{aq}$ ratio would decrease to 3. In addition, given that Cr-uptake does occur and the rates of acidic dissolution and reductive dissolution are generally not equal, the $[Mn]^T_{aq} : [Cr^{VI}]_{aq}$ ratio would be interdependent on the extent of each of these reactions (Eqns. 1-5). At low pH (e.g. 3) the ratio would be greatest due to the increased rate of acidic dissolution. At higher pH (e.g. 6) where there is less manganite dissolution and Cr^{III}_{aq} oxidation competes with $Cr(OH)_3 \cdot 3H_2O$ precipitation, the ratio would likely decrease. This expected trend in the reaction stoichiometry with increasing pH was observed in our batch reactor experiments (Figs. 2, 3, 4). After ~6 hr. of reaction at pH 3, 4, 5 and 6, the $[Mn]^T_{aq} : [Cr^{VI}]_{aq}$ ratio decreased from greater than to less than 4 (4.4, 3.7, 3.1 and 2.1, respectively). Eary and Rai (1987) observed a similar trend in the $[Mn]^T_{aq} : [Cr^{VI}]_{aq}$ ratio which they ascribed, as we do, to these simultaneous reactions. However, other studies found their measured ratio of $[Mn]^T_{aq} : [Cr^{VI}]_{aq}$ to be in agreement with their proposed stoichiometric reactions, even at varied solution conditions (Amacher and Baker, 1982; Johnson and Xyla, 1991; Fendorf and Zasoski, 1992).

4.2 Cr-adsorption

Although not specifically addressed in this study, the driving force for Cr-adsorption on manganite is probably due to a specific (inner sphere) interaction. This is apparent from EXAFS studies on similar systems (Manceau and Charlet, 1992) and also because Cr^{3+} adsorption takes place even on positively charged surfaces. Considering manganite has a positive surface charge for pH < 5.2 (i.e. the PZC) it would be expected that the anionic chromate species ($HCrO_4^-$) formed during the oxidation of $CrOH^{2+}$ would be electrostatically bonded to the surface. However, chromate was not detected (by XPS) on the manganite surface; only Cr^{3+} was detected. The absence of bound chromate is explained by: 1) the much increased solubility of chromate relative to Cr^{III}_{aq} due to oxidative dissolution, which therefore disposes chromate to be predominately in an aqueous state, and 2) an absence of appropriate absorption sites (e.g. tunnel, interlayer) in manganite. Interestingly, birnessite (PZC ~1.9) surfaces were shown by Banerjee and Nesbitt (1999) to sorb both cationic $CrOH^{2+}$ and anionic $HCrO_4^-$ species at a pH of ~4.6

where the surface would have a negative charge. These observations suggest that electrostatic forces acting between aqueous chromium and Mn-oxide are not of primary importance to Cr-uptake.

4.3 Heterogeneity of reaction

In-situ AFM and ex-situ FESEM observations show that Cr_{aq}-manganite interactions are highly heterogeneous, with some manganite surfaces showing localized microprecipitation and/or dissolution, and adjacent areas exhibiting little or no evidence for any reaction. The extent of this heterogeneity varies from sample to sample and may be dependent on a variety of physical and chemical attributes (e.g. defects, trace element dopants, twinning, micropores) and their affects on the electronic properties of the surface (e.g. band gap, electron mobility, work function). There are two lines of direct evidence observed in this study which demonstrate that the conductivity of manganite varies across its surface: 1) differential charging as revealed in voltage contrast SEM imaging, and 2) unreliable engagement of an STM tip with manganite, depending on the exact area of tip approach. The numerous factors which contribute to heterogeneous semiconductor properties preclude drawing any unambiguous conclusions. However, if electron mobility is locally inhibited on the manganite surface, then adsorbed Cr^{3+} is unlikely to be oxidized. This situation may allow for the formation of single or multinuclear $Cr(OH)_3 \cdot 3H_2O$ complexes which may accumulate to form surface clusters (Bleam and McBride, 1985) or surface precipitates (Fendorf et al., 1992; Fendorf and Zasoski, 1992). Results of our FESEM and in-situ AFM experiments are consistent with the hypothesis that variations in surface conductivity may promote $Cr(OH)_3 \cdot 3H_2O$ surface precipitation.

It has been observed in many experiments that $Cr(OH)_3 \cdot 3H_2O$ precipitates are often not spatially associated with sites of dissolution. It is logical that precipitation would tend not to occur near sites of manganite dissolution because dissolution would require either Mn-reduction (for reductive dissolution) or Mn-protonation (for acidic dissolution) which would interfere with $Cr(OH)_3 \cdot 3H_2O$ precipitation.

For areas of the manganite surface where electron transfer is not inhibited, we expect that electrons originating from an inner spherically bound Cr^{3+} are conducted into the manganite. This transfer of electrons results in the formation and subsequent desorption of chromate and

either: 1) manganite dissolution localized at the Cr-adsorption site, or 2) dissolution occurring at some other surface site, perhaps even spatially distant from the Cr-adsorption site. Heterogeneous Cr-uptake and manganite dissolution behaviors such as we have observed are not uncommon in some metallic corrosion processes (Scully, 1990; Stumm and Morgan, 1996 and references therein). In addition, there is a growing base of STM and AFM observations and supporting quantum mechanical calculations which show that redox reactions occurring on semiconducting mineral surfaces are often spatially heterogeneous (Junta and Hochella, 1994; Rosso and Hochella, 1997; Becker and Hochella, 1997; Rosso et al., 1999a,b). These findings have recently been formulated into what has been termed the proximity effect (Becker et al., 2001). The idea is that, due to the delocalized nature of electrons in semiconducting materials, a reducing or oxidizing chemical species at a surface site not only influences the electronic structure of neighboring sites, but also may influence other sites some distance away through electron transfer processes. In the case of Cr^{3+} adsorption and oxidation on manganite surfaces, this tells us that electron transfer from Cr to Mn need not necessarily involve only next nearest neighbor metal atoms. In fact, electrons donated by sorbed Cr atoms may travel in the conduction band of the manganite to a Mn site, for example, at a surface step or kink site some distance away where the reduced Mn will desorb, eventually forming a dissolution pit at that location after multiple transfers.

4.4 Environmental Implications

Our experiments show that in undersaturated $Cr(OH)_3 \cdot 3H_2O$ solutions the reaction between manganite and Cr^{III}_{aq} efficiently oxidizes Cr^{III}_{aq} to Cr^{VI}_{aq} (especially at low pH or low to negative S.I.) with a simultaneous decrease in the $[Cr]^{T}_{aq}$ due to Cr-adsorption and surface catalyzed precipitation of $Cr(OH)_3 \cdot 3H_2O$. The chromate production results in a significant increase in solution toxicity (Nriagu et al., 1988). In the natural environment this threat of increased toxicity is often reduced by competing or parallel processes such as: 1) passivation of the Mn-oxide surface by metal sorbates and precipitates (Fendorf et al., 1993; Pratt et al., 1997); 2) complexation of Mn^{III}_{aq} with organic and inorganic ligands (Johnson and Xyla, 1992; Nico and Zasoski, 2000); 3) bulk precipitation of $Cr(OH)_3 \cdot 3H_2O$; and 4) the presence of reductants (e.g. natural organic matter, Fe^0, Fe^{2+}-containing phases) (Powell et al., 1995; Peterson et al., 1997;

Blowes et al., 1997; Jardine et al., 1999). The relative importance of each of these competing processes is dictated by the presiding aqueous and mineralogical conditions. Through much laboratory and field experimentation it has been shown that the extent and rate of Cr^{III}_{aq} oxidation is greatest in environments of low pH and high Mn-oxide content. Given this knowledge, appropriate geochemical conditions for safe chromium disposal include: 1) slightly basic to neutral pH; 2) the absence of Mn-oxides; and 3) the presence of a strong reductant (e.g. Fe^0). Satisfying more than one of these conditions provides added security that chromium remains in the relatively immobile and nontoxic Cr^{III}_{aq} or $Cr(OH)_3 \cdot 3H_2O_{(s)}$ state.

Acknowledgements- This work was supported by grants from the NSF (#EAR 96-9628023, #99-9902996 and #9975678) and The American Federation of Mineralogists. The authors wish to thank Don Rimstidt and Matt Eick of Virginia Tech for insightful comments.

5. REFERENCES

Amacher M. C. and Baker D. A. (1982) Redox reactions involving chromium, plutonium and manganese in soils. Institute for Research on Land and Water Resources, Penn. State Univ.

Banerjee D. and Nesbitt H. W. (1999) Oxidation of aqueous Cr(III) at birnessite surfaces: constraints on reaction mechanism. Geochim. Cosmochim. Acta **63**, 1671-1687.

Becker U., Hochella M. F., Jr., and Vaughan D. J. (1997) The adsorption of gold to galena surfaces: calculation of adsorption/reduction energies, reaction mechanisms, XPS spectra, and STM images. Geochim. Cosmochim. Acta **61**, 3565-3585.

Becker U., Rosso K. M., and Hochella M. F., Jr. (2001) The proximity effect on semiconducting mineral surface: A new aspect of mineral surface reactivity and surface complexation theory? Geochim. Cosmochim. Acta **65**, 2641-2649.

Bleam W. F. and McBride M. B. (1985) Cluster formation versus isolated-site adsorption. A study of Mn(II) and Mg(II) adsorption on boehmite and goethite. J. Colloid Interf. Sci. **103**, 124-132.

Blowes D. W., Ptacek C. J., and Jambor J. L. (1997) In-Situ Remediation of Cr(VI)-Contaminated Groundwater Using Permeable Reactive Walls: Laboratory Studies. Environ. Sci. Technol. **31**, 3348-3357.

Buerge I. J. and Hug S. J. (1999) Influence of Mineral Surfaces on Chromium(VI) Reduction by Iron(II). Environ. Sci. Technol. **33**, 4285-4291.

Burns R. G. and Burns V. M. (1979) Manganese oxides. Rev. Mineral. 6, 1-46

Chao T. T. and Anderson B. J. (1974) The scavenging of silver by manganese and iron oxides in stream sediments collected from two drainage areas of Colorado. Chem. Geol. **14**, 159-166.

Chung J.-B. (1998) Chromium speciation in Cr(III) oxidation by Mn-oxides: relation to the oxidation mechanism. Han'guk Nonghwa Hakhoechi **41**, 89-94.

Chung J.-B., Zasoski R. J., and Lim S.-U. (1994) Kinetics of chromium(III) oxidation by various manganese oxides. Han'guk Nonghwa Hakhoechi **37**, 414-20.

Dillard J. G., Koppelman M. H., Crowther D. L., Schenck C. V., Murray J. W., and Balistrieri L. (1981) X-ray photoelectron spectroscopic (XPS) studies on the chemical nature of metal

ions adsorbed on clays and minerals. In Adsorpt. Aqueous Solutions, [Proc. Symp.], 227-40.

Eary L. E. and Rai D. (1987) Kinetics of chromium (III) oxidation to chromium (VI) by reaction with manganese oxide. Environ. Sci. Technol. **26** (79-85).

Evans S. and Raftery E. (1982) Determination of the oxidation state of manganese in lepidolite by x-ray photoelectron spectroscopy. Clay Mineral **17**, 477-81.

Fendorf S. E., Fendorf M., Sparks D. L., and Gronsky R. (1992) Inhibitory mechanisms of chromium(III) oxidation by δ-manganese dioxide. J. Colloid Interf. Sci. **153**, 37-54.

Fendorf S. E. and Zasoski R. J. (1992) Chromium (III) oxidation by δ-MnO_2: Characterization. Environ. Sci. Technol. **21**(1187-1193).

Fendorf S. E., Zasoski R. J., and Burau R. G. (1993) Competing metal ion influences on chromium (III) oxidation by birnessite. Soil Sci. Soc. Amer. J. **57**, 1508-1515.

Goldstein J. I., Newbury D. E., Echlin P., Joy D., Romig A. D. J., Lyman C. E., Fiori C., and Lifshin E. (1992) Scanning electron microscopy and X-ray microanalysis Plenum Press.

Gray M. J. and Malati M. A. (1979) Adsorption from aqueous solution by δ-manganese oxide: II Adsorption of some heavy metal cations. J. Chem. Technol. Biotechnol. **29**, 135-144.

Gupta R. P., Sen, S.K. (1974) Calculations of multiplet structure of core p-vacancy levels. Phys. Rev. B **10**, 71-79.

Gupta R. P., Sen, S.K. (1975) Calculation of multiplet structure of p-vacancy levels II. Phys. Rev. B **12**, 15-19.

Halada G. P. and Clayton C. R. (1991) Photoreduction of hexavalent chromium during X-ray photoelectron spectroscopy analysis of electrochemical and thermal films. J. Electrochem. Soc. **138**, 2921-2927.

Hem J. D. (1981) Rates of manganese oxidation in aqueous systems. Geochim. Cosmochim. Acta **45**, 1369-1374.

Hem J. D., Lind C. J., and Roberson C. E. (1989) Coprecipitation and redox reactions of manganese oxides with copper and nickel. Geochim. Cosmochim. Acta **53**, 2811-2822.

Hem J. D., Roberson C. E., and Fournier R. B. (1982) Stability of β-MnOOH and manganese oxide deposition from springwater. Water Resources Res. **18**, 563-570.

Ikemoto I., Ishii K., Kinoshita S., Kuroda H., Alario-Franco M. A., and Thomas J. M. (1976) X-ray photoelectron spectroscopic studies of chromium dioxide and some related chromium compounds. In J. Solid State Chem. **17**, 425-430.

Ilton E. S., Veblen D. R., Moses C. O., and Raeburn S. P. (1997) The catalytic effect of sodium and lithium ions on coupled sorption-reduction of chromate at the biotite edge-fluid interface. Geochim. Cosmochim. Acta **61**, 3543-3563.

Jardine P. M., Fendorf S. E., Mayes M. A., Larsen I. L., Brooks S. C., and Bailey W. B. (1999) Fate and Transport of Hexavalent Chromium in Undisturbed Heterogeneous Soil. Environ. Sci. Technol. 33, 2939-2944.

Johnson C. A. and Xyla A.G. (1991) The oxidation of Chromium(III) to chromium(VI) on the surface of manganite (γ-MnOOH). Geochim. Cosmochim. Acta **55**, 2861-2866.

Johnsson P. A., Eggleston C. M., and Hochella M. F. Jr., (1991) Imaging the molecular-scale structure and microtopography of hematite with the atomic force microscope. Amer. Mineral. **76**, 1442-1445.

Junta J. L. and Hochella M. F., Jr. (1994) Manganese(II) oxidation at mineral surfaces: a microscopic and spectroscopic study. Geochim. Cosmochim. Acta **58**, 4985-4999.

Kavanaugh M. C. (1994) Alternative for Groundwater Cleanup. National Academy Press.

Lind C. J. (1988) Hausmannite (Mn_3O_4) conversion to manganite (γ-MnOOH) in dilute oxalate solution. Environ. Sci. Technol. **22**, 62-70.

Malati M. A. and Rophael M. W. (1999) Radiochemical and physicochemical characterization of manganese oxides. Surf. Sci., **433-435**, 740-744.

Manceau A. and Charlet L. (1992) X-Ray absorption spectroscopy study of the sorption of Cr(III) at the oxide-water interface I. Molecular mechanisms of Cr(III) oxidation on Mn oxides. J. Colloid Interf. Sci. **148**, 425-442.

McKenzie R. M. (1967) The sorption of cobalt by manganese minerals in soils. Australian J. Soil Res. **5**, 235-246.

McKenzie R. M. (1980) The adsorption of lead and other heavy metals on oxides of manganese and iron. Australian J. Soil Res. **18**, 61-73.

Means J. L., Crerar D.A., Borcsik M. P., Duguid J.O. (1978) Adsorption of Co and selected actinides by Mn and Fe oxides in soils and sediments. Geochim. Cosmochim. Acta **42,** 1763-1773.

Murray D. J., Healy T. W., and Fuerstenau D. W. (1968) The adsorption of aqueous metal on colloidal hydrous manganese oxide. In Adsorption from Aqueous Solution, 79 (ed. W. J. Weber, Jr. and E. Matijevic), 74-87. Amer. Chem. Soc.

Murray J. W. and Dillard J. G. (1979) The oxidation of cobalt(II) adsorbed on manganese dioxide. Geochim. Cosmochim. Acta **43**, 781-787.

Murray J. W., Dillard J. G., Giovanoli R., Moers H., and Stumm W. (1985) Oxidation of Mn(II): Initial mineralogy, oxidation state and ageing. Geochim. Cosmochim. Acta **49**, 463-470.

Nico P. S. and Zasoski R. J. (2000) Importance of Mn(III) Availability on the Rate of Cr(III) Oxidation on δ-MnO_2. Environ. Sci. Technol. **34**, 3363-3367.

Nriagu J. O., Nieboer E., and Editors. (1988) Advances in Environmental Science and Technology, **20**: Chromium in the Natural and Human Environments, p. 571.

Peterson M. L., Brown G. E., Jr., Parks G. A., and Stein C. L. (1997) Differential redox and sorption of Cr(III/VI) on natural silicate and oxide minerals: EXAFS and XANES results. Geochim. Cosmochim. Acta **61**, 3399-3412.

Powell R. M., Puls R. W., Hightower S. K., and Sabatini D. A. (1995) Coupled Iron Corrosion and Chromate Reduction: Mechanisms for Subsurface Remediation. Environ. Sci. Technol. **29**, 1913-22.

Pratt A. R., Blowes D. W., and Ptacek C. J. (1997) Products of Chromate Reduction on Proposed Subsurface Remediation Material. Environ. Sci. Technol. **31**, 2492-2498

Pratt A. R. and McIntyre N. S. (1996) Comment on curve fitting of Cr 2p photoelectron spectra of Cr_2O_3 and CrF_3. Surf. Interface Anal. **24**, 529-530.

Rai D., Sass B. M., and Moore D. A. (1987) Chromium(III) hydrolysis constants and solubility of chromium(III) hydroxide. Inorg. Chem. **26**, 345-349

Rophael M. W. and Boulis S. N. (1982) Kinetics of the oxidation of chromium(III) ions by trimanganese tetroxide and by manganese(III) oxide. Surf. Technol. **16**, 243-248.

Rosso K. M., Becker U., and Hochella M. F., Jr. (1999a) Atomically resolved electronic structure of pyrite {100} surfaces: an experimental and theoretical investigation with implications for reactivity. Amer. Mineral. **84**, 1535-1548.

Rosso K. M., Becker U., and Hochella M. F., Jr. (1999b) The interaction of pyrite {100} surfaces with O_2 and H_2O: fundamental oxidation mechanisms. Amer. Mineral., **84**, 1549-1561.

Schroeder D. C. and Lee G. F. (1975) Potential transformations of chromium in natural waters. Water, Air, Soil Pollution **4**, 355-365.

Scully J. C. (1990) The Fundamentals of Corrosion. Pergamon Press, p. 226.

Silvester E., Charlet., L., Manceau, Alain. (1995) Mechanism of Chromium(III) Oxidation by Na-Buserite. J. Phys. Chem. **99**, 16662.

Stumm W. and Morgan J. J. (1996) Aquatic Chemistry- Chemical equilibria and rates in natural waters. John Wiley and Sons, Inc. p. 1022

Van Der Weijden C. D. and Reith M. (1982) Chromium(III)-Chromium(VI) interconversions in seawater. Marine Chem. **11**, 565-572.

6. CHAPTER 1: Tables and Figures

Table 1. XPS peak parameters for $Mn2p^{3/2}$, $Cr2p^{3/2}$ and O1s.

Multiplet	B.E., eV	Intensity[a]	FWHM	G./L.[b]	ref.[c]
Mn^{3+}, $Mn2p^{3/2}$ 1	640.28	0.760	1.25	0.85	1
Mn^{3+}, $Mn2p^{3/2}$ 2	641.12	1.000	1.25	0.85	1
Mn^{3+}, $Mn2p^{3/2}$ 3	641.97	0.849	1.25	0.85	1
Mn^{3+}, $Mn2p^{3/2}$ 4	642.91	0.464	1.25	0.85	1
Mn^{3+}, $Mn2p^{3/2}$ 5	644.00	0.222	1.7	0.85	1
$Mn2p^{3/2}$ overall	641.40	1.33	~3.23	na.	1
Mn^{3+}, $Mn2p^{3/2}$ 1[e]	640.70	0.741	1.00	1.00	2,3
Mn^{3+}, $Mn2p^{3/2}$ 2[e]	641.40	0.741	1.00	1.00	2,3
Mn^{3+}, $Mn2p^{3/2}$ 3[e]	642.30	1.000	1.00	1.00	2,3
Mn^{3+}, $Mn2p^{3/2}$ 4[e]	643.10	0.519	1.00	1.00	2,3
Mn^{3+}, $Mn2p^{3/2}$ 5[e]	644.90	0.222	1.00	1.00	2,3
Cr^{3+}, $Cr2p^{3/2}$ 1	576.07	1.000	1.50	0.95	1
Cr^{3+}, $Cr2p^{3/2}$ 2	577.23	0.943	1.50	0.95	1
Cr^{3+}, $Cr2p^{3/2}$ 3	578.46	0.245	1.50	0.95	1
$Cr2p^{3/2}$ overall	576.70	1.48	~2.7	na.	1
Cr^{3+}, $Cr2p^{3/2}$ 1[d,e]	576.30	na.	1.00	1.00	2,3
Cr^{3+}, $Cr2p^{3/2}$ 2[d,e]	577.60	na.	1.00	1.00	2,3
Cr^{3+}, $Cr2p^{3/2}$ 3[d,e]	578.90	na.	1.00	1.00	2,3
Cr^{3+}, $Cr2p^{3/2}$ 1	576.02	na.	1.40	na.	4
Cr^{3+}, $Cr2p^{3/2}$ 2	577.00	na.	1.40	na.	4
Cr^{3+}, $Cr2p^{3/2}$ 3	577.79	na.	1.40	na.	4
O^{2-}, O1s	529.05	1.000	1.51	1.00	1, 3, 5
OH^-, O1s	530.40	1.000	1.51	1.00	1, 3, 5
H_2O, O1s	531.82	0.244	1.75	1.00	1, 3, 5

a. Peak intensities are ratios against the most intense multiplet observed within each data set.

b. Gaussian equals 1, Laurentzian equals 0.

c. References: 1. This work; 2. Gupta and Sen, 1975; 3. Nesbitt and Banerjee, 1998; 4. Pratt and McIntyre, 1996; 5. Junta and Hochella, 1994

d. Peak parameters obtained from curve fitting of a scanned image of Figure 2 of Gupta and Sen, 1975.

e. Multiplet parameters are for the Cr^{3+} and Mn^{3+} free ion.

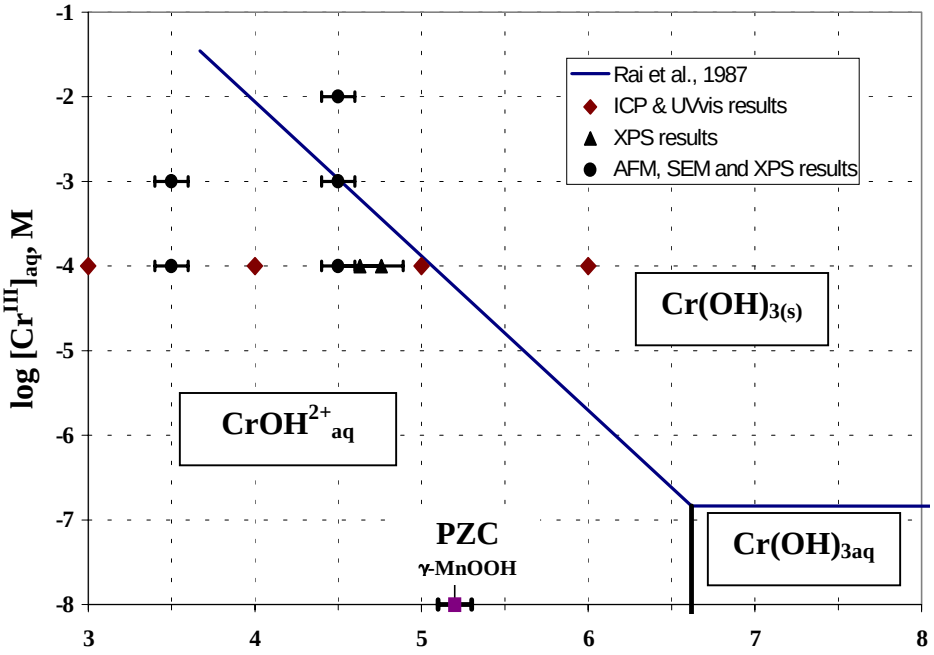

Fig. 1. Stability diagram for Cr^{III}_{aq} as a function of pH and $[Cr^{III}]_{aq}$ (modified after Rai et al., 1987). $CrOH^{2+}_{aq}$ is the dominant species under acidic conditions. The plotted data shows the aqueous conditions employed in each of our experiments. The symbols indicate the primary analytical method(s) used to characterize that particular experiment as discussed in the results. The PZC of manganite has been labeled on the pH axis.

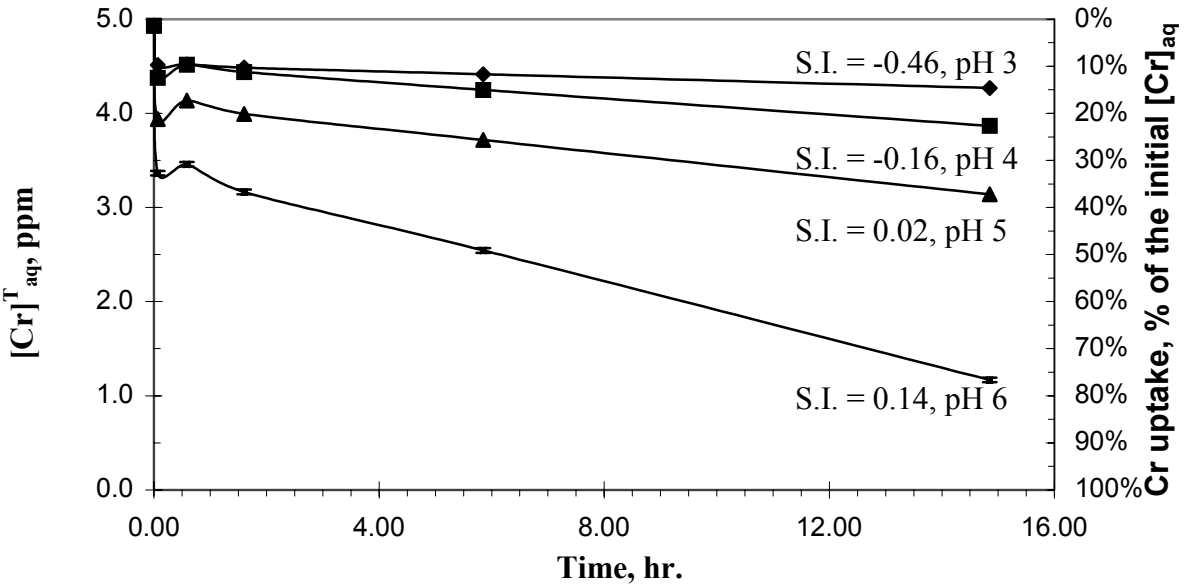

Fig. 2. Total aqueous chromium concentration with time and pH as measured by ICP. The initial solution contained 10^{-4} M Cr^{III}_{aq} (4.9 ppm) and 0.45g/L γ-MnOOH at pH 3, 4, 5, 6. The decreasing trend in the total aqueous chromium with time and pH results from $Cr(OH)_3 \cdot 3H_2O$ precipitation and Cr-adsorption on the manganite surface and in solution. On the right side y-axis is given the Cr-uptake as a percentage of the initial chromium concentration. S.I. = saturation index for $Cr(OH)_{3(s)}$.

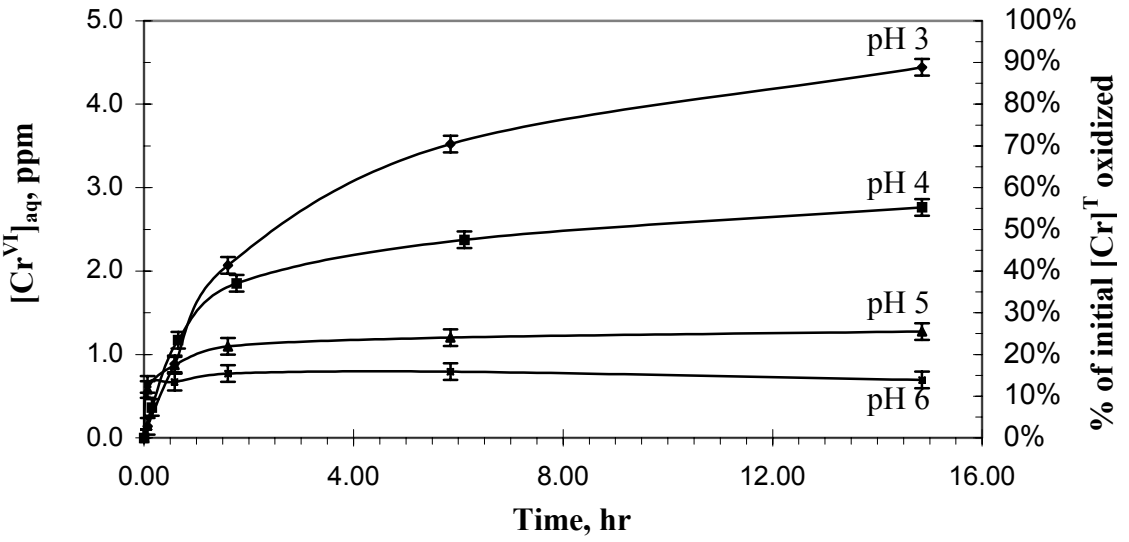

Fig. 3. Chromate concentration with time and pH as measured by UVvis. The initial $[Cr^{III}]_{aq}$ was 4.9 ppm (~10^{-4} M). The y-axis on the right side indicates the percentage of the initial Cr^{III}_{aq} that has been oxidized to $HCrO_4^-$.

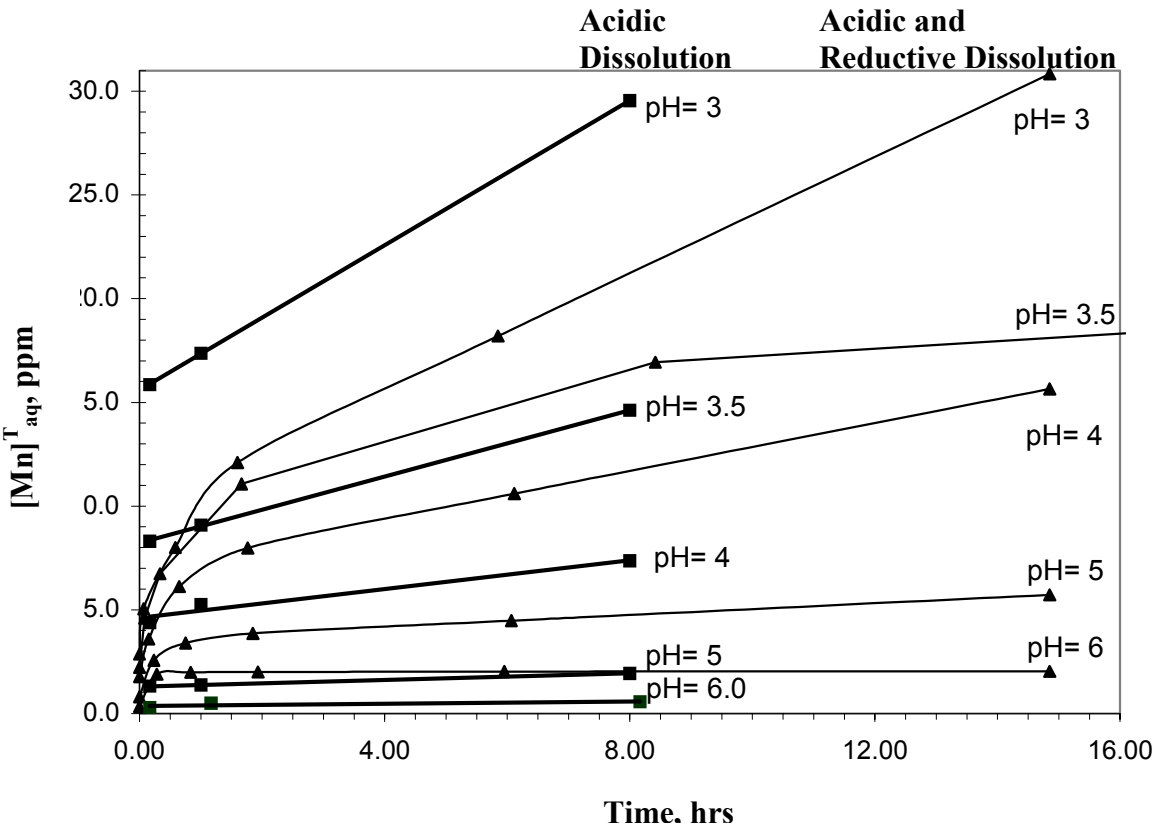

Fig. 4. Total aqueous manganese concentration with reaction time and pH as observed for acidic dissolution in HNO_3 (values plotted to 8 hr.) and for reductive plus acidic dissolution in 4.9 ppm (~10^{-4} M) Cr^{III}_{aq} (values plotted to 15 hr.). Note that at pH 3.5 the rate of acidic dissolution is nearly the same as the rate of reductive plus acidic dissolution. However, at pH 3 the rate of acidic dissolution is greater and for pH > 3.5 the rate of reductive plus acidic dissolution is greater. In the acidic dissolution experiments, the first sample was collected after 10 min. of reaction.

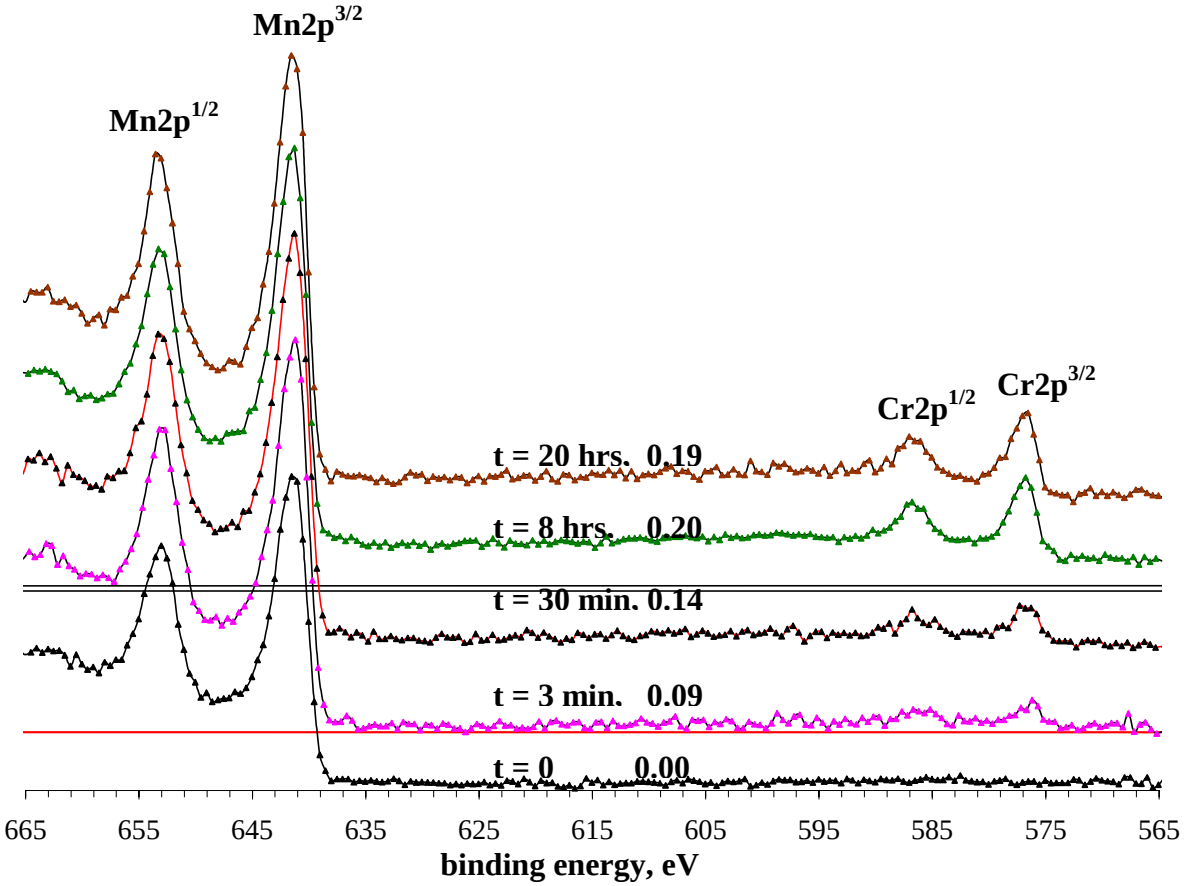

Fig. 5. XPS spectra of the Mn2p and Cr2p photopeaks of manganite before and after exposure to pH ~4.6, 10^{-4} M Cr^{III}_{aq} solution for the lengths of time indicated on each spectra. The number following the reaction time is the ratio of the $Cr2p^{3/2}$: $Mn2p^{3/2}$ peak areas.

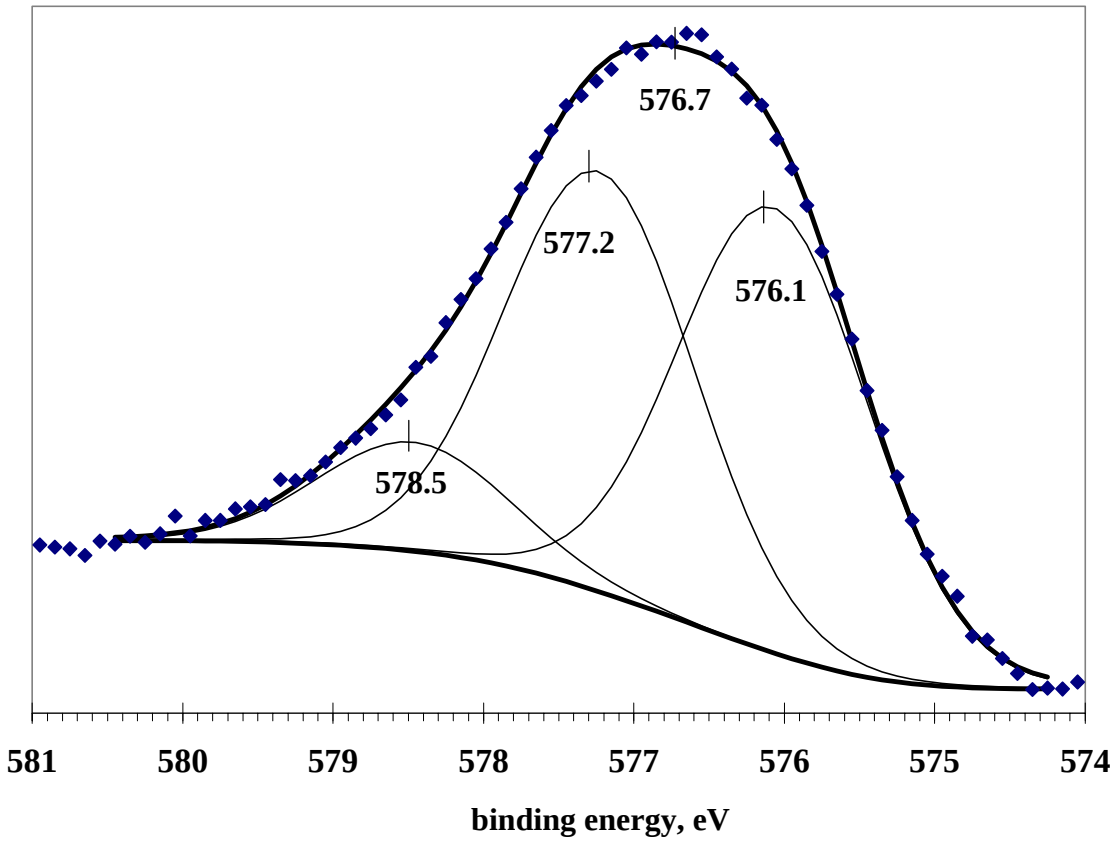

Fig. 6. XPS spectra of the $Cr2p^{3/2}$ photopeak collected after 20 hours of reaction with pH ~4.6, 10^{-4} M Cr^{III}_{aq}. The peak shape and position in the spectra is nearly identical to that observed in the other samples. The three thin curves show the theoretical multiplet structure (slightly modified) calculated for the Cr^{3+} free ion (Gupta and Sen, 1974; 1975). The two thick solid lines illustrate the fit to the raw data and the Shirley background.

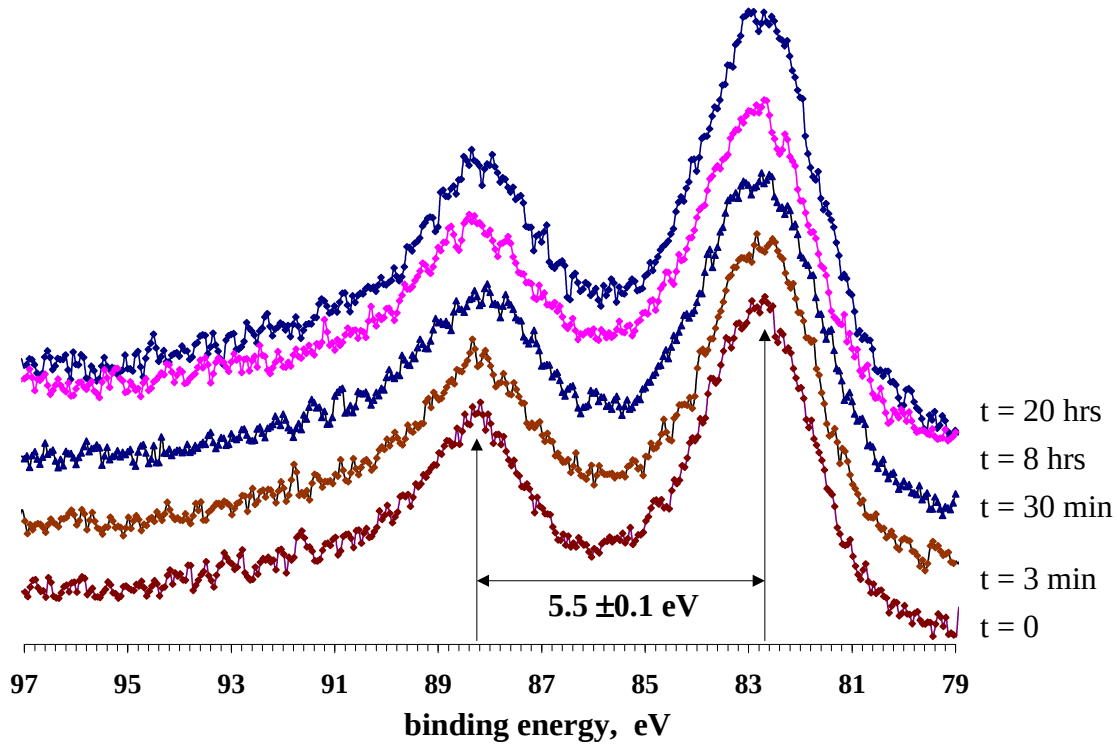

Fig. 7. Comparison of Mn3s XPS spectra of manganite before and after reaction with pH ~4.6, 10^{-4} M Cr^{III}_{aq}. The multiplet splitting of 5.5 ± 0.1 eV is constant throughout the reaction indicating only the presence of Mn^{3+}.

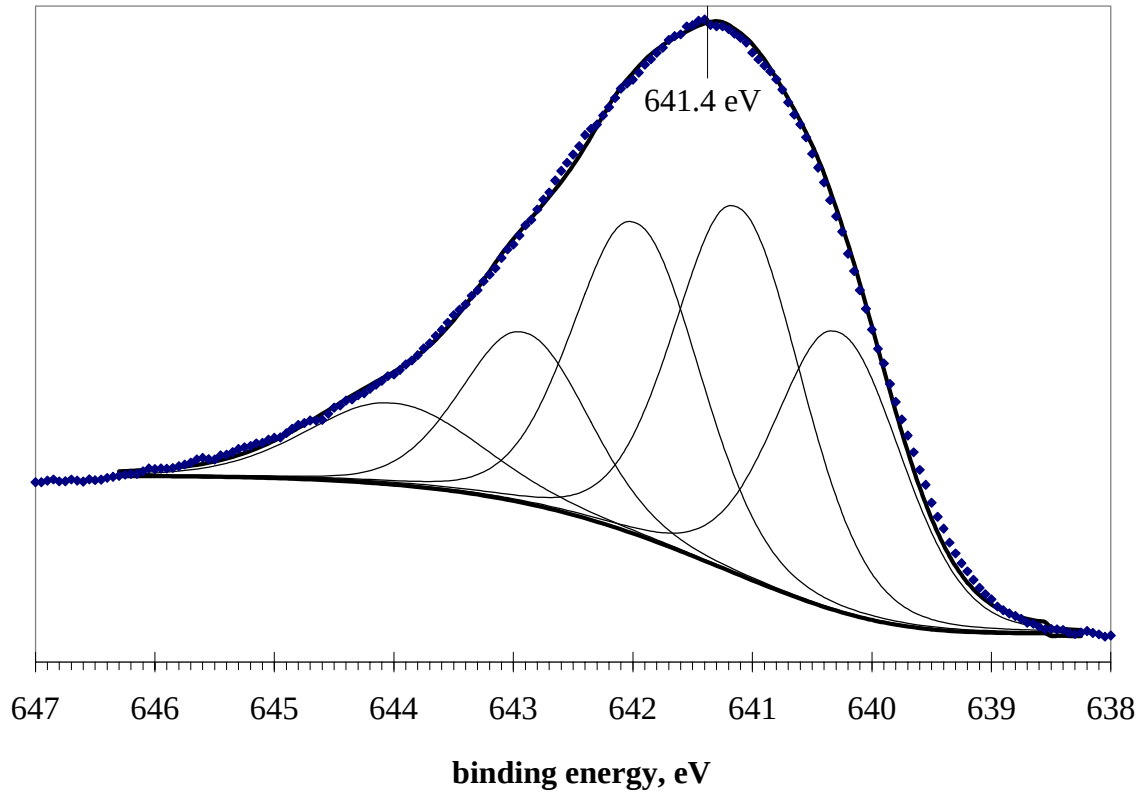

Fig. 8. XPS spectra of the $Mn2p^{3/2}$ photopeak collected after 8 hours of reaction with pH ~4.6, 10^{-4} M Cr^{III}_{aq}. The position and shape of the $Mn2p^{3/2}$ peak was nearly identical for each reacted sample. The thin lines show the theoretical multiplet structure (slightly modified) of the Mn^{3+} free ion (Gupta and Sen, 1974; 1975). The bold line nearly superimposed on the raw data illustrates the good agreement between the theoretical model and experimental data.

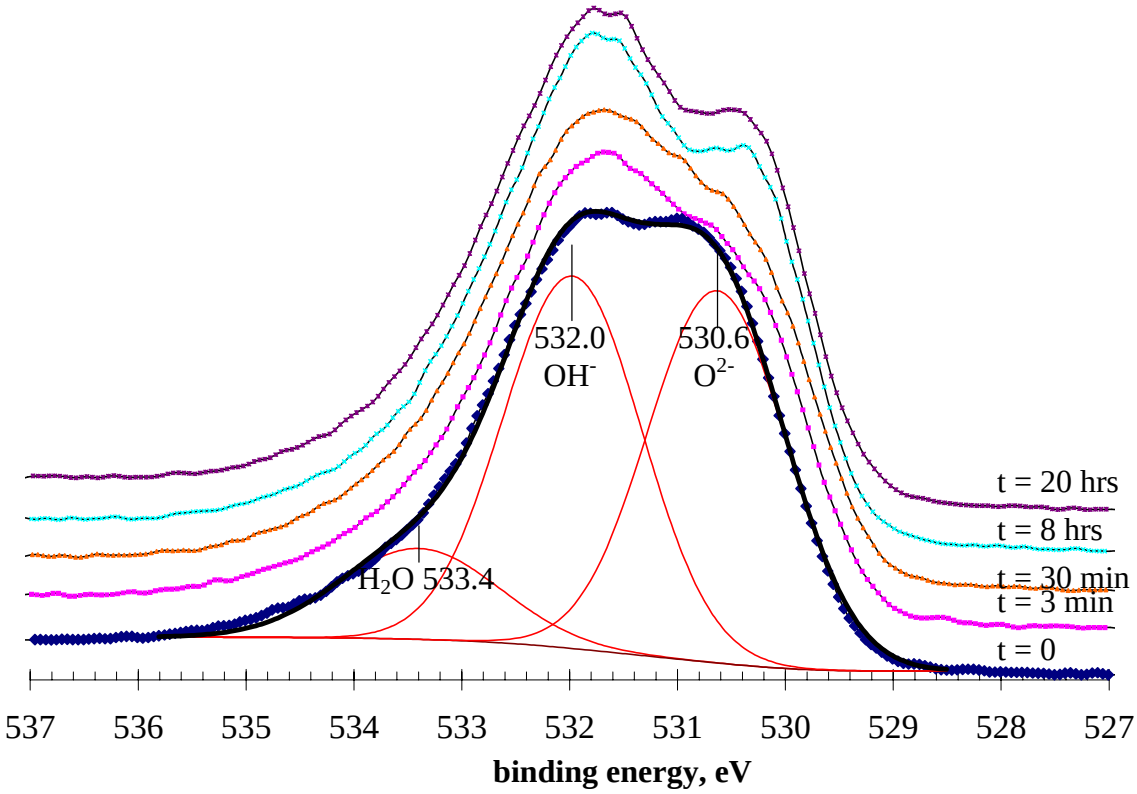

Fig. 9. XPS spectra of the O1s region on manganite before and after reaction with pH ~4.6, 10^{-4} M Cr^{III}_{aq}. The t = 0 sample was equilibrated in pH 4.5 HNO_3^- for 30 min. and is well fit (solid line superimposed on raw data) using 1:1 quantities (i.e. stoichiometric) of OH^- and O^{2-} and minor (12%) H_2O. With increasing time of reaction the contributions from the OH^- and H_2O components increase.

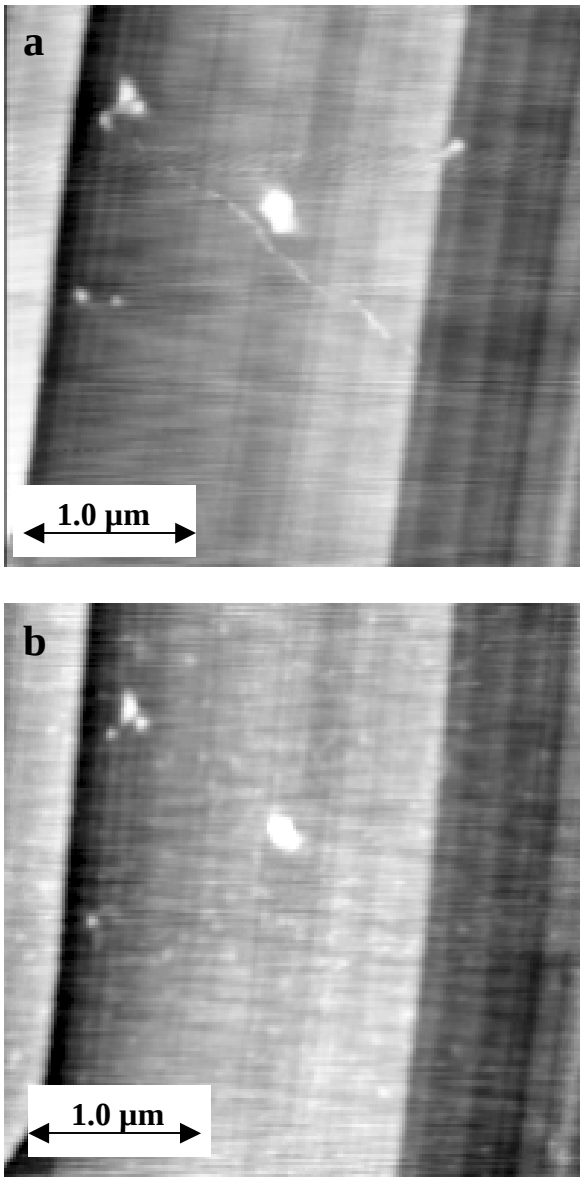

Fig. 10. Comparison of fluid-cell TMAFM images obtained in pH 3.5 HNO_3 (a, t = 0) and immediately after exposure (b, t = 4 min.) to pH 3.5, 10^{-4} M $Cr^{III}_{aq.}$ The adsorbates/ microprecipitates seen in (b) range from 0.3 - 1.3 nm tall and have lateral dimensions ranging from 10 - 100 nm. The lateral dimensions of these particles are likely to be much smaller but the finite AFM tip radius (>20 nm) causes the particles to appear larger. In (b), a low pass filter has been applied to remove a high frequency component caused by the Tapping® process.

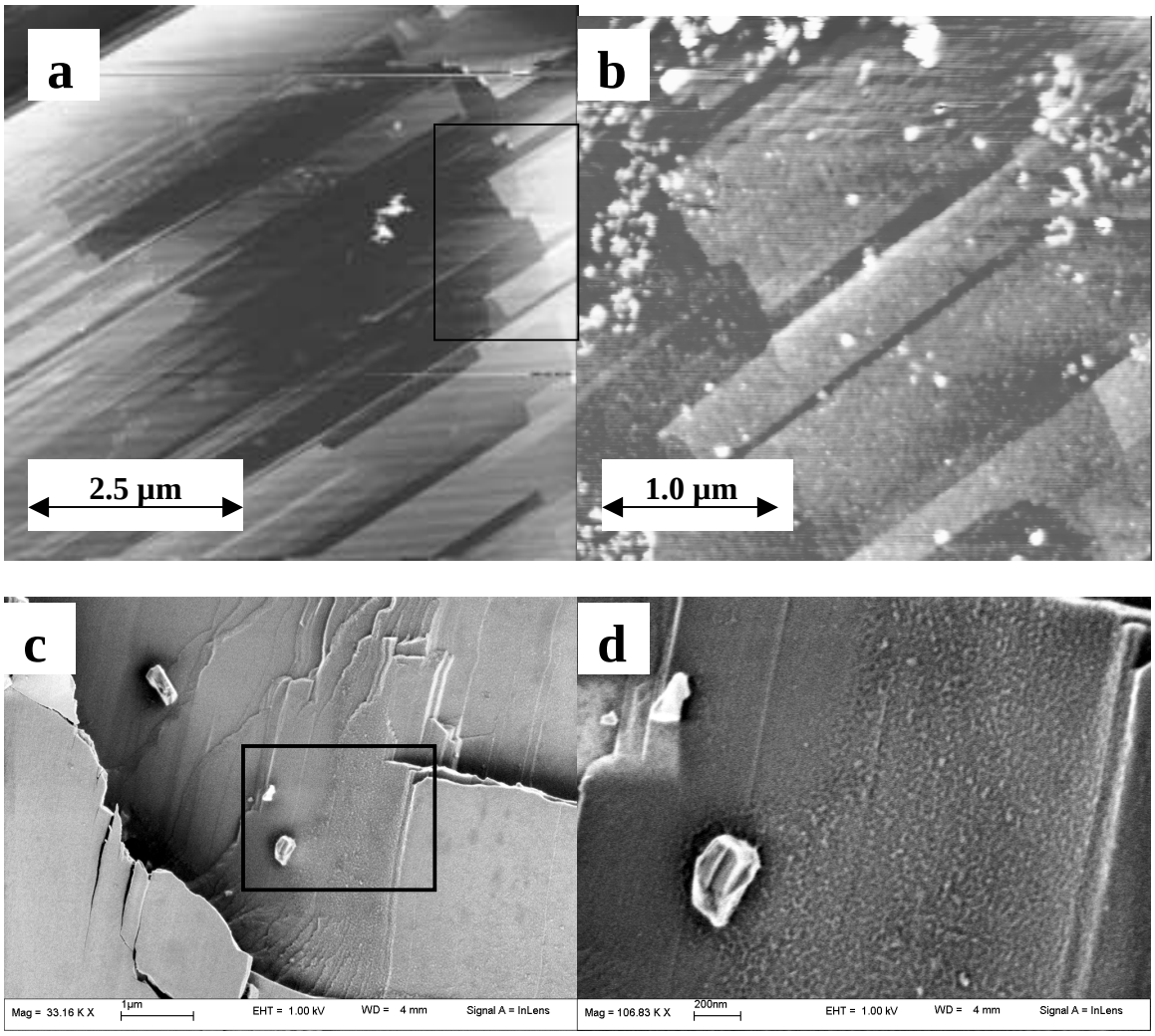

Fig. 11. AFM and FESEM images of manganite before (a) and after (b, c, d) exposure to Cr^{III}_{aq}. a) TMAFM images obtained in pH 4.5 HNO_3 (t = 0). The fresh surface is characterized by broad atomically flat terraces with most step edges directed along [001]. b) Area outlined in (a) after exposure to a pH 4.5, 10^{-4} M Cr^{III}_{aq} for 5 min. Compared to (a) the surface is rougher with microprecipitates ranging in size from 0.3 – 10 nm tall and having lateral dimensions ranging from 10 – 300 nm. Fine scale homogeneous surface pitting has also occurred. Adjacent areas may show dissolution with no precipitation or no change in the topography relative to the HNO_3^- reacted surface. c,d) FESEM images of a different manganite sample after 2 hours of exposure to pH 4.5, 10^{-4} M Cr^{III}_{aq} solution. The outlined area in (c) shows the location of (d). Images were obtained at 1 kV using an 'in-lens' SE_I detector. The distribution of adsorbates/microprecipitates is spatially heterogeneous. That is, patches of precipitate are bounded by large areas devoid of Cr-hydroxy hydrate precipitates. Chromium was detected on these samples by XPS but not with EDS.

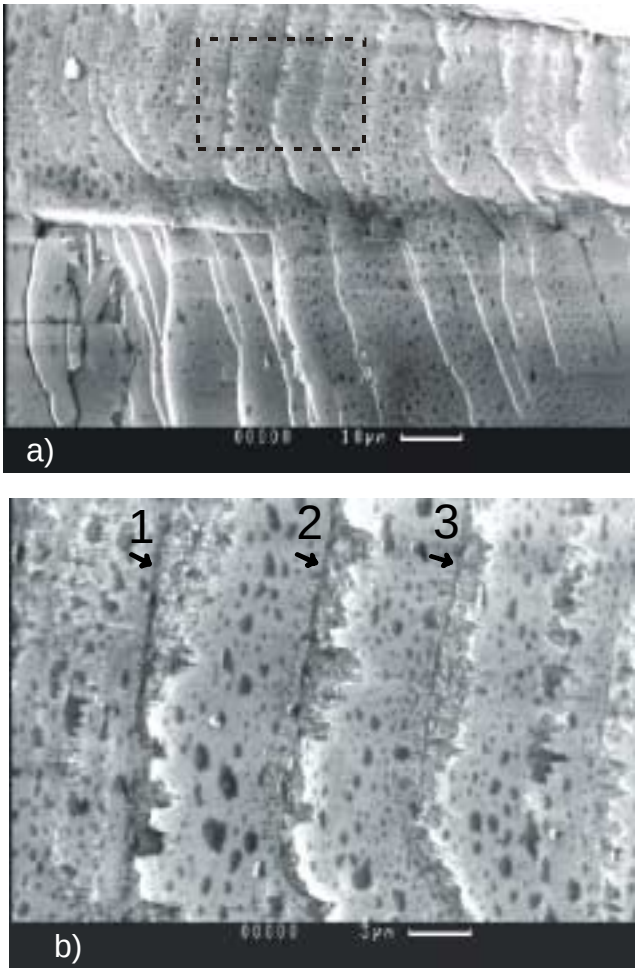

Fig. 12. SEM images of a manganite after reaction for 10 hours in a pH 4.5 ±0.2, ~10^{-3} M (46 ppm) Cr^{III}_{aq} solution. Image (a) illustrates the degree of dissolution heterogeneity commonly seen in our experiments. The extent of dissolution observed across the surface varies widely, with few dissolution pits seen in the lower left area relative to the area outlined above. (b) Enlargement of area outlined in (a). No Cr-microprecipitates were observed in this area, although the 30 kV accelerating voltage used to collect these images results in a low degree of surface sensitivity. The linear dissolution features marked '1', '2' and '3' presumably mark the location of the step edges prior to dissolution.

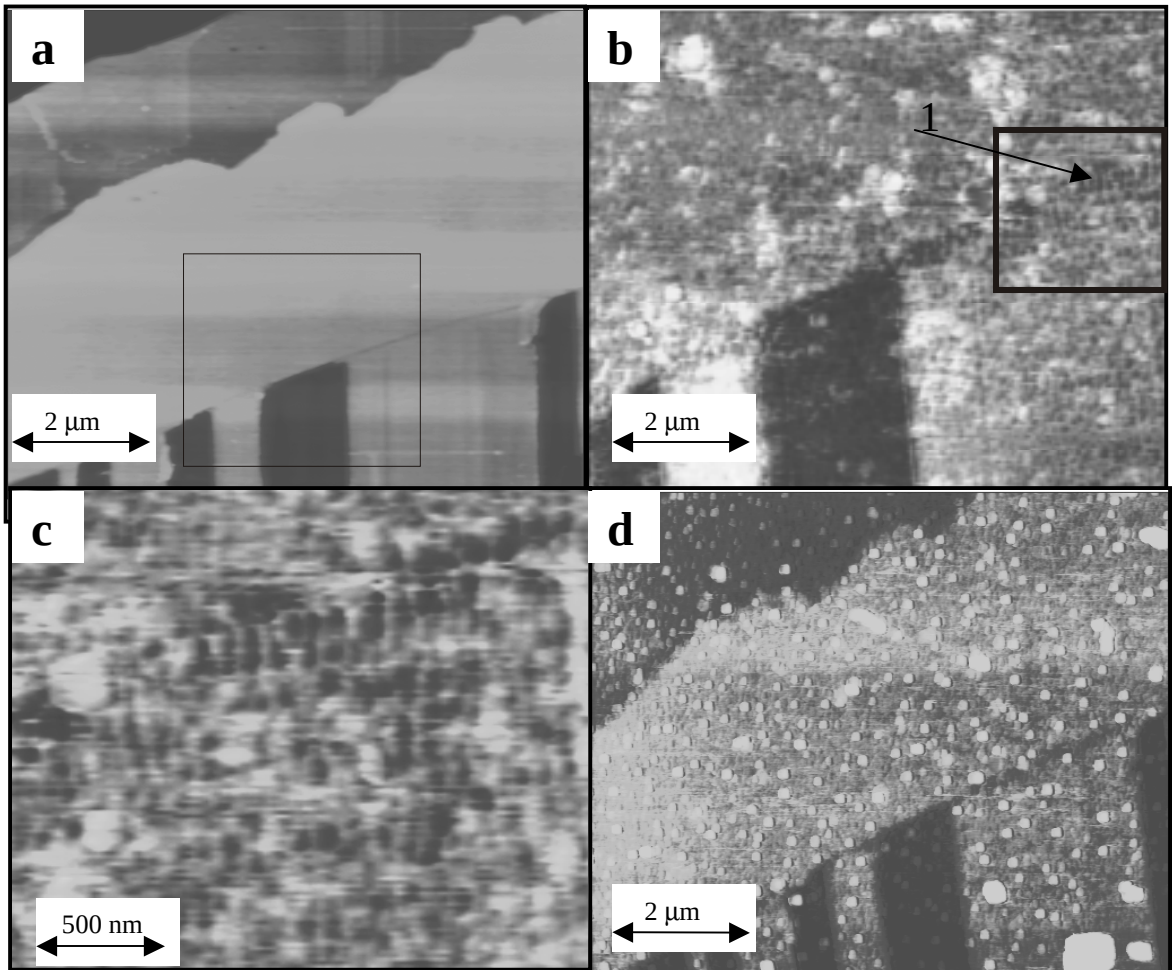

Fig. 13. Comparison of fluid-cell TMAFM images obtained in pH 4.5 HNO_3 at t = 0 (a) and after exposure to a pH 4.5, 10^{-2} M Cr^{III}_{aq} (b-d). b) Image was obtained within 4 minutes of exposure. The adsorbates/microprecipitates (bright patches) are ~ 0.5 to 7 nm high. Note that dissolution is slightly more extensive along the step edge marked '1' in (b) and enlarged in (c). c) Enlarged view of area outlined in (b). Dissolution pits are ~1 nm deep and are elongate along [001]. d) AFM image collected in air after the sample has been reacted for 10 hr. The surface is now extensively covered by $Cr(OH)_3 \bullet 3H_2O$ precipitates (identified by XPS), some measuring 50 nm high.

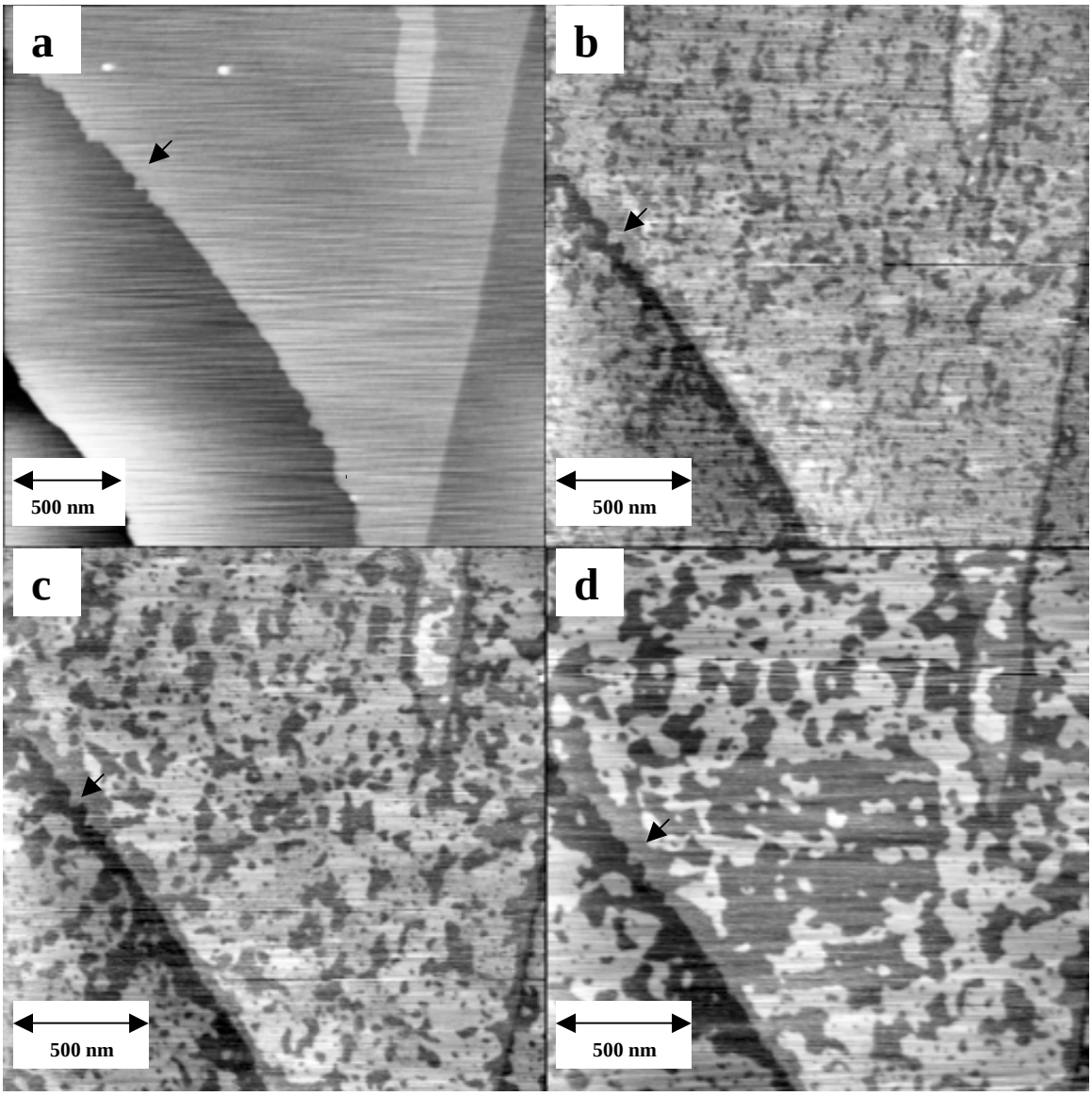

Fig. 14. Sequence of TMAFM images obtained before and during the acidic dissolution of manganite. a) In-air image of a fresh manganite surface (t = 0). b) Same area as (a), except slightly magnified, obtained in-solution, after 13 min of exposure to pH 3.5 HNO_3. Although pitting of the terraces is widespread, dissolution is more rapid along step edges, as evidenced by the laterally continuous pits extending parallel to these edges. c) Continued dissolution (t = 25 min) has occurred primarily at step edges causing the pits seen in (b) to become broader. A tip radius of ~5 nm can be estimated from the diameter of the smallest resolvable pit (~10 nm). At least 5 terrace levels are identified, each of which is vertically offset by 0.5 ±0.1 nm. d) After 60 min. of exposure (image area shifted up ~200 nm), many of the pits seen in (c) have now coalesced. The arrows shown in each image mark a feature which persists throughout the reaction with little to no dissolution. Tip-enhanced dissolution caused during a previous 1.0 μm scan is apparent in the central portion of the image.

CHAPTER 2: Comparison of the Reactivity of Various Mn-Oxides with Cr^{III}_{aq}: Microscopic and Spectroscopic Observations of Dissolution, Cr-sorption and Cr and Mn Redox Interactions

Abstract

The interaction between Cr^{III}_{aq} and seven different Mn-oxides (6 monomineralic, 1 synthetic) has been observed in pH 4.4 HNO_3 and pH 4.4 ~10^{-4} M Cr^{III}_{aq} solutions. For each mineral-solution interaction, the aqueous chemical concentrations (e.g. $[Mn]_{aq}$, $[Cr]_{aq}$, $[Cr^{VI}_{aq}]$) were measured with time. Reacted samples were examined by XPS to determine if, and to what extent, the surface chemical states of Cr, Mn and O had changed. Microscopic observations of the reacted surfaces were obtained using AFM and high-resolution, low-voltage FESEM. The solubility of the Mn-oxides in the acidic, non-Cr bearing solutions varied inversely with the average Mn valence, but did not show systematic behavior with respect to the mineral structure type (e.g. tunnel, layer, framework). This trend was interpreted as resulting from the relative ability of an adsorbed proton to polarize surface Mn-O bonds, with the polarizability being in the order Mn^{2+}-O > Mn^{3+}-O > Mn^{4+}-O. For samples reacted with Cr^{III}_{aq}, the rate and extent of reductive dissolution was always greater than for acidic dissolution during the initial time period. The measured ratios of the $[Mn]_{aq}$: $[Cr^{VI}]_{aq}$ were approximately in agreement with the values expected from the proposed stoichiometric reactions. Cr-uptake was observed to occur in undersaturated solutions as a result of adsorption, absorption and surface catalyzed precipitation. The chromium as detected by XPS was predominately Cr^{III}, however pyrolusite contained both Cr^{III} and Cr^{VI}. Previous studies have implicated a chromium surface precipitate to be responsible for the cessation of the Cr^{III}_{aq} oxidation reaction. Our surface sensitive FESEM and AFM observations tend to suggest that Cr-uptake is by isolated site binding, very small (<30 nm) surface clusters or monolayer scale films. Cr-uptake was followed by slow Cr-release on several of the solids (particularly the layered solids) after a substantial portion of the total aqueous Cr had been converted to Cr^{VI}_{aq}.

The oxidizing ability of the different Mn-oxides for Cr^{III}_{aq} is evaluated with regards to the energy level of the redox couple (i.e. the redox potential) as compared with the Fermi energy

level of the Mn-oxide. Although these energies were calculated rather than directly measured, the results indicate that electrons originating from adsorbed Cr^{III} ions may be transferred into the conduction band or more likely, into available surface states. The presence of an initial limited quantity of electron accepting surface states likely explains the observation of a rapid initial Cr^{III}-oxidation followed by much slower oxidation. The Mn-oxides that exhibited the greatest and longest lasting Cr^{III}-oxidizing power were the Mn-oxides containing Mn^{3+}, and in particular those containing Mn^{3+} and Mn^{2+}. It is believed that the combined presence of a reducible Mn ion (e.g. Mn^{3+}) and a highly soluble Mn^{2+} ion facilitates a sustained Cr^{III}-oxidation reaction because fresh surface is exposed during the reaction.

7. INTRODUCTION

Manganese oxides are widely known as strong metal sorbents/scavengers and oxidizers, resulting in great interest in the role that they play in the fate of toxic metals in nature, as well as potential and realized applications in waste water treatment and reactive barriers in soils (e.g. Jenne, 1968; Murray, 1975; Means et al., 1978; Merkle et al., 1996). One metal in particular, chromium, has attracted a large amount of attention with regards to Mn-oxides because these minerals are the most notable naturally occurring inorganic phases capable of oxidizing Cr^{III}_{aq} to Cr^{VI}_{aq} (Eary and Rai, 1987). This is of concern because Cr^{VI}_{aq} is both more labile and more toxic than its reduced counterpart. Overall, Cr is the most common redox-active inorganic groundwater contaminant in the United States and in many other industrialized countries around the world (Nriagu et al., 1988; Kavanaugh, 1994).

The primary goal of this study is to determine and attempt to explain the similarities/differences in the Cr^{III}_{aq} sorption/oxidation characteristics of various Mn-oxides. A large variation in reactivity is expected because the Mn-oxides encompass a structurally diverse set of oxides, hydroxides, oxyhydroxides, and hydrous mineral phases (Post, 1992). Mn-oxides may be of the layer, tunnel, or framework structure types that are assembled of edge and corner sharing Mn-octahedral and tetrahedral building blocks. In terms of valence, the Mn-oxides are equally diverse with manganese occurring in divalent, trivalent or tetravalent states, or occurring simultaneously in multiple valence states. There is perhaps no other group of minerals that exhibits such diversity in structure and valence with such little variation in chemical composition.

We also felt it important to use as many natural Mn-oxides, as opposed to synthetic analogs, as possible. Natural samples typically have more complex minor and trace element chemistries, as well as potentially more surface and bulk defect structures, both of which could lead to differences in reactivity. Most previous studies have used synthetic Mn-oxides (in the following list of references, '*' indicates that natural vs. synthetic has not been specified, 'B' indicates both have been used, and no designation means the study has used only synthetic samples: Schr.oeder and Lee, 1975*; Basak and Malati, 1977; Amacher and Baker, 1982[B]; Rophael and Boulis, 1982; Eary and Rai, 1987; Bartlett and James, 1988*; Manceau and Charlet, 1990*, 1992*; Johnson and Xyla, 1991; Fendorf and Zasoski, 1992; Fendorf et al., 1992, 1993a, 1994; Bidoglio et al.,

1993; Chung et al., 1994; Silvester et al., 1995; Chung, 1998; Kim and Moon, 1998; Malati and Rophael, 1999; Banerjee and Nesbitt, 1999). This is at least partially due to the difficulty of collecting these phases in monomineralic form. Natural Mn-oxides are typically exceptionally fine grained and intimately mixed with other minerals, either as coatings on rocks and minerals or highly disseminated in soils (Hem, 1964; McKenzie, 1980; Crerar et al., 1980; Singh, 1984). Nevertheless, through extensive searching, we were able to obtain five pure and one impure Mn-oxide minerals (Table 1). Birnessite, a very important Mn-oxide that we and several other research groups have failed to find in a monomineralic form, was synthesized and also included in this study. Taken collectively, all of these samples possessed tunnel, layer, or framework structures and had an average Mn valence that range from 2.67 to 4.0.

To compare and contrast the reactivities of these various Mn-oxides with Cr^{III}_{aq}, we monitored the aqueous concentrations (by inductively coupled plasma spectroscopy, ICP) and Cr^{VI}_{aq} speciation (by ultraviolet-visible spectrophotometry, UV-Vis) in batch reactor runs, and performed surface imaging (low-voltage field emission scanning electron microscopy, FESEM, and atomic force microscopy, AFM) and chemical analysis (X-ray photoelectron spectroscopy, XPS, and energy and wavelength dispersive spectroscopy, EDS and WDS) on the sorbent surfaces before and after reaction.

A standard set of experimental conditions (e.g. 0.01M $NaNO_3$, pH ~4.4, 10^{-4} M $CrOH^{2+}_{aq}$ which is, ~5.2 ppm Cr^{III}_{aq} and ~0.5g Mn-oxide/L) was chosen so that our results could be easily compared with the existing literature. Deviations from these conditions were necessary for birnessite because of its very rapid Cr^{III}-oxidation reaction, and for lithiophorite, because of the quantity of available sample. Conditions close to those stated above have been widely used in other studies so that: 1) the rate of reactions are sufficiently slow for convenient sampling, 2) the detection limit is not an issue and, 3) the solutions are undersaturated with respect to $Cr(OH)_{3(s)}$. It should be noted that these experimental conditions are generally not adopted for the purpose of reproducing environmental conditions, although such conditions do exist in nature.

8. MATERIALS AND METHODS

8.1 Chemicals and Solutions

All solutions were prepared from chemicals of at least reagent grade and using distilled, deionized water (H_2O_{DD}) obtained from a Millipore Synthesis A10 water system (18.2 MΩ, < 8 ppb total organic carbon (TOC), UV light treated, ultrafiltration membrane, 0.2 μm filtered). All glassware and high-density polyethylene (HDPE) containers were rinsed with acid (0.01M HNO_3) and water before use. Cr^{III}_{aq} solutions were prepared fresh (< 4 hours) for each experiment using $Cr(NO_3)_3 \cdot 9H_2O(s)$ and 0.01M $NaNO_{3aq}$. Solution pH adjustments before and during the experiments were made using 1 N HNO_3 and 10 N NaOH. All experiments were conducted at room temperature (23 ± 2° C) and solutions were in equilibrium with air. Although it has been shown that Cr^{III}_{aq} is not significantly oxidized by O_{2aq} (Schr.oeder and Lee, 1975; Van Der Weijden and Reith, 1982; and Eary and Rai, 1987), we tested for Cr^{VI}_{aq} by UV-Vis in fresh and 95 day old 10^{-3} M Cr^{III}_{aq} solutions and found less than 10^{-7} M (< 5 ppb) Cr^{VI}_{aq}.

8.2 Mineral characterization and preparation

Mn-oxide samples were obtained from the National Museum of Natural History (NMNH) of the Smithsonian Institution and the Virginia Polytechnic Institute and State University (VPI&SU) museum, as well as collected from various Virginia localities and synthesized in the laboratory. The mineralogy and chemistry of each sample was determined by X-ray diffraction (XRD), energy dispersive spectroscopy (EDS) and for some samples, wavelength dispersive spectroscopy (WDS). Samples were used in experiments as mineral powders or as ~0.5 mm^3 sized cleavage or fracture fragments. Powders for all of the samples except the synthetic birnessite and lithiophorite were prepared by crushing larger fragments to less than 0.5 mm in a percussion mortar and then grinding (with H_2O_{DD}) for ten minutes in a McCrone micronizing mill. Although any type of grinding should be considered an aggressive form of preparation, grinding in this type of mill is performed primarily by less destructive shear forces. The birnessite sample was synthesized according to procedure #1 of McKenzie (1981), and was not micronized. Due to a limited supply of lithiophorite, grinding was performed by mortar and pestle. Compared to the other powders, the lithiophorite was observed to be slightly coarser and of less uniform grain size. A surface area of 8.0 m^2/g was estimated based on a comparison of the grain size and shape with the other Mn-oxides. For all of the other powders a BET surface

area was measured. For all Mn-oxides except birnessite, cleavage or fracture surfaces were exposed by applying pressure with a pestle or scalpel, or for lithiophorite, by cleaving along the basal plane with a scalpel and tweezers. Table 1 summarizes the results of our characterizations and also lists some additional properties of each Mn-oxide.

8.3 Batch experiments with powder samples

8.3.1 General comments

The release of Mn from each Mn-oxide was measured (in triplicate) in the presence and absence of Cr^{III}_{aq}. For the experiments performed in the presence of Cr^{III}_{aq}, total aqueous chromium (i.e. $[Cr]^{T}_{aq}$) and chr.omate (i.e. $[Cr]^{VI}_{aq}$) concentrations were also measured. In these experiments, reactions were conducted in 500 mL HDPE bottle "reactors" which had been drilled at their base and fit with a luer fitting and tygon hose through which samples could be extracted by syringe. The reactors were continuously agitated by wrist-action, except for short periods during pH adjustment. Additional experiments performed using cryptomelane and hausmannite (chosen because of their highly different solubilities) conducted at significantly faster and slower shaking speeds suggested that the Cr^{III}_{aq} oxidation rate was not limited by transport phenomena. This is in agreement with investigations by Stone and Morgan (1987) who have shown that Mn-oxide dissolution is a surface controlled process. Sampling took place at prescribed times and while under agitation, so it was assumed that the solid to solution ratio was approximately maintained throughout the experiment. Samples were immediately filtered through 0.2 μM nitrocellulose or polycarbonate and stored in capped HDPE centrifuge tubes prior to UV-Vis or ICP analysis. Remeasurement of the $[Cr^{VI}]_{aq}$ in the filtered solutions after 4 days showed that filtration was successful at stopping the reactions. This reanalysis also showed that the HDPE container did not absorb Cr^{VI}_{aq}. Resealable filter holders (Millipore, Swinex) were used in all experiments so that the dried Mn-oxide could be easily recovered from the filter for subsequent chemical analysis (WDS and XPS) and also for use in a second Cr^{III}-oxidation experiment designed to investigate the initial Cr^{III}-oxidation rate behavior.

8.3.2 UV-Vis and ICP

Cr^{VI}_{aq} concentrations were measured using 0.1% s-diphenylcarbazide and a Beckman-Coulter 640DU UV-Vis spectrophotometer. The 0.1% s-diphenylcarbazide solution was diluted from certified 0.5% s-diphenylcarabzide in 99.5% acetone using 0.01 M $NaNO_3$ and acidified with 0.1 mL, 5N H_2SO_4. Each 0.1 mL sample was combined with 1 mL of 0.1% s-diphenylcarbazide in a 1 cm methacrylate cuvet. Using this sample to reagent ratio, color development was complete and stable in less than 3 minutes. Samples were read and the absorbance maximum at 543 nm was verified in fixed and scanned wavelength modes, respectively. The absorbance of each cuvet containing a blank sample was checked regularly so that inter-cuvet absorbance variability could be subtracted. The uncertainty on replicate measurements of Cr^{VI}_{aq} standards was ± 10 ppb.

Total aqueous manganese and chromium were determined by ICP using a Spectro Analytical Instruments SpectroFlame (type FTMA85D). All such measurements represent the average of three measurements with an uncertainty of ± 25 ppb.

8.3.3 Acidic dissolution experiments

All of the Mn-oxides except lithiophorite were reacted at 0.5 g/L solid to solution ratio. Due to a lack of sample, the lithiophorite was reacted at 0.1 g/L. Experiments were initiated by adding a weighed mass of Mn-oxide to pH 4.4, 0.01 M $NaNO_3$. Prior to any sampling, the pH of several of the suspensions fluctuated so that frequent pH adjustments were required during the first two hours of reaction. For example, the pH of the manganite suspension increased to ~10.2 within 5 minutes, the birnessite solution increased to pH ~5.3 and the hausmannite solution increased to pH ~5.2. Only the hausmannite suspension could not be stabilized at pH 4.4 ± 0.15 over the course of the experiment. This behavior of the hausmannite suspension resulted from the dissolution of witherite ($BaCO_3$) impurities that were identified by SEM/EDS, and so a pH of 5.2 was maintained instead. The first sample was withdrawn after 3 hr., when the drift in pH had diminished substantially

8.3.4 Reductive dissolution in the presence of Cr^{III}_{aq}

In the reductive dissolution experiments the solid was hydrated in a pH 4.4, 0.01 M $NaNO_3$ solution for 10 hr. prior to the addition of the Cr^{III}_{aq}. After the 10 hr., a sample was taken to record the initial manganese concentration due only to acidic dissolution (i.e. $[Mn]^{A}_{aq}$). Immediately after this sample was obtained, the reductive dissolution experiment was initiated by adding 200 mL of pH 4.4, $2x10^{-4}$ M $CrOH^{2+}_{aq}$. In the case of birnessite, an additional experiment was performed at a much lower solid to solution ratio of 0.02 g/L, so that the rate of Cr^{VI}_{aq} production would be significantly slower, thus allowing for more samples before all of the Cr^{III}_{aq} was oxidized.

8.3.5 Re-reaction of Mn-oxides with Cr^{III}_{aq}

In all of the reductive dissolution experiments, except those performed with lithiophorite, enough reacted solid could be scraped from the filter papers to perform an additional batch experiment. The purpose of this experiment was to determine if the reacted Mn-oxide would be less effective towards Cr^{III}_{aq} oxidation when returned to the same starting conditions of the original reductive dissolution experiments. In this experiment, 2 to 10 mg of the Cr-reacted Mn-oxide powder (80 hr. sample, air dried ~25 days) was hydrated with 15 mL of pH 4.4, 0.01 M $NaNO_3$ in a 50 mL HDPE centrifuge tube. After 10 hr. of hydration, a 5 mL sample was taken to record the initial Cr^{VI}_{aq} concentrations and 15 mL of pH 4.4, $1.66 x10^{-4}$ M $CrOH^{2+}_{aq}$ was added. This brought the solutions to the same starting conditions as used in the original reductive dissolution experiments (i.e. pH 4.4, 10^{-4} M $CrOH^{2+}_{aq}$). As mentioned above, the dissolution of barite impurities in the hausmannite resulted in a constant pH of 5.2 ± 0.15. Four samples were taken at prescribed intervals, filtered and analyzed for Cr^{VI}_{aq}.

8.4 Microscopic and spectroscopic observations of reacted Mn-oxide surfaces: Dissolution and Cr-uptake

8.4.1 General comments

In order to obtain microscopic (AFM and FESEM) observations from the surfaces of acid and Cr^{III}_{aq} reacted Mn-oxides, additional experiments were performed using larger samples that were cleaved or fractured as described above. Birnessite could not be investigated in this way because of its very fine grain size. Lithiophorite was the only sample on which AFM fluid-cell results were obtained. Lithiophorite samples were rinsed under a high velocity $N_{2(g)}$ stream to remove fine cleavage dust, then mounted on glass using C-paint, initially imaged by AFM in air and then imaged in acidic solution (pH 4.4, 0.01 M $NaNO_3$) or Cr^{III}_{aq}-containing (pH 4.4, 10^{-4} M $CrOH^{2+}_{aq}$) solution. The fluid cell was purged with fresh solution at least once every 30 minutes. Imaging was performed in non-flowing solutions.

For ex-situ AFM and FESEM observations, the samples were sonicated in H_2O_{DD} for ~1 min to remove some of the fine particles adhering to the surfaces. After sonicating, the samples were transferred to HDPE vessels containing ~15 mL of acid (pH 4.4, 0.01 M $NaNO_3$) or Cr^{III}_{aq} (pH 4.4, 10^{-4} M $CrOH^{2+}_{aq}$) and reacted under agitation. Grains were removed at specified times, placed in a Millipore Swinex filter holder, exposed to a high velocity stream of $N_{2(g)}$ to remove excess solution and mounted for FESEM and AFM imaging.

For each Mn-oxide at least one reductive dissolution experiment was performed in which a weighed mass of Mn-oxide (usually ~3-10 grains) was added to 1.0 mL of pH 4.4, 10^{-4} M $CrOH^{2+}_{aq,}$ in a 1.5 mL HDPE microcentrifuge tube and shaken. At prescribed times, 0.1 mL of solution was removed for Cr^{VI}_{aq} measurement and a grain of the Mn-oxide was also removed. The purpose of the Cr^{VI}_{aq} measurements was only to gauge the extent of reaction and not for direct comparison with the results of the powder experiments. After ~ 80 hr., the remaining Mn-oxide grains were removed, dried under $N_{2(g)}$ and imaged by FESEM. For the lithiophorite, samples were removed after 0.1 and 13 hr. After mounting, the lithiophorite (13 hr. sample) was cleaved parallel to (001) to expose an interior surface. This new surface, as well as the original exterior surface and the lithiophorite sample reacted for 0.1 hr., were analyzed by XPS. The Al

disk onto which each lithiophorite crystal was mounted was first coated with carbon paint so that only the sample and adjacent carbon would be detected.

8.4.2 Atomic force microscopy

AFM images were collected with a Digital Instruments Nanoscope IIIa Multimode Atomic Force Microscope, operating in either air or aqueous solution, and in contact or Tapping® mode (TMAFM). The XY scale was calibrated with a 1 μm standard and the Z scale was calibrated against the basal spacing of mica (i.e. 0.995 nm). AFM probes used in this study have a Si tip (nominal radius ~20 nm) on a 100 μm SiN_3 cantilever. The acrylic AFM fluid cell holds ~0.03 - 0.07 mL , depending on the sample size and the degree of silicone o-ring compression (see Johnsson et al., 1991 for cell schematic).

8.4.3 Field-emission SEM, EDS & WDS

SEM imaging and EDS was performed with a LEO 1550 FESEM with Kevex EDS detector. When operated at low accelerating voltage (e.g. <5 kV) and utilizing the 'SE^I' type detector, a lateral resolution of <5 nm and a vertical resolution (or surface sensitivity) of <10 nm was achieved on all samples (with no conductive coating). The very high spatial resolution results from fact that as the accelerating voltage is decreased, the volume of sample from which the total electron signal (i.e. backscatter electrons (BSE) and secondary electrons (SE^I & SE^{II}) originates decreases. This results in a greater percentage of the detected electrons having been derived from an area closely localized around the impact point of the primary electron beam. In a greatly simplified definition, SE^I type electrons originate within a few nanometers of the beam impact point and SE^{II} type electrons originate from an area up to several microns from the point of beam impact (see Goldstein et al., 1992). It is therefore obvious that the SE^I type electrons contain an inherently higher spatial resolution signal. The 'SEI' detector utilized by the LEO1550 is optimized for the collection of this SE^I component of the total electron signal. Since the signals being detected are of a highly surface sensitive nature, contrast mechanisms not apparent at conventional SEM conditions (i.e. >10kV, SE^{II} detector), can be detected and are

often quite dramatic. Typical contrast mechanisms exhibited in low voltage SE^I images are topographic, electronic and chemical in nature.

Wavelength dispersive spectroscopy (WDS) was performed with a Cameca SX-50 electron microprobe. The conditions of the analysis were: 15kV, 20nA, 5 μm spot size, count time of 120 sec on the peak of interest (i.e. $CrK_{\alpha 1}$ or $MnK_{\alpha 1}$) and 45 sec on either side for background measurement. Although the instrument was calibrated for quantitative analysis, the results are expressed on a relative scale (cps) with an uncertainty of ± 0.1 cps. Samples were analyzed on filters after having been carbon coated.

8.4.4 X-Ray Photoelectron Spectroscopy

X-ray photoelectron spectroscopy (XPS) was performed using a Scienta ESCA-300. The ESCA-300 represents the premier of all commercially available XPS instruments and can outperform some second-generation synchrotron XPS instruments, both in terms of monochromatic X-ray flux and energy resolution (Barr, 1994). The instrument utilizes a finely focused electron gun, rotating Al anode and seven strategically bent and placed quartz crystals to create a high flux of monochromic Al K_α X-rays (1486.6 eV). The energy resolution is optimized by the combined geometry of the anode, quartz monochromators and sample, and also through the use of a high-resolution electrostatic lens, 300 mm diameter photoelectron analyzer and microchannel plate detector. High-resolution narrow scans of the $Mn2p^{3/2}$ were collected with a step size of 0.05 eV. Narrow scans of the $Cr2p^{3/2}$, O1s, C1s and Mn3s were collected with a 0.1 or 0.15 eV step size. In both cases the pass energy was 150 eV. When required a flood gun was used to compensate for charging. Pressures during analysis were typically ~10^{-9} Torr.

Sample preparation for XPS analysis consisted of scraping the Mn-oxide from the filter and pressing it into a Sn foil. The time between filtering and XPS analysis ranged from 3 to 35 days depending on the sample. Pressing was performed < 24 hours prior to introduction into the XPS instrument.

9. RESULTS AND DISCUSSION

9.1 Acidic dissolution

Because the pH in several of the reactors was not stable during the first two hours of reaction it was decided to reset the time and $[Mn]_{aq}$ scales relative to the time the first sample was collected (i.e. after 3 hr. of reaction at pH $\geq$ 4.4). Resetting these scales was also performed because the dissolution rates at the onset of reaction were more rapid and thus may not accurately represent the material's intrinsic bulk solubility. Rapid initial dissolution behavior is a common observation in mineral dissolution experiments and may be attributed to intrinsic surface properties (e.g. soluble surface sites, defects) or the sample's preparation style and history . After normalization, the data were fit to an equation in order to allow us to: 1) infer the $[Mn]_{aq}$ component released during the reductive dissolution experiments, and 2) obtain acidic dissolution rates by numerical integration (Pollard, 1977).

The acidic dissolution results (Fig. 1a) show two important behaviors: 1) the dissolution rates decrease very rapidly, and 2) the Mn-oxides of lower average Mn valence dissolve much faster and to a greater extent than those of higher average Mn valence. The bold lines in Figure 1a show fits to the raw data. These fits were used to calculate the dissolution rates as a function of $[Mn]_{aq}$ (Fig. 1b). For any given Mn-oxide, the rates can be seen to decrease with increasing $[Mn]_{aq}$, but the dissolution rates vary greatly for different Mn-oxides at the same Mn_{aq} concentration. A comparison of the final $[Mn]_{aq}$ with cited solubility products (K_{sp}) for hausmannite, manganite and pyrolusite shows the solutions to be well undersaturated with respect to each mineral phase (Table 2). In fact, the most Mn_{aq}-saturated solution (i.e. hausmannite, SI = 0.54) displays the fastest dissolution rates. SEM and AFM observations were consistent with these findings and no evidence for any accumulation of reaction products was seen. However, our data offer no insight as to whether or not Mn_{aq} present in the diffuse layer may inhibit the approach or attachment of H^+ by an electrostatic mechanism. Regardless, these observations strongly suggest that the Mn-oxide dissolution rates were not significantly affected by $[Mn]_{aq}$. This claim does not contradict any previous findings on the acidic dissolution of pyrolusite (Eary and Rai, 1987) or δ-MnO_2 (birnessite-like) (Murray, 1974). Two alternative explanations for the rapid decrease in the dissolution rates that are supported by microscopic observation are: 1) the early and rapid dissolution of ultra-fine particles and general rounding of sharp corners and protrusions (Nielsen, 1964). SEM images of the unreacted Mn-oxides show

that in most samples there was approximately a 100x difference between the radius of the largest (~1000 nm) and smallest (~10 nm) particles), and 2) the early and rapid preferential dissolution (i.e. pitting) and enhanced dissolution in certain crystallographic directions (i.e. etching).

Preferential dissolution at highly soluble surface sites may also explain the initial rate behavior. These sites may be an inherent trait of the mineral due to chemical or structural attributes (e.g. ordered vacancies, density of specific surface terminations, reduced metal substitutions) or may result from the sample's preparation style or exposure history (e.g. grinding or fracturing method, time exposed to atmosphere or hydrating/ etching/ washing solution, presence of reduced or oxidized surface layers). Given that Mn-oxides are often nonstoichiometric due to reduced Mn or other metal substitutions and vacancies (Post, 1992) and that their surfaces fresh or reacted surfaces can be oxidized or reduced even under mild conditions (e.g. drying, warming, freezing, thawing, moist storage, dry storage, rinsing with water) (Amacher and Baker, 1988; Ross et al., 2001a), it is probable that surface sites of variable solubility were initially present.

By considering that as dissolution proceeds, there is a progressive change in the structural environment of a Mn ion from a bulk crystallographic site, to a surface ion and then to an aqueous ion, we can utilize the bulk crystallographic properties to predict which sites are expected to be preferentially soluble. Crystal-chemical relations will demonstrate that solubility correlates with the Mn-O bond strength and the polarizability of the Mn cation. For example, hausmannite has a spinel structure with two distinctly different types of Mn sites: 1) 4-coordinated Mn^{2+} and, 2) 6-coordinated Mn^{3+}, with the Mn^{3+} being twice as abundant. Although the Mn^{3+}-oxygen bond and the Mn^{2+}-O bond have the same Pauling bond strength, the Mn^{2+}-O bond is generally longer (Chartier et al., 1999, Table 1 footnote f). Since bond lengthening usually results in bond weakening, it makes sense to factor bond length into the Pauling bond strength (σ). This has been done by simply dividing σ by the Mn-O bond lengths for Mn^{2+}-O (0.223 nm), Mn^{3+}-O (0.204 nm) and Mn^{4+}-O (0.189 nm) (Shannon, 1976; Palenik, 1997). The new measure of relative bond strength (i.e. 'σ/l', Table 1) now shows the Mn^{2+}-O to be weaker. As a result, the Mn^{2+}-O bond should be more easily polarized by an adsorbed proton, and thus more likely to cleave from the mineral into solution (i.e. dissolve). This allows for the possibility that with continued dissolution, the more soluble Mn^{2+} sites are preferentially removed and the surface becomes more enriched in the Mn^{3+} sites. The Mn^{2+}/Mn^{3+} ratio is not

expected to change dramatically though because as the surface is dissolved new Mn^{2+} sites are exposed. $Mn2p^{3/2}$ XPS spectra of the hausmannite reacted surfaces support this conjecture by showing a slight enrichment in the Mn^{3+} component at 640.9 eV after 260 hours of reaction (Fig. 4A1). Several of the other Mn-oxides (e.g. pyrolusite, lithiophorite) also show depletion in the abundance of the lower valence Mn, however, manganite shows no change (Weaver and Hochella, in review). This different behavior for manganite results because it contains only Mn^{3+} ions, so once these ions are released to solution an underlying Mn^{3+} site is exposed and there exists no possibility for enrichment in the surface Mn valence (i.e. it can only remain the same).

FESEM observations of lithiophorite and hausmannite crystals, show that dissolution often produced a crystallographically influenced etch pattern (Figs. 3c, 5a). Although etch patterns are large compared to atomic sites, they are a manifestation of an atomic scale dissolution rate anisotropy. That is, different directions in the crystal, which correspond to different chemical or bonding geometries, are dissolved at different rates. This dissolution anisotropy has produced a triangular pattern of intersection ridges on hausmannite (Fig 5a). In-situ and ex-situ AFM experiments on lithiophorite dissolution showed that most of the dissolution probably occurred before the first image was collected (~5 min.), because observations of the same area for up to 2 hr. showed no change in dissolution pit size (Fig. 3e). This behavior implies that the initial dissolution took place at some site of near atomic dimensions and rapidly expanded until the step edges were pinned by relatively insoluble sites. Although the basal edges of lithiophorite are too rough to image by AFM, high-resolution FESEM images show them to have become pitted (Fig 3a, inset). Bickmore et al. (2001), and references therein, have shown that the edge sites on layer silicates are far more soluble than the basal surfaces.

It should be noted that the size of the AFM scans was not nearly sufficient to evaluate the extent to which the dissolution (acidic or reductive) was spatially heterogeneous (Fig. 3c). The dissolution heterogeneity depicted in Fig. 3c extends over tens of microns with the brightest terraces (denoted B) exhibiting the most extensive pitting and the darker terraces (denoted D) the least. The medium shaded terraces (denoted M) show that anisotropic dissolution has produced pits along a lineation (parallel to arrows). The variable contrast of the terraces is not due to topography, but likely results from a difference in the near surface average atomic number (i.e.

chemistry, analogous to a near surface backscatter electron image). Fig. 3b depicts this spatial distribution of contrast to a much greater degree (see section 3.3 for more discussion).

The surfaces of the Mn-oxides of higher average Mn valence did not show any obvious localized dissolution features. However this was not unexpected given their very low solubilities. Mass balance calculations show that to account for the observed $[Mn]_{aq}$ in each dissolution experiment (except hausmannite), less than 1 monolayer of dissolution would be necessary. This suggests that dissolution features would be rare and if present, then very subtle.

9.1.1 Dissolution mechanism

The data support the view that protons promote dissolution by polarizing the Mn-O bond to such a degree that it is broken, with the Mn and O released to solution. This is best demonstrated by comparing the dissolution behaviors of hausmannite, manganite and pyrolusite. These solids make a good comparison because they are very similar in composition, but vary significantly in terms of their Mn valence, Mn-O bond properties and bulk solubility. The Mn^{2+}-O bonds in hausmannite are generally longer and should therefore contain less electron density along the bond path than the shorter Mn^{3+}-O or Mn^{4+}-O bonds in manganite and pyrolusite, respectively. The increased length and lower charge of the Mn^{2+}-O bond causes it to be weaker in an acidic solution because the electrons contained along the Mn-O bond are more susceptible to being polarized towards an adsorbed, electrophilic H^+ ion. In the bulk structures of hausmannite and manganite, the $[Mn^{3+}O_6]$ octahedra are expected to be weaker than the $[Mn^{4+}O_6]$ octahedra in pyrolusite because they contain less charge (and thus a lower σ/l, Table 1) and are highly distorted by Jahn-Teller (i.e. crystal field splitting) effects (Burns, 1970). Recent *ab-initio* calculations for hausmannite show the apical Mn^{3+}-O bonds to be ~16% longer than the equatorial Mn^{3+}-O bonds (Chartier et al., 1999). These theoretical values are in good agreement with experimental values (Boucher et al., 1971). In manganite, bond length distortions are even greater, with apical Mn^{3+}-O bonds up to 25% longer (Dachs, 1963). The situation for manganite is also complicated by the presence of the complex anion OH^-. Since this anion is polar, it would also have the effect of decreasing the bond strength through polarization. This observation suggests it would be interesting to compare the dissolution behavior of Mn_2O_3 with γ-MnOOH.

The explanation that the polarizability of a bond increases it susceptibility towards dissolution has been previously proposed (Furrer and Stumm, 1986; Stumm and Wieland, 1990; Stone and Morgan, 1987; Wehrli et al., 1990). The present data clearly support this simple explanation with a suite of chemically similar minerals with broadly varying structures and average manganese valences.

9.2 Coupled Cr^{III}_{aq} oxidation and Mn-oxide reductive dissolution

Figure 6 shows the results of the batch reactor experiments where Cr^{III}_{aq} is reacted with the seven Mn-oxides used in this study. As it was standard procedure to hydrate the Mn-oxide prior to the reductive dissolution experiments, the $[Mn]_{aq}$ was elevated at the onset of reaction due to acidic dissolution. For this reason, the measured Mn_{aq} concentrations resulting from simultaneous reductive and acidic dissolution processes (i.e. $[Mn]^{R+A}$) are presented with this background $[Mn]_{aq}$ component subtracted (Fig. 6). Also plotted are the acidic dissolution data (i.e. $[Mn]^{A}_{aq}$) and calculated values for the reductive dissolution component (i.e $[Mn]^{R}_{calc.} = [Mn]^{R+A} - [Mn]^{A}_{calc.}$). It was necessary to use calculated $[Mn]^{A}_{calc.}$ values for this subtraction because the sampling times for the reductive and acidic dissolution experiments were different. The Cr concentrations (i.e. $[Cr]^{T}_{aq}$, $[Cr^{VI}]_{aq,}$) are expressed with the Mn_{aq} concentrations on the left y-axis in M/m^2, and are also expressed in terms of the initial $[Cr]^{T}_{aq}$ (i.e. 10^{-4} M) on the right y-axis (Fig. 6). Note that the 100% mark on the right y-axis extends to the same height as the initial $[Cr]^{T}_{aq}$ on the left y-axis. Shading has been used to delineate the relative amounts of Cr-uptake (dark), Cr^{VI}_{aq} (light) and Cr^{III}_{aq} (white). Also plotted in Figure 6 are the results from the experiments in which the Cr-reacted Mn-oxide powders (80 hr. samples) were reacted for a second time, in a fresh Cr^{III}_{aq} solution (labeled '$[Cr^{VI}]_{aq}$ 2' in legend).

In general, each reaction depicted in Fig. 6 displays an initial period of rapid reductive dissolution coupled with the rapid oxidation of Cr^{III}_{aq} to Cr^{VI}_{aq}. The longevity of this initial period, and the rate and extent of the overall reactions, vary greatly for the different Mn-oxides. This general kinetic behavior has been observed in many previous studies (Schr.oeder and Lee, 1975; Basak and Malati, 1977; Rophael and Boulis, 1982; Amacher and Baker, 1982; Eary and Rai, 1987; Johnson and Xyla, 1991; Fendorf and Zasoski, 1992; Silvester et al., 1995; Kim and

Moon, 1998; Chung, 1998), and therefore suggests that this behavior is demonstrated regardless of the initial solution conditions and sample preparation history. This is a very significant observation in that it strongly suggests that the initial Cr^{III}-oxidation rate behavior (i.e. initially very rapid then considerably slower) is due to a property of the Mn-oxide surface that is to some extent, independent of the variety of the Mn-oxide.

Also, the distribution of chromium between its various aqueous (e.g. Cr^{VI}_{aq}, Cr^{III}_{aq}) and solid forms (e.g. sorbed or precipitated chromium) varies greatly with time and with the type of Mn-oxide. This is demonstrated in each of our data sets (Fig. 6a-h) by the height of each shaded region at a given time (note that not all plots are at the same scale). For example, hausmannite (Fig. 6a) shows that after ~1 hr. of reaction ~85% of the initial Cr^{III}_{aq} has been either oxidized to Cr^{VI}_{aq} (lightly shaded region) or removed from solution (darkly shaded region). This point in time is also marked by a decrease in the slope of the $[Mn]^{R+A}$. Pyrolusite (Fig. 6h) shows a much different behavior, with far less Cr-oxidation and Cr-uptake with time. The amount of Cr-uptake and Cr-oxidation by the different Mn-oxides is summarized by considering only three times, 5 min, 1 hr. and 80 hr. (Fig. 7). For example, after only 5 min. of reaction, hausmannite has oxidized nearly 20% of the ***initial*** Cr^{III}_{aq} whereas, in the same amount of time pyrolusite has oxidized only 2%. After 80 hr. of reaction, these percentages increase to 62% for hausmannite and to 11% for pyrolusite. When assessing the extent of Cr^{III}_{aq} oxidation by the different Mn-oxides, it makes sense to distinguish between the extent of Cr^{III}-oxidation relative to the ***initial*** total aqueous chromium concentration (i.e. $[Cr]^{T}_{aq\ t=0}$) and the extent of Cr^{III}-oxidation relative to the ***current*** chromium concentration (i.e. $[Cr]^{T}_{aq\ t=n}$). This distinction is most important when a significant amount of Cr-uptake has occurred. Reconsidering the above example for hausmannite (Fig. 6a), it can be seen that after ~1 hr. there is < 10% of the initial $[Cr^{III}]_{aq}$, now available for sorption and subsequent oxidation. After this time (i.e. ~ 1 hr.), there is a slow (but steady) increase in Cr^{VI}_{aq} and Cr^{T}_{aq}, which is inevitably linked to a slower rate of oxidation for some of the surface sequestered chromium. With this effect of Cr-uptake on the current $[Cr^{III}]_{aq}$ in mind, the comparison made above between hausmannite and pyrolusite now shows that after 5 minutes, 23% of the $[Cr^{III}]_{t=5min}$ has been oxidized to Cr^{VI}_{aq} whereas for pyrolusite the amount is still 2%. After 80 hr. of reaction, these percentages increase to 97% for hausmannite (i.e. the reaction is essentially complete) and 13% for pyrolusite.

Basak and Malati (1977), Rophael and Boulis (1982), Malati and Rophael (1999), Chung et al. (1994) and Chung (1998) have studied Cr^{III}_{aq} oxidation by several synthetic Mn-oxides (e.g. δ-MnO_2, β-MnO_2, Mn_2O_3, Mn_3O_4). Their results show as ours do, that the rate and extent of Cr^{III}_{aq}-oxidation is mineral dependent even when the data are normalized to surface area. The earliest study (i.e. Basak and Malati, 1977) concluded that the Cr^{III}_{aq}-oxidizing ability of a Mn-oxide, for a given set of experimental conditions, is most related to the presence of Mn^{3+}. However, it is not directly proportional to the amount of $Mn^{3+}_{(s)}$, because the oxidizing ability is further enhanced if Mn^{2+} is present (as in hausmannite, Mn_3O_4) or diminished if Mn^{4+} is present. Our results generally support this conclusion, showing the following hierarchy in Cr^{III}-oxidizing ability: hausmannite > birnessite >> romanechite > manganite >> cryptomelane ≅ pyrolusite >> lithiophorite. Birnessite and romanechite, which are predominantly Mn^{4+}-oxides, with some Mn^{3+}, seem to be more powerful oxidizers than expected from their average Mn valence. A recent study of Cr^{III}-oxidation by birnessite (Kim and Moon, 1998) has shown that the degree of crystallinity should also be considered as a factor influencing the rate and extent of oxidation. Their results showed up to a 20% increase in the extent of Cr^{III}-oxidation by a less crystalline birnessite. This value of 20% was obtained in a solution that was relatively rich in Cr_{aq} compared to the present study, so it may be that 20% is a conservative estimate. The birnessite and romanechite used here were of very low crystallinity and this may account for their higher than expected position in the Cr^{III}-oxidizing ability hierarchy. Lithiophorite, which contains Mn^{3+} (~16%, Post and Appleman, 1994), is less oxidizing than expected. However, this behavior is partially explained because, as a consequence of the highly cleavable nature of our samples (and high crystallinity) the relatively insoluble (001) surface was preferentially exposed. Also, lithiophorite contains ~10 wt% Al, an element known to inhibit Cr^{III}-oxidation by promoting the uptake of Cr^{III}-solid (Fendorf et al., 1992; Bartlett and James, 1988).

9.2.1 Imaging the reactions on lithiophorite surfaces

A more extensive microscopic and spectroscopic analysis of lithiophorite was conducted because the preparation of large and flat surfaces was possible. AFM and SEM images of these surfaces reacted with either acidic or Cr^{III}_{aq} solutions show that dissolution pits (~1 to 4 nm deep)

form rapidly, but do not continue to grow beyond the size they attain after ~10 minutes of reaction (Fig. 3a inset, c, e, f, g). The $Mn2p^{3/2}$ XPS spectra of lithiophorites reacted in acidic or reductive solutions (for any length of time) support this conclusion (Fig. 4B1). This is evident by noting the decrease in intensity at 640.7 eV. This binding energy is equal to the theoretical position of the lowest binding energy Mn^{3+} multiplet predicted for a free Mn^{3+} ion (Gupta and Sen, 1974; 1975). If Mn^{2+} were present, a peak at 640.0 eV would be required and this is not observed. Once the Mn^{3+} is dissolved, the dissolution of the adjacent Mn^{4+} sites is exceedingly slow, as for other Mn^{4+}-oxides.

These observations are unlike the results of the batch reactor studies, which show a slow but steady increase in the Mn_{aq} concentration with time for both acidic and reductive dissolution for lithiophorite. We explain this difference as resulting from the fact that the AFM observations are from the (001) terraces and not from the basal edges, where acidic dissolution pitting is seen by FESEM (Fig. 3a inset). It should also be noted that the size of the AFM scans was not nearly sufficient to evaluate the spatial heterogeneity of the dissolution reaction. The density and morphology of dissolution pits as seen by FESEM varies spatially and with an unknown surface contrast mechanism. Fig. 3b shows the appearance of this contrast (i.e. shading) on a freshly cleaved surface. The contrast was most evident at low accelerating voltage and using the SE^{I} detector. Sample tilting, rotation and aging (up to six months) had no effect on this contrast. This suggests that the contrast is due to a near surface chemical or electronic variation. Lihiophorite consists of alternating octahedral layers (~0.3 nm thick) of (Li,Al)-OH "Li-hydrargillite" and Mn-O (Wadsley, 1952; Pauling and Kamb, 1982; Post and Appleman; 1994). In the Li-hydrargillite layers, ~1 octahedron in 21 is vacant. The Mn-O layers contain predominately Mn^{4+} with ~16% of these Mn^{4+} sites replaced by Mn^{3+} (Post and Appleman, 1994). Since the contrasting regions are topographically offset relative to each other it is possible that the contrast is due to the difference in the average atomic number (i.e. chemistry) between the layers.

In some locations, as dissolution is occurring on the lithiophorite surface, so is Cr^{III}-uptake (Fig. 3f,g). The bright spots seen in Figs. 3f and g are surface precipitates of a Cr^{3+}-containing phase measuring some 4 to 30 nm in height. WDS $CrK_{\alpha 1}$ analyses show the lithiophorite surfaces usually contain a higher Cr-concentration than other Mn-oxides reacted under the same conditions (Fig. 8). $Cr2p^{3/2}$ XPS spectra on lithiophorite also show an increase in

the amount of Cr^{3+} with time (Fig. 4B3). Cr^{3+} was identified based on the binding energy of 576.8 ± 0.1 eV, which is within the range (i.e. 577.0 – 576.45 eV) reported for Cr^{3+} compounds (e.g. $Cr(OH)_3 \bullet 0.4H_2O$, 576.96 eV, see Banerjee and Nesbitt, 1999). Also, the $Cr2p^{3/2}$ peak shape closely matched that of a theoretical Cr^{3+} free ion (Gupta and Sen, 1974; 1975). The contacting solution contained very little Cr^{VI}_{aq} as measured by UV-Vis (Fig. 6c). O1s XPS spectra showed a corresponding increase in the OH^- component with time. The width of the OH^- peak is greater than that of the O^{2-} peak probably because of the disorder created by vacancies in the (Li, Al)-OH layers and the multitude of possible cations to which the OH^- ligand may be bonded (e.g. Li-OH, 531.2 eV, Al-OH, 531.5 eV, Cr-OH, 531.2 eV, Mn-OH, 530.4) (Junta and Hochella, 1994; Moulder et al., 1995) (Fig. 4B2). Although not definitive, this increase probably results from the formation of a chromium hydroxyhydrate, as was observed to form on manganite (Weaver and Hochella, in review) and birnessite (Fendorf et al., 1992; Manceau and Charlet, 1992) under similar conditions.

The fact that Cr is typically detected in greater amounts by bulk techniques, such as WDS and EDS, even in locations where surface precipitates are not observed, suggests that absorption is also a Cr-uptake mechanism. This observation combined with the additional WDS observation of an increase and subsequent decrease in Cr on some samples suggests that Cr_{aq} infiltration and Cr^{III}-absorption has occurred (Fig. 8). Cr-absorption is certainly a possibility, considering the layer structure and pitting observed along the basal edges (Fig. 5a). Direct evidence for Cr-absorption was provided by XPS observations obtained on an interior lithiophorite surface (Fig. 4B3). FESEM observations along the perimeter of this interior surface did not show precipitates along the exterior surface, but did show in some locations a patchy or sinuous distribution of a solid phase, presumably Cr-containing (Fig. 3d).

Cr-uptake by lithiophorite may be facilitated because $Cr(OH)_2$ and the (Li-Al)-OH layer are isostructural (Pauling and Kamb, 1982). Furthermore, Bartlett and James (1988) have demonstrated an affinity or association between Cr^{3+} and Al^{3+}, which they attribute to their similar ionic radii (e.g. Cr-0.064 vs. Al-0.067 nm). Fendorf et al. (1993) have suggested that Cr^{3+} may substitute for Al^{3+} in $Al(OH)_3$. In light of these similar crystal-chemical properties of Cr^{3+} and Al^{3+} and the presence of vacancies in the hydrargillite layers, Cr uptake has many reasons to be more likely on lithiophorite than on other Mn-oxides. Minor to trace amounts of aluminum were also present in other Mn-oxides (e.g. romanechite, cryptomelane, manganite)

(Table 2). The presence of Al or other substituted metals will have a considerable effect on the electronic properties of the surface, such as quenching surface states that would otherwise participate in the oxidation of Cr^{III}_{aq}. Heterogeneous distribution of Al may also account for the spatial heterogeneity of Cr-uptake.

9.2.2 Reaction stoichiometry

As the increase in the concentrations of Mn_{aq} and Cr^{VI}_{aq} are directly coupled, a ratio of their concentrations (i.e. $[Mn]_{aq}$: $[Cr^{VI}]_{aq}$) should approximate the stoichiometry of the overall reaction. $[Mn]_{aq}$: $[Cr^{VI}]_{aq}$ ratios were calculated from the raw data and compared against the ratio expected from the stoichiometry of the reactions proposed in Table 2. A plot of these Mn_{aq} : Cr^{VI}_{aq} ratios versus the type of Mn-oxide shows, as expected, that higher ratios are generally exhibited by the Mn-oxides of lower average Mn valence (Fig. 9). The closed symbols show the ratios as determined for two cases: 1) considering only the reductively dissolved manganese $[Mn]^R$ and, 2) with the $[Mn]^A$ component included (i.e. $[Mn]^{R+A}$). These values tend to be very similar for the acid insoluble Mn^{4+}-oxides, but diverge as the average Mn valence (and solubility) decreases. In the case of hausmannite, there exists a broad range in predicted values because it is unclear how the highly soluble Mn^{2+} ions contribute to the $[Mn]^{R+A}$ measurement. This uncertainty exists because the Mn^{2+} ions cannot be further reduced, but do readily dissolve in acid. The large open symbols show the expected Mn_{aq} : Cr^{VI} ratios (Table 2). In general there is good agreement between the measured and predicted ratios for all of the minerals except hausmannite.

9.2.3 Re-exposure of Cr-reacted Mn-oxide powder to fresh Cr^{III}_{aq}

The experiments in which the Cr^{III}_{aq}-reacted Mn-oxide powder was re-reacted in a fresh 10^{-4} M Cr^{III}_{aq} solution showed the same initial period of rapid Cr^{III}-oxidation as was observed in the original experiments. Interpreting this unexpected behavior was initially difficult because it was: 1) our observation that changing solution conditions (e.g. $[Mn]_{aq}$, $[Cr^{VI}_{aq}]/[Cr^{III}]_{aq}$) did not limit the extent of Cr^{III}-oxidation (for example, note that the Cr^{III}-oxidation by birnessite and

hausmannite (Fig. 6a,d,e) are very rapid, despite the relatively high $[Mn]_{aq}$ and $[Cr^{VI}_{aq}]/[Cr^{III}]_{aq}$ ratio) and 2) our premise that a permanent decrease in the Cr^{III}-oxidizing power of the Mn-oxide surface (or, alternatively stated, a permanent change in the surface electronic structure) resulted from the Cr-uptake and reductive dissolution processes. However, since our experimental procedure involved the drying and storage (30 days) of the reacted Mn-oxide powder, it was not possible to exclude the possibility that the Mn-oxide surface had been returned to a highly oxidizing state. An additional Cr^{III}-oxidation experiment performed in which the re-reacted Mn-oxide powder was not dried could show if the Cr^{III}-oxidizing ability of the surface had in fact regenerated during the drying or storage steps. If an initially rapid period of Cr^{III}-oxidation is not observed then it would be highly likely that surface alteration did occur as a result of drying and storage. It is possible that the results of this proposed experiment could still be ambiguous because exposing the reacted Mn-oxide suspension to a fresh solution (even of the same pH, ionic strength and $[Cr]^{T}_{aq}$) could change the charge of the Mn-oxide surface or could displace adsorbed ions from potentially reactive sites. Alternatively, XPS could be used to determine if there is a progressive change in the surface with time.

9.2.4 Cr-uptake

For all of the Mn-oxides used in this study, except those with tunnel structures (romanechite and cryptomelane), Cr-uptake is initially rapid and slows with reaction time. This behavior is best demonstrated in the aqueous concentration data (Fig. 6a-h), though spectroscopic measurements of Cr concentrations (e.g. XPS and WDS) also support this general observation (Fig. 4, 8). Hausmannite and birnessite show this initial rapid Cr-uptake, however during the later stage of their reactions, after $\geq$ 50% of the $[Cr]^{T}_{aq}$ has been oxidized to Cr^{VI}_{aq}, there is a period of relatively slow Cr release (Fig. 6a,d,e). This release is also qualitatively evident in the WDS data (Fig. 8), which shows a decrease in Cr after ~1 hr. for birnessite and after ~4 hr. for hausmannite. The times at which the Cr-release is observed for birnessite and hausmannite by ICP and WDS correspond satisfactorily given that fewer samples were analyzed by WDS and the [Cr] measurement is made over a small (~5 μm^2) area where the Cr distribution may not be uniform. As previously mentioned, there is a subsequent increase in $[Cr]^{T}_{aq}$ which

correlates with a slow increase in $[Cr^{VI}]_{aq}$. This is good evidence that the oxidizing ability of the surface has changed or more likely, that the form of Cr undergoing oxidation and subsequent release was not the same throughout the reaction for birnessite and hausmannite. For birnessite, the relatively high rate of initial Cr-uptake may be attributable to Cr^{III}-adsorption to the negatively charged surface (PZC ~2) and also due to absorption into the interlayer or at vacancy sites, as was seen for lithiophorite. Manceau and Charlet (1992) report a similar observation of Cr-desorption by birnessite from an in-situ XAS study. They describe the process as a double solid-state diffusion, involving the inner sphere adsorption of Cr^{III}_{aq}, and subsequent desorption. For hausmannite (PZC <5), the high rate of Cr-uptake is attributable to the higher pH (5.2) of the solution which likely catalyzed surface nucleation of $Cr(OH)_3 \bullet nH_2O$, although Cr-adsorption is also possible. The WDS analyses of the reacted powders shows that hausmannite and birnessite exhibited the greatest amount of initial Cr-uptake. It is appropriate to mention here that Cr-uptake control experiments, performed in the absence of Mn-oxide at pH 3, 4, 5 ± 0.2, 10^{-4} M $Cr^{III}OH^{2+}_{aq}$ did not show any decrease in $[Cr]^{T}_{aq}$ during a 4 day period. Since all of our experiments were conducted under aqueous conditions that were less saturated with respect to $Cr(OH)_{3(s)}$ than these control experiments, it is certain that no significant portion of the observed decreases in $[Cr]^{T}_{aq}$ was due to homogenous $Cr(OH)_{3(s)}$ precipitation (Baes and Mesmer, 1976).

XPS $Mn2p^{3/2}$ spectra from pyrolusite ground and pressed in air, show the solid to be initially non-stoichiometric (Fig. 4c1). This is a common quality for pyrolusite, but has not been previously observed by XPS (Shuey, 1975). Approximately 90% of the spectra is attributable to Mn^{4+}, based on values of the multiplet structure for the Mn^{4+} free ion modified after Gupta and Sen (1974; 1975). The remaining 10% is probably due to Mn^{3+} though the presence of some Mn^{2+} cannot be dismissed because spectral data fitting is complicated for species at low concentrations and exhibiting a complex multiplet structure. While under UHV, the pressed β-MnO_2 surface was scraped with the manipulator and a second spectrum was obtained. The spectrum of the scraped surface showed ~6% decrease in the amount of reduced Mn species (Fig. 4c1). It is likely that the initially rapid acidic dissolution of pyrolusite was at least partially due to the higher solubility of this reduced Mn component. $Mn2p^{3/2}$ spectra of pyrolusites reacted in acidic or reductive dissolution experiments for any length of time appeared very similar to the UHV scraped surface. The Mn3s spectra showed a constant multiplet splitting of 4.7 ± 0.1 eV. This is slightly greater than reported multiplet splitting values of 4.5 eV for Mn^{4+}. This also

shows that reduced Mn is present, but indicates that the Mn3s peak is not as sensitive as the $Mn2p^{3/2}$ peak. However, the Mn3s peak is generally of greater utility than the $Mn2p^{3/2}$ for determining the bulk Mn valence (Evans and Raftery, 1982; Junta and Hochella, 1994). A recent study by Fujiwara et al. (1995) has shown that Mn3s spectra are very diagnostic for the valences and structures of various Mn-oxy,nitro,chloro complexes. FESEM images of pyrolusite reacted in acidic or reductive solutions did not show any definitive evidence for dissolution or Cr-uptake (Fig. 2). However, $Cr2p^{3/2}$ XPS spectra showed that the chromium concentration continued to increase after 10 min of reaction (Fig. 4c3). The surface Cr is predominately Cr^{III} , but some Cr^{VI} is also present. O1s spectra of Cr^{III}-reacted surfaces show a slight progressive increase in the OH^- and H_2O signals with reaction time. This may suggest that the surface sequestered Cr-phase, contains or is coordinated with water or hydroxyl (e.g. $Cr(OH)_3 \bullet nH_2O$).

Studies of Cr^{III}-adsorption to hydrous Fe-oxide (Leckie et al., 1984), Al-oxide (Wehrli et al., 1990) and previous Cr^{III} oxidation studies by Mn-oxides (Eary and Rai, 1987; Johnson and Xyla, 1991) show that Cr^{III}-absorption can occur against a strong positive surface charge. This must have been the case in the current study for Cr^{III}-adsorption to pyrolusite (PZC 7.3) and manganite (PZC 5.5) given the solution pH of 4.4. Kinetic studies of Cr^{III}_{aq} adsorption to Al_2O_3 under aqueous conditions comparable to ours (e.g. $\leq 5 \bullet 10^{-5}$ M Cr^{III}_{aq}, pH 3.1 - 4.4) observed as we did, an initially rapid adsorption step followed by a slower, pH dependent step (Wehrli et al. 1990). This observation was interpreted on the basis of the water exchange rates for the two Cr^{III}_{aq} species, Cr^{3+}_{aq} ($2.4 \bullet 10^{-6}$ s^{-1}) and $CrOH^{2+}_{aq}$ ($1.8 \bullet 10^{-4}$ s^{-1}) present under these conditions, with the higher exchange rate of $CrOH^{2+}_{aq}$, suggesting more rapid surface complex formation.

The observation of a fast then slow Cr^{III}-oxidation period on all of the Mn-oxides shows that the oxidation of Cr^{III} to Cr^{VI} by single electron transfers (i.e. $Cr^{III} \rightarrow Cr^{IV} \rightarrow Cr^{V} \rightarrow Cr^{VI}$) into the Mn-oxide becomes inhibited with time. Our microscopic and spectroscopic observations suggest that the inhibition may be due to minor amounts of Cr-uptake, Mn-reduction or dissolution of active sites. Microscopic observations for lithiophorite show that reactive regions (i.e. large 'sites') initially present are rapidly consumed. As previously stated, most of the past studies which observed the same type of kinetic behavior (but lacked microscopic and spectroscopic observations) also concluded that some type of surface alteration must be responsible. Studies with supporting microscopic and spectroscopic observations also share the same interpretation. For example, Banerjee and Nesbitt (1999) have shown by XPS that Cr^{IV} and

Cr^{V} intermediates are present on birnessite surfaces after reaction with Cr^{III}_{aq}. However, they also admit that the similarity in binding energy between Cr^{III} and Cr^{IV}, and between Cr^{V} and Cr^{VI} precludes their separate identification. Assuming that Cr^{IV} and Cr^{V} have been correctly identified, their presence as a stable species supports the above suggestion that certain sites or regions on the Mn-oxide surface do not readily accept electrons and therefore cannot fully oxidize Cr^{III} to Cr^{VI}. This would imply that the rate and extent of Cr^{III}_{aq} oxidation depends strongly on the initial and changing electronic properties of the surface. As the Mn-oxides used in this study demonstrate a range in electrical behavior from insulating to highly semiconducting, we concluded that other electrical properties (e.g. Fermi level, band gap) known to strongly influence redox reactions occurring at the electrolyte/semiconductor interface would also vary among the Mn-oxides. On the basis of measured and calculated values for band gap and Fermi level (see below), we evaluated the Cr^{III}-oxidizing ability of the Mn-oxides by the fluctuating energy level model.

9.3 Fluctuating energy level model for predicting redox reactions at the semiconductor/electrolyte interface

9.3.1 Definitions and concepts from band theory

In the quantum mechanical description of a solid, electrons are distributed over a range of energies from the highest energy core levels, to the lowest energy valence levels, to excited conduction band levels. The fundamental energy width between discrete energy levels (i.e. quanta or states) has the magnitude kT, where k is Boltzman's constant ($1.38E^{-23}$ J/K) and T is the temperature (K). Converting kT to the more familiar absolute energy units in electron-volts (eV), where 1 eV = $1.602 \bullet 10^{-19}$ J and considering a solid at room temperature (298.15 K), each state would have an energy width of ~0.0257 eV (i.e. ~40 states/eV). States extend continuously from the vacuum level (i.e. E = 0 eV) to the highest energy core level and may be occupied by one or more electrons, or may be empty. The fact that a large population of electrons in a solid may occupy the same energy state does not violate the Pauli Principle because the electrons are delocalized from their parent orbital (and nucleus). Electron delocalization (i.e. sharing between nuclei) gives rise to an uneven distribution of electrons, or "density of states" (DOS), over all

available energies for that solid. A group of adjacent states, possessing a high electron density is referred to as a 'band' (although a group of adjacent empty states may also be referred to as a band.). The band resulting from electrons that reside in filled bonding orbitals is known as the 'valence band'. The band resulting from vacant antibonding orbitals is known as the 'conduction band'. In a semiconductor (or insulator), the valence band and the conduction band are generally separated by a range of empty states (i.e. energies) known as the band gap (E_g). Since electrical conduction in a material is accomplished by exciting a valence-band electron into a delocalized conduction-band state, the size of the band gap relates directly to the material's ability to conduct electricity. The energy level in a solid where it is equally probable to find an occupied or empty state is known as the Fermi energy level (E_f). Stated in another way, the number of occupied and empty states on either side of the Fermi level is the same. In a semiconductor, the Fermi level is always located within the band gap, but its position may vary from top to bottom depending on the type of free charge carriers.

Semiconductors are classified as intrinsic or extrinsic based on the type of free charge carriers responsible for electron conduction. Intrinsic semiconductors transfer charge by the motion of electrons and holes, which are present in nearly equal quantities. Extrinsic semiconductors transfer charge by way of defects or dopants (i.e. trace-level impurities), which may act as electron acceptors or electron donors. Intrinsic semiconduction is therefore rare in minerals because trace levels of impurities and defects are common (however, pyrolusite is intrinsic). Semiconductors are further subdivided into 'p' and 'n' types, where n-type denotes that the dopants (or defects) are electron donors, and p-type denotes that the dopants (or defects) are electron acceptors. Since the dopants will effect the distribution of electrons, the Fermi level (E_f) will be shifted. In an extrinsic n-type semiconductor, the E_f is typically shifted to near the bottom of the conduction band by the electron-rich dopants (i.e. donor states). In an extrinsic p-type semiconductor, the E_f is typically shifted to near the top of the valence band by the electron-deficient dopants (i.e. acceptor states). In an intrinsic semiconductor, the E_f is located approximately halfway between the base of the conduction band and the top of the valence band.

9.3.2 Interpretation of experimental results

For the most part, there was a correlation showing that the Mn-oxides of lower average valence are more effective Cr^{III}-oxidizers. With a decrease in valence, there is also an accompanying shift in Mn-O bonding character and electrical properties towards more ionic and more insulating, respectively (Fig. 10). This shift towards more insulating behavior was apparent from charging observed during XPS and FESEM analysis and also from macroscopic resistance measurements on single crystal samples. Based on these observations, we inferred the following order of conductivity for the three simple Mn-oxides: hausmannite < manganite < pyrolusite. This order is also supported by band gap (E_g) values cited (Shuey, 1975; Samsonov, 1982) or calculated from the refractive indices of these minerals (Wemple and Didomenico, 1969).

Given that the Cr^{III}_{aq} - Mn-oxide interaction is electrochemical in nature, it would be expected that the electrical properties of the Mn-oxide and the $Cr^{III}_{aq}/Cr^{VI}_{aq}$ redox couple would strongly influence the rate and extent of the reaction. This premise can be aptly evaluated using the fluctuating energy level model of Marcus (1965) and Gerischer (1978) (also see Morrison, 1980, and Nozik and Memming, 1996, for substantial development of this theory). In essence, this model determines if an electrochemical (i.e. redox) reaction is energetically favorable by comparing the Fermi energy level of the semiconducting solid phase with that of the redox potential (E^o) of the aqueous redox couple. By this comparison, it may be demonstrated that the rate and extent of the reaction is proportional to their difference in energy. If the energy of the redox couple is equal to or greater than the Fermi level of the semiconductor, then electrons are spontaneously transferred into the semiconductor. If the reverse is true, then electrons are transferred from the solid into the aqueous redox couple. If the two energy levels are approximately the same or slightly different, then it may be possible for electron transfer to occur in either direction (i.e. even against a bulk potential energy gradient). This is possible because semiconductors commonly contain a small population of electron donor and electron acceptor energy levels (i.e. states, bands) on either side of the Fermi level. These donor or acceptor states are typically due to dopants (i.e. impurities), defects or surface states and may provide an energetically favorable pathway by which electron transfer may be accomplished (see Fig. 11) or

may provide reactants with the additional energy they require to exceed an activation energy and form products.

Surface states, also referred to as "dangling bonds", are energy levels that arise at a surface due to the under-coordinated nature of the surface atoms (i.e. a break in the bulk symmetry). Surface states, though difficult to characterize, have been shown in many cases to have a significant effect on the electronic properties at solid-solid and solid-electrolyte interfaces (Nozik and Memming, 1996; Bard and Faulkner, 2001). On most surfaces, impurities, defects and surface states are likely to be heterogeneously distributed and in relatively limited supply. Therefore, if the energy states arising from defects, impurities or surface states were responsible for promoting an otherwise thermodynamically unfavorable reaction (as is arguably the case for Cr^{III}-oxidation by Mn-oxides, see Chung, 1998) then, the reaction would show a rapid decrease in rate as these reactive 'states' were quenched by electron transfer from an adsorbing species or destroyed by dissolution. External energy inputs from heat and light may also affect a reacting system by creating, destroying or shifting the energy levels within the solid (e.g. consider photoconductivity, thermoluminescence and fluorescence). Through these many caveats, it is important to recognize that as the name of the model implies, the energy levels within the solid and aqueous redox couple are likely fluctuating as the reaction progresses and are also fluctuating in space as the width of the electrical double layer is changed or the surface undergoes local chemical, structural and topographic changes.

The remaining discussion is devoted towards demonstrating the interpretive power of the fluctuating energy level model to our observations on hausmannite (Mn_3O_4) and pyrolusite (MnO_2). Only hausmannite and pyrolusite are discussed because their range in reactivities and electrical properties closely proxies for that of all seven of the Mn-oxides studied. The reader should be informed that in some respects this discussion must be considered speculative since all of the electrical properties of the Mn-oxides (e.g. band gap, Fermi level) were calculated rather than directly measured. However, as was previously mentioned, because these electrical properties may vary appreciably with the extent of reaction, and also from sample to sample and even from location to location on the same sample, it may not be wise to exclusively use bulk, direct measurements of these properties anyways.

The first step in preparing the band energy diagram for our system is to calculate the Fermi levels for the Mn-oxides. The Fermi level of a semiconductor at its point of zero charge

(PZC) may be approximated using the average work function (ϕ_{ave}) (Fig. 10). The average work function for MnO_2 and Mn_3O_4 can be calculated from the work functions of the constituent species, that is, ϕ_{Mn} = 4.0 eV and ϕ_{O_2} = -7.28 eV (Morrison, 1980; Butler and Ginley, 1978). Thus,

$E_{f,}\ MnO_2 = (\phi Mn + \phi O_2)/2 \qquad = -5.64$ eV

$E_{f,.}\ Mn_3O_4 = (3\phi Mn + 2\phi O_2)/5 \qquad = -5.31$ eV

Since the pH in our experiments was not equal to the PZC, the Fermi levels must be corrected. The correction factor is –0.059 eV for each pH unit the reacting solution is less than the materials PZC. Thus,

$$E_f \text{ at } pH_{exp} = E_f \text{ at PZC} - 0.059\ (PZC - pH_{exp}) \qquad (1)$$

By substitution,

$E_{f,}\ MnO_2$ at pH 4.4 $= -5.64$ eV $- 0.059\ (7.3 - 4.4) = -5.81$ eV

$E_{f,.}\ Mn_3O_4$ at pH 5.2 $= -5.31$ eV $- 0.059\ (5.0 - 5.2) = -5.30$ eV

The band gap (E_g) of an oxide may be calculated from its index of refraction (n) (Wemple and Didomenico, 1969).

$$E_g = 15/(n^2-1) \qquad (2)$$

As hausmannite is optically anisotropic, an upper limit for E_g = 4.14 eV is obtained from n_ε = 2.15. The E_g for pyrolusite is expected to be much lower because of its observed conductivity and opaque nature. Since Eqn. 2 does not apply for opaque substances, E_g = 0.25 eV for pyrolusite was obtained from Shuey (1975). Band gaps for pyrolusite as large as 1.3 eV have been reported by Samsonov (1982). This range in reported band gaps likely results from sample heterogeneities including impurities, grain boundaries, reduced manganese species and crystallographic anisotropies. Further, pyrolusite is a rare example of an intrinsic

semiconducting mineral (Shuey, 1975). Finally, although it is not known if our hausmannite sample is intrinsic or extrinsic, and p- or n-type, it will be illustrative to consider hausmannite as extrinsic and n-type.

Given these semiconducting properties (e.g. E_g ,E_f), energy band diagrams are plotted for hausmannite and pyrolusite (Fig. 12). Note that for the intrinsic pyrolusite, the E_f is at mid-gap, whereas for the extrinsic hausmannite, its E_f is shifted towards the conduction band.

The next step is to plot the energy of the Cr^{III}/Cr^{VI} redox couple on the band diagram. The redox potential (E^o) in volts, for the Cr^{III}/Cr^{VI} reaction (Eqn. 3) at any given pH and $[Cr^{VI}]/[Cr^{III}]$ ratio can be calculated from Eqn. 4 (Pourbaix, 1974).

$$CrOH^{2+}_{aq} + 3H_2O = HCrO_4^-{}_{aq} + 6H^+ + 3e^- \qquad E^o = 1.275 \text{ V} \qquad (3)$$

$$E^o = 1.275 - 0.1182\ pH + 0.0197 \log [Cr^{VI}]/[Cr^{III}] \qquad (4)$$

The E^o value of 1.275 V given in Eqn. 3 applies only to the experimental conditions: pH = 0 and $\{[Cr^{VI}]/[Cr^{III}]\} = 1$. To evaluate the maximum range of values that E^o may encompass over our observed experimental conditions, we consider $[Cr^{VI}]/[Cr^{III}]$ = 1% (onset of reaction) and = 99% (complete reaction), at pH 4.4. Thus,

$$\left.\begin{aligned} E^o_{\text{(onset)}} &= 1.275 - 0.1182\ (4.4) + 0.0197 \log 0.01 = 0.72 \text{ V} \\ E^o_{\text{(complete)}} &= 1.275 - 0.1182\ (4.4) + 0.0197 \log 99 = 0.79 \text{ V} \end{aligned}\right\} \cong -0.75 \text{ V}$$

Since the redox potential is measured on a scale relative to the standard hydrogen electrode (SHE), it must be converted to the same energy scale used to denote the energy levels in the solid before a comparison between the two can be made. The energy of a solid is measured with reference to the energy of an electron in vacuum (i.e. E^{e-}_{vac} = 0 eV). On the SHE scale, this reference energy equals –4.5 eV (Bard and Faulkner, 2001). Thus,

$$\left.\begin{aligned} E^{e-}_{vac} &= (-4.5 - E_o) \\ E^{e-}_{vac}\ \text{(onset)} &= (-4.5 - 0.72) = -5.22 \text{ eV} \\ E^{e-}_{vac}\ \text{(complete)} &= (-4.5 - 0.79) = -5.29 \text{ eV} \end{aligned}\right\} \cong -5.25 \pm 0.04$$

As these values are approximately the same, this shows that there is very little 'fluctuation' in the energy level of the redox couple over the course of the reaction. This suggests that the observed Cr^{III}-oxidation rate behavior (i.e. initially rapid, then considerably slower) is probably not due to a change the $[Cr^{VI}]/[Cr^{III}]$ ratio, but is likely due to a change in the availability of electron accepting states in the Mn-oxide.

As suggested by the relatively high coefficient (i.e. –0.1182) on the pH term in Eqn. 4, the Cr^{III}-oxidation by Mn-oxide should show pH dependence. From Eqn. 4, as the pH increases, the energy of the Cr^{III}/Cr^{VI} couple shifts by –0.1182 eV/ pH unit. As previously stated (Eqn. 2), increasing pH would shift the Fermi level of the semiconductor in the opposite direction by +0.059 eV/ pH unit. This relatively opposite energy shift predicts that Cr^{III}-oxidation should be more energetically favorable at lower pH. Most experimental observations are in agreement with this, showing that Cr^{III}-oxidation is more rapid and extensive at lower pH (Eary and Rai, 1987; Fendorf and Zasoski, 1992; Kim and Moon, 1998, Chung, 1998; Weaver and Hochella, in review). However, one of these studies (Chung, 1998) showed a slightly opposite effect (for pyrolusite) and the study of Johnson and Xyla (1991) who only studied initial rate behavior (i.e. < 5 min), observed that pH had no effect.

An additional point to consider is the fact that the redox potential determined is for the combined transfer of three electrons. Since it is likely that electron transfer from an adsorbed Cr^{III} to the Mn-oxide proceeds by single electron transfers, rather than all three electrons at once, it would probably be more accurate to use the redox potentials for each of the intermediate reactions (i.e. Cr^{III}/Cr^{IV}, Cr^{IV}/Cr^{V}, Cr^{V}/Cr^{VI}). However, thermodynamic data for the Cr^{IV}_{aq} and Cr^{V}_{aq} species are not available because they are too unstable. If each of these redox couples is assumed to have the magnitude of one third of the total potential (i.e. ~0.75 V/3 = 0.25 V) then the resulting redox potential for each single electron transfer subreaction is –4.75 eV.

Now, plotting the energy level of the redox couple (–5.25 eV) on the band diagram (Fig. 12) shows that the energy of the redox couple is greater than the Fermi levels of both hausmannite and pyrolusite. For pyrolusite, the energy of the Cr^{III}/Cr^{VI} couple lies within the conduction band. For hausmannite, the energy of the Cr^{III}/Cr^{VI} couple lies within the band gap. This would tend to suggest that Cr^{III}-oxidation by pyrolusite should be much more extensive than was observed because the conduction band contains a high density of empty states, where electrons

may be transferred. This example also shows a greater energy difference between that of the Cr^{III}/Cr^{VI} couple and E_f for pyrolusite than for hausmannite. In the absence of other electronic information about the solids, this would tend to suggest that pyrolusite should display a more rapid and extensive oxidation of Cr^{III} than hausmannite. However we observed the opposite in our experiments.

This discrepancy may be explained if it is assumed that the Cr^{III}-oxidation rate behavior (i.e. very rapid then slow) results from the presence of a finite supply of states capable of accepting electrons from an adsorbed Cr^{III}. States of this energy may be *initially* present due to surface states, defects or impurities, but may not be subsequently created unless this is accomplished perhaps by dissolution. Thus, the Cr^{III}-oxidation rate should show a very rapid decrease as these initially present electron acceptor states are consumed (Fig. 11). This may explain why all of the Mn-oxides in this study and other studies show an initially rapid Cr^{III}-oxidation rate, and why the Mn-oxides containing a more soluble Mn^{2+} or Mn^{3+} component (e.g. hausmannite and birnessite) exhibit a more sustained Cr^{III}-oxidation reaction. If drying of the Mn-oxide can also regenerate surface states, then this may explain why a period of initially rapid Cr^{III}-oxidation was also observed on the Mn-oxide that was re-reacted in a fresh Cr^{III} solution.

Although we could not test the predictive capability of the fluctuating energy level model using measured values for E_f and E_g, this discussion has shown that the redox potential of the Cr^{III}/Cr^{VI} couple is generally greater than the Fermi levels of the Mn-oxides (perhaps by as much as 0.5 eV for pyrolusite). This suggests that in terms of the bulk the Cr^{III}-oxidation reaction is energetically favorable with bulk Mn-oxide. Since this reaction is known to occur directly at the Mn-oxide future investigations should give more attention to the measurement of surface electronic properties.

10. SUMMARY AND CONCLUSIONS

1. The seven Mn-oxides studied (hausmannite, manganite, lithiophorite, romanechite, cryptomelane, birnessite, pyrolusite) exhibited a wide range in their abilities to take up and oxidize chromium. All of the Mn-oxides exhibited an initial rapid period of Cr^{III}-oxidation, as is commonly observed in studies of this type. The longevity of this initial period is interpreted to depend on the initial number of electron accepting surface states, and also on the ability of the

Mn-oxide surface to create new such reactive states. This latter ability is thought to be most related to the solubility of the Mn-oxide.

2. The fact that dried samples of the Cr-reacted Mn-oxide powder, when re-reacted in a fresh Cr^{III}_{aq} solution, showed an initial period of rapid Cr^{III}-oxidation suggests that drying may restore the oxidizing ability of the Mn-oxide surface. Previous studies (Bartlett and James, 1988) have shown that the Cr^{III}-oxidizing ability of Mn-oxides may be increased or decreased after storage or varying treatments. At present it can only be speculated that drying may cause the number of electron accepting surface states to increase.

3. Cr^{III} was the dominant oxidation state adsorbed to all Mn-oxides, although pyrolusite did contain some Cr^{VI}. In addition to Cr-adsorption, Cr-absorption occurred for both of the layer Mn-oxides (birnessite and lithiophorite). This was conclusively demonstrated by XPS spectra and high-resolution FESEM images obtained from reacted lithiophorite surfaces and indirectly demonstrated from desorption trends in batch reactor experiments.

4. High-resolution, FESEM imaging of Cr^{III}-reacted Mn-oxides demonstrated that contrast mechanisms and enhanced surface sensitivity (<4 nm in some cases) resulting from low accelerating voltage operation (e.g. <5 keV) can provide important information as to the spatial distribution of chemical and electronic heterogeneities.

5. There is a correlation between the solubility of a Mn-oxide and its average Mn-valence. This correlation can be explained in terms of the susceptibility of the Mn-O bond to be polarized (and subsequently broken) by an adsorbed charged species. Such susceptibility can be explained adequately by crystal-chemical properties such as coordination, charge and bond length. Bond polarization by adsorbing species can explain proton promoted and reductive dissolution. However, in the case of reductive dissolution, additional consideration must be given to the interaction between the electronic energy levels of the mineral surface, relative to those of the aqueous redox couple (e.g. Cr^{III}/Cr^{VI}).

6. The fluctuating energy level model (see Morrison, 1980; Nozik and Memming, 1996) provides a detailed description of the relevant chemical, physical and electronic processes occurring between a semiconducting Mn-oxide surface and the $Cr^{III}_{aq}/Cr^{VI}_{aq}$ redox couple. This is accomplished by comparing the energy level(s) of the solid-state reactants with those of the aqueous reactants. In principle, this model can be freely applied by environmental scientists to understand complex geochemical systems and fundamental reaction mechanisms. Although difficult to verify experimentally, this model also addresses the influences of various types of surface heterogeneities.

7. Chemical shifts observed in $Mn2p^{3/2}$ XPS spectra of reacted samples versus fresh samples were generally subtle, but in several cases well above the detection limit. Acid or Cr^{III}-reacted lithiophorite, hausmannite and pyrolusite surfaces showed an increase in the surface Mn oxidation state. This was interpreted to result from leaching of the more soluble reduced Mn components (e.g. Mn^{2+} and Mn^{3+}). However, we also suspect that the thickness of an altered surface layer is less than the surface sensitivity of an XPS instrument operating with $AlK_{\alpha 1}$ X-rays (i.e. 1486.6 eV). Furthermore, we cannot dismiss the possibility that the oxidation states of the surfaces were altered since it was necessary to allow the samples to dry in air before they could be analyzed. Future experiments will utilize spectroscopic and microscopic techniques offering spatial resolution and higher surface sensitivity (e.g. synchrotron scanning XPS microscopy, Auger) and/or in situ surface-chemical analysis (e.g. Raman).

8. Ongoing research should be focused on obtaining in situ and spatially resolved measurements of the changing semiconducting properties (e.g. E_f, E_g) of the Mn-oxide surface during alternating drying and Cr^{III}_{aq} exposures. A fundamental understanding of these effects has obvious applicability since drying and wetting cycles are a common environmental process and also because, in this system these processes are linked to restoring or impairing a Mn-oxide's ability to oxidize Cr^{III} to the more mobile and toxic Cr^{VI}_{aq} form.

11. REFERENCES

Amacher M. C. and Baker D. A. (1982) Redox reactions involving chromium, plutonium and manganese in soils. Institute for Research on Land and Water Resources, Penn. State Univ.

Baes C. F. and Mesmer R. E. (1976) *The hydrolysis of cations*. Wiley.

Banerjee D. and Nesbitt H. W. (1999) Oxidation of aqueous Cr(III) at birnessite surfaces: constraints on reaction mechanism. *Geochim. Cosmochim. Acta* **63**, 1671-1687.

Bard A. J. and Faulkner L. R. (2001) *Electrochemical methods: fundamentals and applications*. Wiley.

Barr T. (1994) *Modern ESCA, The principles and practice of X-ray photoelectron spectroscopy*. CRC Press.

Bartlett R. J. and James B. R. (1988) Mobility and bioavailability of chromium in soils. In *Chromium in the Natural and Human Environments*, Vol. 20 (eds. J. O. Nriagu and E. Nieboer), p. 571

Basak B. and Malati M. A. (1977) Characterization of manganese dioxides. IV. The oxidation of chromium(III) ions by manganese dioxides. *J. Inorg. Nucl. Chem.* **39**, 1081-1084.

Bickmore B. R., Bosbach D., Hochella M. F. J., Charlet L., and Rufe E. (2001) In situ atomic force microscopy study of hectorite and nontronite dissolution: Implications for phyllosilicate edge surface structures and dissolution mechanisms. *Amer. Mineral.* **86**, 411-423.

Bidoglio G. G., P. N.; O'Gorman, M.; Roberts, K. J. (1993) X-ray absorption spectroscopy investigation of surface redox transformations of thallium and chromium on colloidal mineral oxides. *Geochim. Cosmochim. Acta* **57**, 2389-2394.

Boucher B., Buhl R., and Perrin M. (1971) Magnetic properties and structure of manganese oxide. *J. Phys. Chem. Solids* **32**, 2429-37.

Burns R. G. (1970) *Mineralogical applications of crystal field theory*. University Press.

Butler M. A. and Ginley D. S. (1978) Prediction of flatband potentials at semiconductor-electrolyte interfaces from atomic electronegativities. *J. Electrochem. Soc.* **125**, 228-32.

Chartier A., D'Arco P., Dovesi R., and Saunders V. R. (1999) An *ab initio* Hartree-Fock investigation of the structural, electronic and magnetic properties of Mn_3O_4- Hausmannite. *Phys. Rev. B.* **B**, 14042-14048.

Chung J.-B. (1998) Chromium speciation in Cr(III) oxidation by Mn-oxides: relation to the oxidation mechanism. *Han'guk Nonghwa Hakhoechi.* **41**, 89-94.

Chung J.-B., Zasoski R. J., and Lim S.-U. (1994) Kinetics of chromium(III) oxidation by various manganese oxides. *Han'guk Nonghwa Hakhoechi.* **37**, 414-20.

Crerar D. A., Cormick R. K., and Barnes H. L. (1980) Geochemistry of manganese: An overview. In *Geology and Geochemistry of Manganese. Mineralogy, Geochemistry, Methods.*, Vol. 1 (eds. I. M. Varentsov and G. Grasselly). 293-334.

Dachs H. (1963) Neutronen- und rontgenuntersuchungen am manganit, MnOOH. *Zeits. Kristallographie I.* **118**, 303-326.

Eary L. E. and Rai D. (1987) Kinetics of chromium (III) oxidation to chromium (VI) by reaction with manganese oxide. *Environ. Sci. Technol.* **26**, 79-85.

Evans S. and Raftery E. (1982) Determination of the oxidation state of manganese in lepidolite by x-ray photoelectron spectroscopy. *Clay Mineral.* **17**, 477-81.

Fendorf S. E., Fendorf M., Sparks D. L., and Gronsky R. (1992) Inhibitory mechanisms of chromium(III) oxidation by δ-manganese dioxide. *J. Coll. Interface Sci.*, **153**, 37-54.

Fendorf S. E. and Zasoski R. J. (1992) Chromium(III) oxidation by δ-manganese oxide (MnO_2). 1. Characterization. *Environ. Sci. Technol.* **26**, 79-85.

Fendorf S. E., Zasoski R. J., and Burau R. G. (1993b) Competing metal ion influences on chromium (III) oxidation by birnessite. *Soil Sci. Soc. Am. J.* **57**, 1508-1515.

Fujiwara M., Matsushita T., and Ikeda S. (1995) Evaluation of Mn3s X-ray photoelectron spectroscopy for characterization of manganese complexes. *J. Elect. Spectro. Related Phenom.* **74**, 201-206.

Furrer G. and Stumm W. (1986) A coordination chemical approach to the kinetics of weathering: I. dissolution of oxides; case studies on δ-Al_2O_3 and BeO. *Geochim. Cosmochim. Acta* **50**, 1847-1860.

Gerischer H. (1978) Electrochemistry of the excited state. *J. Electrochem. Soc.* **125**, 218c-226c.

Goldstein J. I., Newbury D. E., Echlin P., Joy D., Romig A. D. J., Lyman C. E., Fiori C., and Lifshin E. (1992) *Scanning electron microscopy and X-ray microanalysis*. Plenum Press.

Gupta R. P., Sen, S.K. (1974) Calculations of multiplet structure of core p-vacancy levels. *Phys. Rev. B* **10**, 71-79.

Gupta R. P., Sen, S.K. (1975) Calculation of multiplet structure of p-vacancy levels II. *Phys. Rev. B* **12**, 15-19.

Hem J. D. (1964) Deposition and solution of manganese oxides. *United States Geological Society Water Supply Paper*. **1667-B**, B1-B42.

Jenne E. A. (1968) Controls on Mn, Fe, Co, Ni, Cu, and Zn concentrations in soils and water: The significant role of hydrous Mn and Fe oxides. *Trace Inorganics in Water*. **73**, 337-387.

Johnson C. A. and Xyla A. G. (1991) The oxidation of chromium(III) to chromium(VI) on the surface of manganite (γ-MnOOH). *Geochim. Cosmochim. Acta* **55**, 2861-2866.

Johnsson P. A., Eggleston C. M., and Hochella M., F. Jr. (1991) Imaging the molecular-scale structure and microtopography of hematite with the atomic force microscope. *Amer. Mineral.* **76**, 1442-1445.

Junta J. L. and Hochella M. F., Jr.;. (1994) Manganese(II) oxidation at mineral surfaces: a microscopic and spectroscopic study. *Geochim. Cosmochim. Acta* **58**, 4985-4999.

Kavanaugh M. C. (1994) *Alternative for Groundwater Cleanup*. National Academy Press.

Kim J. G. and Moon H.-S. (1998) Oxidation of chromium (III) to chromium (VI) by a series of synthesized birnessites (δ-MnO_2): Kinetics and oxidation capacity. *Clay Sci*. **10**, 363-373.

Leckie J. O., Appleton A. R., Ball W. B., Hayes K. F., and Honeyman B. O. (1984) Report 910.1. Electric Power Research Institute.

Lindsay W. L. (1979) *Chemical equilibria in soils*. John Wiley and Sons.

Malati M. A. and Rophael M. W. (1999) Radiochemical and physicochemical characterization of manganese oxides. *Surf. Sci.* **433**, 740-744.

Manceau A. and Charlet L. (1992) X-Ray absorption spectroscopy study of the sorption of Cr(III) at the oxide-water interface I. Molecular mechanisms of Cr(III) oxidation by Mn oxides. *J. Col. Interface Sci*. **148**, 425-442.

Manceau A. and L. C. (1990) In-Situ X-Ray absorption study of the mechanism of Cr(III) oxidation at the Mn oxide/water interface. *Geochemistry of the Earth's Surface and of Mineral Formation 2nd International Symposium*, 275-278.

Marcus R. A. (1965) Theory of electron-transfer reaction rates of solvated electrons. *J. Chem. Phys.* **43**(10), 3477-89.

McKenzie R. M. (1971) The synthesis of birnessite, cryptomelane and some other oxides and hydroxides of manganese. *Mineral. Mag.* **38**, 493-502.

McKenzie R. M. (1980) The manganese oxides in soils. In *The Geology and Geochemistry of Manganese: Volume 1. General Problems. Mineralogy, Geochemistry, Methods.*, **1** (eds. I. M. Varentsov and G. Grasselly), 259-269.

Means J. L. C., D.A.; Borcsik, M.P.; Duguid, J.O. (1978) Radionuclide adsorption by manganese oxides and implications for radioactive waste disposal. *Nature*. **274**, 44-47.

Merkle P. B., Knocke W., Gallagher D., Junta-Rosso J. L., and Solberg T. (1996) Characterizing filter media mineral coatings. *J. Amer. Water Works Association* **88**, 62-73.

Morrison R. S. (1980) *Electrochemistry at semiconductor and oxidized metal electrodes*. Plenum.p. 401

Moulder J. F., Stickle W. F., Sobel P. E., and Bomben K. D. (1995) *Handbook of x-ray photoelectron spectroscopy*. Physical Electronics, Inc.

Murray J. W. (1974) The surface chemistry of hydrous manganese oxide. *J. Col. Interface Sci.* **46**, 357-371.

Murray J. W. (1975) The interaction of metal ions at the manganese dioxide-solution interface. *Geochim. Cosmochim. Acta* **39**, 505-519.

Nielsen A. E. (1964) *Kinetics of precipitation*. Pergamon Press.

Nozik A. J. and Memming R. (1996) Physical Chemistry of Semiconductor-Liquid Interfaces. *J. Phys. Chem.* **100**, 13061-13078.

Nriagu J. O., Nieboer E. (1988) Advances in Environmental Science and Technology, **20** Chromium in the Natural and Human Environments, p. 571

Palenik G. J. (1997) Bond valence sums in coordination chemistry using oxidation state independent Ro values. A simple method for calculating the oxidation state of manganese in complexes containing only Mn-O bonds. *Inorg. Chem.* **36**, 4888-4890.

Pauling L. and Kamb B. (1982) The crystal structure of lithiophorite. *Amer.Mineral.* **67**, 817-821.

Pollard J. H. (1977) *A handbook of numerical and statistical techniques with examples mainly from the life sciences*. Cambridge University Press.

Post J. E. (1992) Crystal structures of manganese oxide minerals. *Catena supplement* **21**, 51-73.

Post J. E. and Appleman D. E. (1994) Crystal structure refinement of lithiophorite. *Amer. Mineral.* **79**, 370-374.

Pourbaix M. (1974) *Atlas of electrochemical equilibria*. National Association of Corrosion Engineers.

Ross D. S., Hales H. C., Shea-McCarthy G. C., and Lanzirotti A. (2001) Sensitivity of soil manganese oxides: drying and storage cause reduction. *Soil Sci. Society America* **65**, 736-743.

Samsonov G. (1982) *The oxide handbook*. Plenum.

Schroeder D. C. and Lee G. F. (1975) Potential transformations of chromium in natural waters. *Water, Air, Soil Pollution* **4**, 355-365.

Shannon R. D. (1976) Revised effective radii and systematic studies of interatomic distances in halides and chalcogenides. *Acta Cryst.* **A32**, 751-767.

Shuey R. T. (1975) *Semiconducting Ore Minerals*. Elsevier p. 415

Silvester E. C., Laurent; Manceau, Alain. (1995) Mechanism of Chromium(III) Oxidation by Na-Buserite. *J.Phys. Chem.* **99**, 16662-16669.

Singh S. K. S., V. (1984) Hydrous Fe and Mn oxides- Scavengers of heavy metals in the aquatic environment. *CRC Critical Reviews Environ. Control* **14**, 33-90.

Stone A. T. and Morgan J. J. (1987) Reductive dissolution of metal oxides. *Aquatic Surface Chemistry- Chemical Processes at the Particle-Water Interface* (ed. W. Stumm), John Wiley & Sons p. 221-254

Stumm W. (1992) Chemistry of the Solid-Water Interface: Processes at the Mineral-Water and Particle-Water Interface in Natural Systems, p. 428.

Stumm W. and Furrer G. (1987) The dissolution of oxides and aluminum silicates; examples of surface-coordination-controlled kinetics. *Aquatic Surf. Chem.*, 197-219.

Stumm W. and Wieland E. (1990) Dissolution of oxide and silicate minerals: rates depend on surface speciation. *Aquatic Chemical Kinetics: Reaction Rates of Processes in Natural Waters* (ed. W. Stumm), Wiley, p. 545.

Stumm W. and Morgan J. J. (1996) *Aquatic Chemistry- Chemical equilibria and rates in natural waters*. John Wiley and Sons

Van Der Weijden C. D. and Reith M. (1982) Chromium(III)-Chromium(VI) interconversions in seawater. *Marine Chemistry* **11**, 565-572.

Wadsley A. D. (1952) The structure of lithiophorite (Al,Li)$MnO_2(OH)_2$. *Acta Cryst.* **5**, 676-680.

Weaver, R.M. and Hochella, M. F. Jr., (accepted) Dynamic processes at the manganite-Cr^{III}_{aq} interface: simultaneous adsorption, dissolution and microprecipitation. *Geochim. et. Cosmochim. Acta*

Weaver, R.M. (2001) A comparison between the reactivity of various Mn-oxides with Cr^{III}_{aq}: microscopic and spectroscopic observations of dissolution, Cr-sorption and Cr and Mn redox interactions, Ph.D. Dissertation, Virginia Polytechnic Institute and State University

Wemple S. and Didomenico D. (1969) Oxygen-octahedra ferroelectrics. II. Electrooptical and nonlinear-optical device applications. *J. Appl. Phys.* **40**, 735

Wehrli B. (1990) Redox reactions of metal ions at mineral surfaces. *Aquatic Chemical Kinetics: Reaction Rates of Processes in Natural Waters* (ed. W. Stumm), Wiley, p. 545

12. CHAPTER 2: Tables and Figures

Table 1. Summary of chemical and structural properties of the Mn-oxides used in this study.

Mineral	Sample	Structure[a]	Formula	EDS[b] Minor <10%	EDS[b] Trace <1%	BET[c] A_s (m^2/g)	refs.[d] ~PZC[a]	ave.Mn^{z+}	CN	σ[e]	σ/ l[f]
Hausmannite	VPI #ha142	framework	$Mn^{2+}(Mn^{3+})_2O_4$	Ba	Ba, Al, Si	9.12 2.06	< 5.0	2.67	Mn^{2+} = 4 Mn^{3+} = 6	1/2 1/2	2.29 2.51
Manganite γ-MnOOH	VPI #ma6	1x1 tunnel	$Mn^{3+}OOH$	Al	Si, Na	6.09	5.5	3.0	Mn^{3+} = 6	1/2	2.51
Romanechite w/out Ba (impure)	VPI #rom2	2x3 tunnel	$Ba_{0.66}Mn^{4+}_{3.68}Mn^{3+}_{1.32}O_{10}\cdot nH_2O$	Si, Al	K, Na, Mg	19.32	unknown	3.73 ±0.1	Mn^{3+} = 6 Mn^{4+} = 6	1/2 2/3	2.51 3.55
Birnessite (syn.) δ-MnO_2	VPI #bi1	layer	$K_2(Mn^{4+}_{0.75},Mn^{3+}_{0.2},Mn^{2+}_{0.05})_{14}O_{27}\cdot 9H_2O$		Na, Si	35.35	2	3.7 ±0.1	Mn^{2+} = 6 Mn^{3+} = 6 Mn^{4+} = 6	1/3 1/2 2/3	1.53 2.51 3.55
Cryptomelane α-MnO_2	VPI #cr2	2x2 tunnel	$K(Mn^{4+}Mn^{3+})_8O_{16}\cdot nH_2O$	Al, Si, K	Na,Ba	14.89	4.5 ±0.5	3.8 ±0.1	Mn^{3+} = 6 Mn^{4+} = 6	1/2 2/3	2.51 3.55
Lithiophorite	NMNH #141948	layer	$LiAl_2\ Mn_{2.52}{}^{4+},Mn_{0.48}{}^{3+}O_6\ (OH)_6$		Mg	8 (est.)	unknown	3.84 ±0.1	Mn^{3+} = 6 Mn^{4+} = 6	2/3 2/3	2.51 3.55
Pyrolusite β-MnO_2	VPI #py8	1x1 tunnel	$Mn^{4+}O_2$	Si	Al	7.86 6.6	7.3	4.0	Mn^{4+} = 6	2/3	3.55

a) The "#" x "#" description of the tunnel denotes the tunnel dimension in units of Mn-octahedra. For example, romanechite has tunnels that are two Mn-octahedra wide by three Mn-octahedra long. Each Mn-octahedra measures approximately 0.22 nm on edge (Post, 1992).

b) EDS was performed with a Kevex light element (>Z = 5) detector mounted on a LEO 1550 FESEM. The EDS detector and quantitative elemental analysis software were calibrated for operation at the conditions of our data collection (e.g. 20kV accelerating voltage, 10 mm working distance, 35° take off angle). The spectra were collected at a low magnification (~1000x, size of irradiated area ~0.02 mm^2), on micronized samples in order to obtain an area averaged chemical composition. Chemical analyses from smaller areas of cleavage or fracture surfaces typically showed less minor and trace elements. To ensure a good detection limit, ~200,000 counts were collected on each spectra. To minimize peak broadening the detector was operated with less than 15% dead time.

c) BET surface area measurements were performed using N^2 as adsorbent using a Quantachrome Nova1000. Samples were degassed at 40°C. For the Mn-oxides with two reported surface areas, the lower one was measured on a 840-250 μm size fraction. The surface area of lithiophorite was estimated (see text).

d) Where possible the values of the PZC were taken from the literature. Cryptomelane, pyrolusite, birnessite (Healy, 1966), manganite (Weaver and Hochella, in review), hausmannite, lithiophorite, romanechite (not reported).

e) σ denotes the Pauling bond strength. σ = valence/ coordination number.

f) σ divided by bond length (l). This parameter allows relative bond strength comparisons to be made between the different Mn-oxides. The Mn^{2+}-O, Mn^{3+}-O and Mn^{4+}-O bond lengths of 0.223 nm 0.204 nm and 0.189 nm respectively, were taken from Shannon (1976) and are a very close approximation of the average Mn-O bond lengths calculated from X-ray diffraction measurements for each of the minerals

Table 2. Summary of acidic and reductive dissolution reactions for hausmannite, manganite and pyrolusite.

Acidic dissolution reaction

		Q, at 260 hrs[1]	log Q	log K[2]	S.I.[3]	ΔG^o_R (kJ/mol)
hausmannite	$Mn_3O_4 + 8H^+ + 2e^- = 3Mn^{2+} + 4H_2O$	$(1.167E^{-3})^3/(10^{-5.2})^8$	32.8	63.03	0.52	-349.6
manganite	γ-$MnOOH + 3H^+ + e^- = Mn^{2+} + 2H_2O$	$1.297E^{-4}$M/$(10^{-4.4})^3$	9.3	25.27	0.37	-144.7
pyrolusite	β-$MnO_2 + 4H^+ + 2e^- = Mn^{2+} + 2H_2O$	$8.725E^{-5}$ M/$(10^{-4.4})^4$	13.5	41.89	0.32	-237.2

Reductive dissolution and $CrOH^{2+}_{aq}$ oxidation reaction			ΔG^o_R (kJ/mol)	Mn_{aq}:Cr^{VI}_{aq}
hausmannite[4]	$1.5Mn_3O_4 + CrOH^{2+}_{aq}$	$= 1.5Mn^{2+(A)} + 3Mn^{2+} + HCrO_4^- + 1.5O_2 + 6e^-$	575.0	$4.5^{(R+A)}$, $3.0^{(R)}$
manganite	3γ-$MnOOH + CrOH^{2+}_{aq}$	$= 3Mn^{2+} + HCrO_4^- + 3OH^-$	171.9	3
pyrolusite	1.5β-$MnO_2 + CrOH^{2+}_{aq}$	$= 1.5Mn^{2+} + HCrO_4^-$	13.2	1.5

Footnotes:

1. Q is the reaction quotient or ion activity product (IAP) (Stumm and Morgan, 1996). The Mn_{aq} concentrations at 260 hrs as reported in Appendix 1(Weaver, 2001) were multiplied by the Mn-oxide surface area (Table 1) to obtain molar quantities.
2. log K is the equilibrium constant calculated from $\Delta G^o_R = -RT \ln K$. These values were obtained from Lindsay, 1979.
3. Saturation index (SI) is equal to Q/K and is a measure of the degree of saturation of a solution with respect to a solid phase. SI < 1 is undersaturated, SI >1 is supersaturated.
4. For the reductive dissolution of hausmannite the Mn^{2+} sites in the lattice cannot be reduced, yet because they are highly soluble they would contribute to the overall Mn^{2+}_{aq} products. These acidically dissolved Mn^{2+}aq ions are explicitly listed in the reaction as $Mn^{2+(A)}$. The two Mn_{aq}:Cr^{VI}_{aq} ratios correspond to the case in which the $Mn^{2+(A)}$ is considered and where only the reductively dissolved Mn is considered.

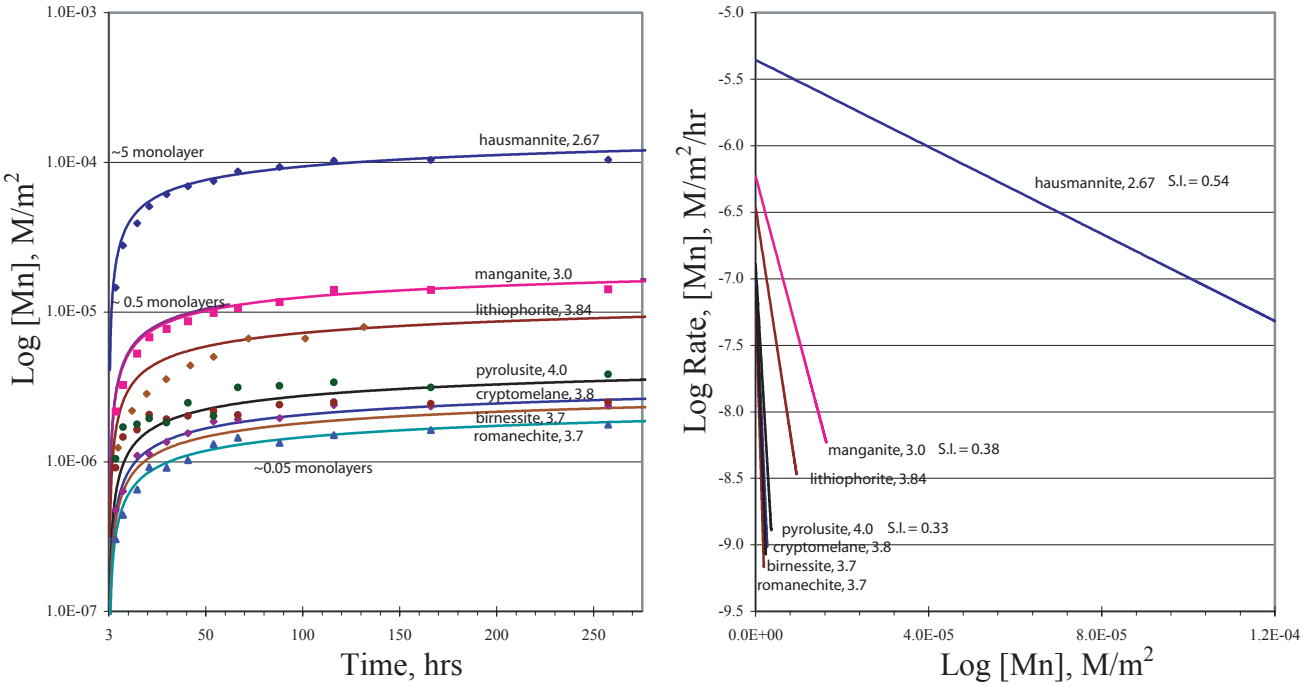

Figure 1. a) Acidic release of manganese from each Mn-oxide versus time. The lines show the fits to the data and are labelled with the mineral name and average Mn oxidation state. Note that the Mn_{aq} concentrations at time 3 hr. were normalized to zero, but this point cannot be displayed in the log scale. Estimates for the corresponding number of monolayers dissolved are given at different Mn concentrations. b) Mn-oxide dissolution rate versus $[Mn]_{aq}$. Dissolution rates are seen to be much more rapid for the lower valence Mn-oxides (e.g. hausmannite) at any given $[Mn]_{aq}$. Saturation indices (SI) are given for the three simple oxides, hausmannite, manganite and pyrolusite at time equals 260 hr. (see Table 2). These trends suggest that $[Mn]_{aq}$ does not inhibit dissolution at these concentrations.

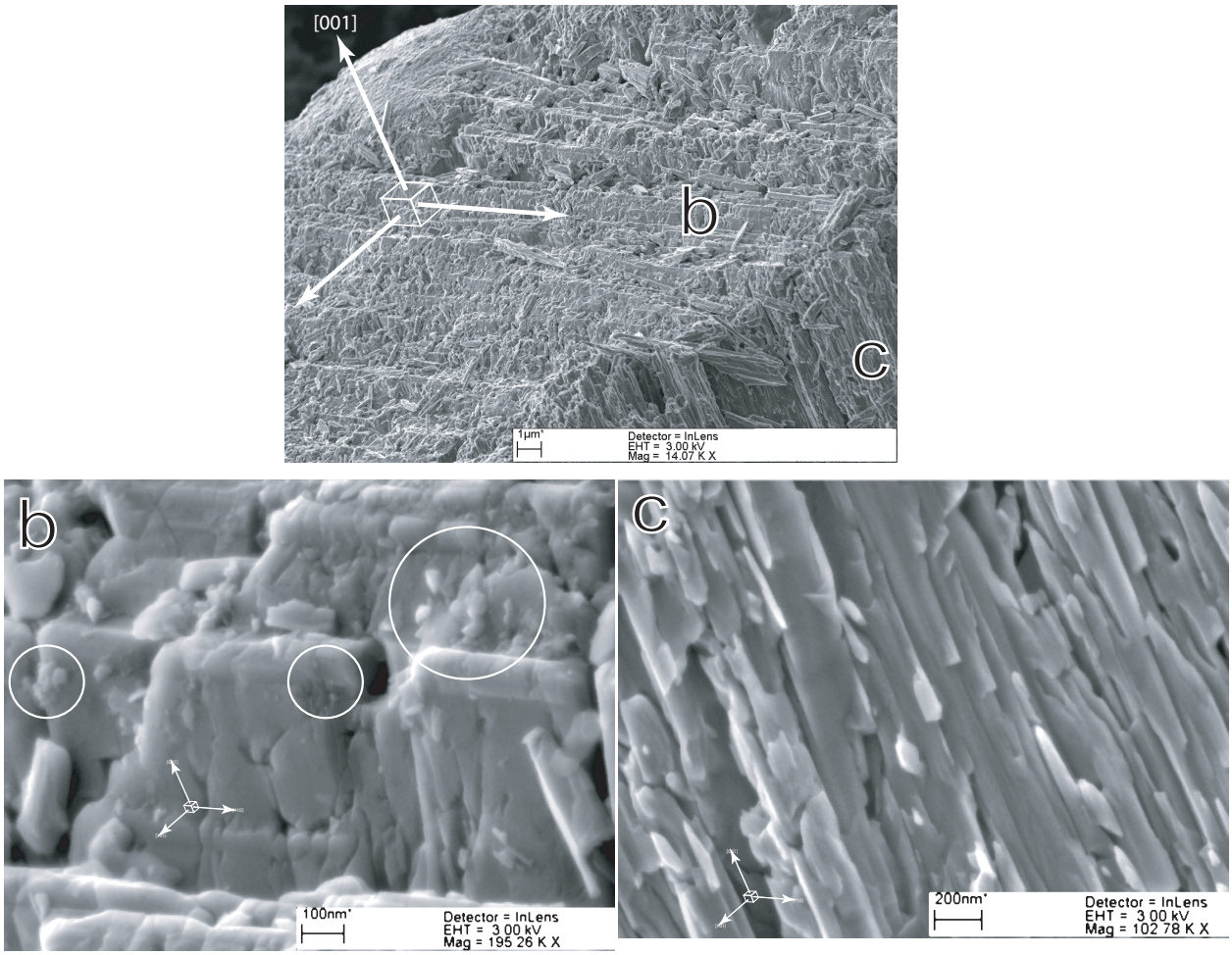

Figure 2. FESEM images of pyrolusite after ~80 hrs of reaction with pH 4.5, 10^{-4} M $CrOH^{2+}_{aq}$. (a) morphology is generally rougher on the (001) termination 'b' compared to the prismatic surfaces 'c'. 'b' and 'c' show locations of images (b) and (c). (b) and (c) Some rounding of the topographic features is apparent, though the amount of surface dissolution estimated from surface area and $[Mn]_{aq}$ measurements is <1 monolayer. Fine debris (possibly Cr-precipitates, circled) are more frequently present on the (b) surfaces compared to the smoother prismatic (c) surfaces. XPS always showed Cr signal on reacted pyrolusite surfaces, however Cr was never detected by EDS. Pyrolusite is reported to exhibit 1 plane of cleavage, whereas there are at least two planes of cleavage visible in these micrographs. This probably indicates that this sample is a pseudomorph, possibly after manganite.

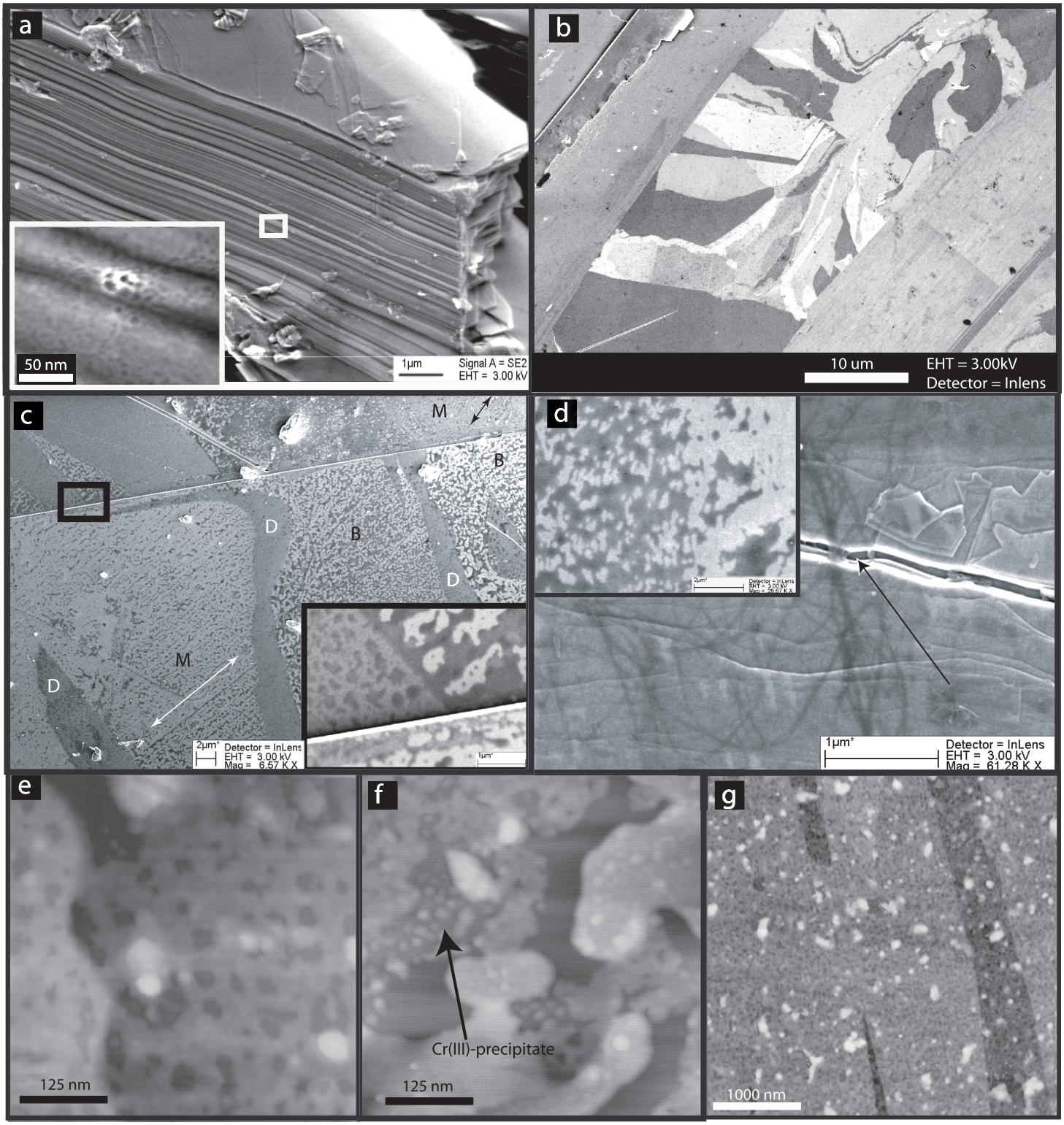

Figure 3. a-d) FESEM images, e-g) TMAFM images of lithiophorite. a) Layer morphology apparent, reacted for 1 hr in pH 4.4 HNO_3. Inset show dissolution pits on the edges of the basal (001) plane. b) Unreacted surface showing variable contrast, probably due to near surface atomic number contrast (i.e dark areas have lower average atomic number, probably Li and/or Al rich). c) Reacted for 1 hr in pH 4.4, 10^{-4} M $CrOH^{2+}_{aq}$. The extent of pitting varies spatially with respect to contrast mechanism seen in (b), with the bright (B) areas showing more extensive dissolution than the medium (M) or dark (D) areas. Arrows mark examples of strong dissolution anisotropy. Inset shows dissolution pits on three adjacent terraces. d) Images from within 20µM of the perimeter of the interior surface after reaction for 13 hr in pH 4.4, 10^{-4} M $CrOH^{2+}_{aq}$, showing a sinuous solid phase (cross-cuts and drapes into crevice, at arrow). Inset shows gray patches which contain a darker solid phase, presumably Cr-containing. Darkness may result from positive charging or lower atomic number. e, f) Fluid cell TMAFM images after exposure to (e) pH 4.4 HNO_3,10 min and (f) pH 4.4, 10^{-4} M $CrOH^{2+}_{aq}$. In both, pits are 1-4 nm deep. In (f) small mounds (~0.5 -2.0 nm high) are presumably Cr-phase. G) Image showing distribution of Cr-ppt (bright spots, 1 -20 nm high). Pits uniformly cover the surface. Before reaction the surfaces were locally of near atomic flatness and contained no pits or particles.

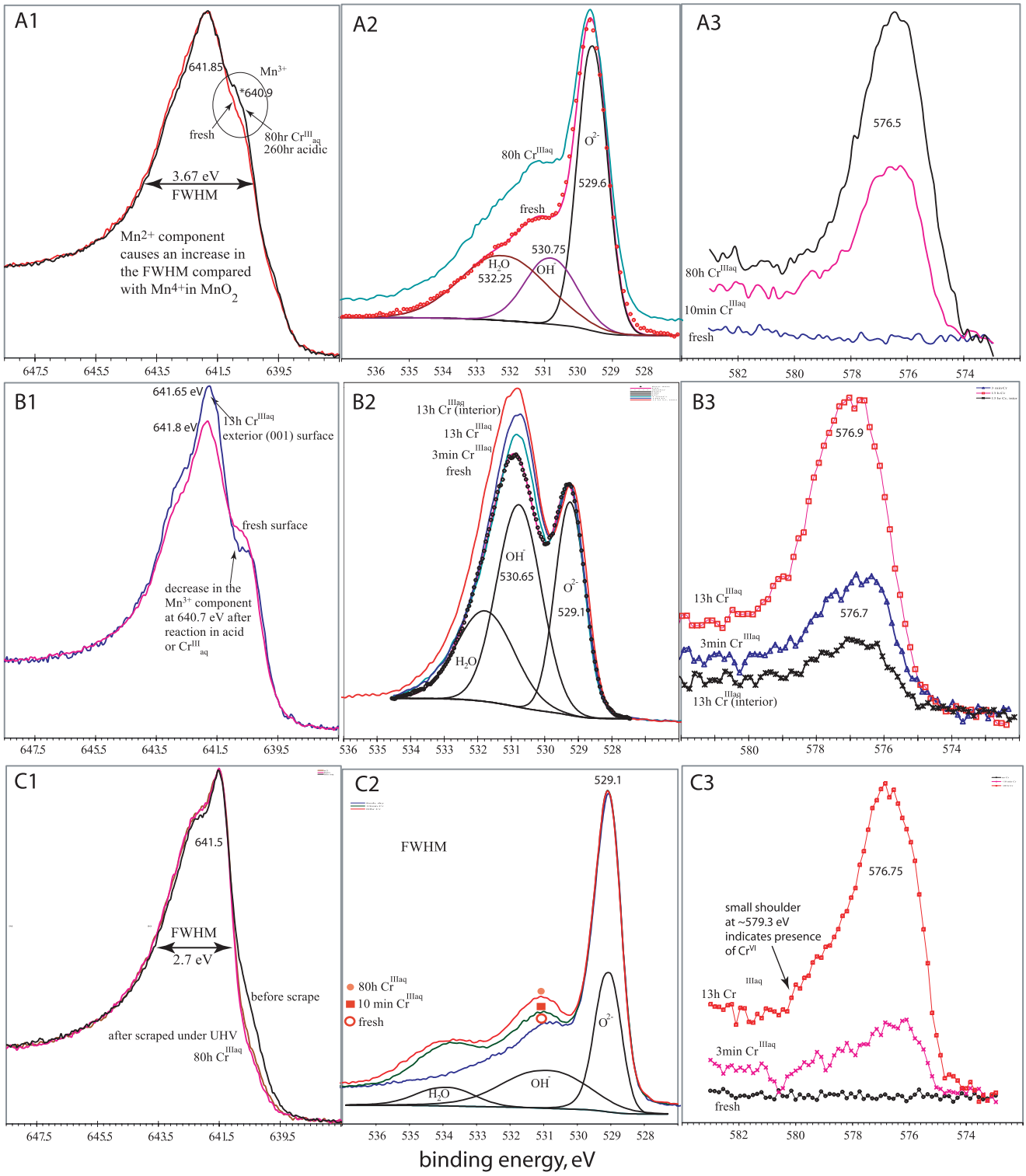

Figure 4. $Mn2p^{3/2}$, O1s and $Cr2p^{3/2}$ XPS spectra for A) hausmannite, B) lithiophorite and C) pyrolusite after various types of treatments (see legend in each plot for experimental conditions).

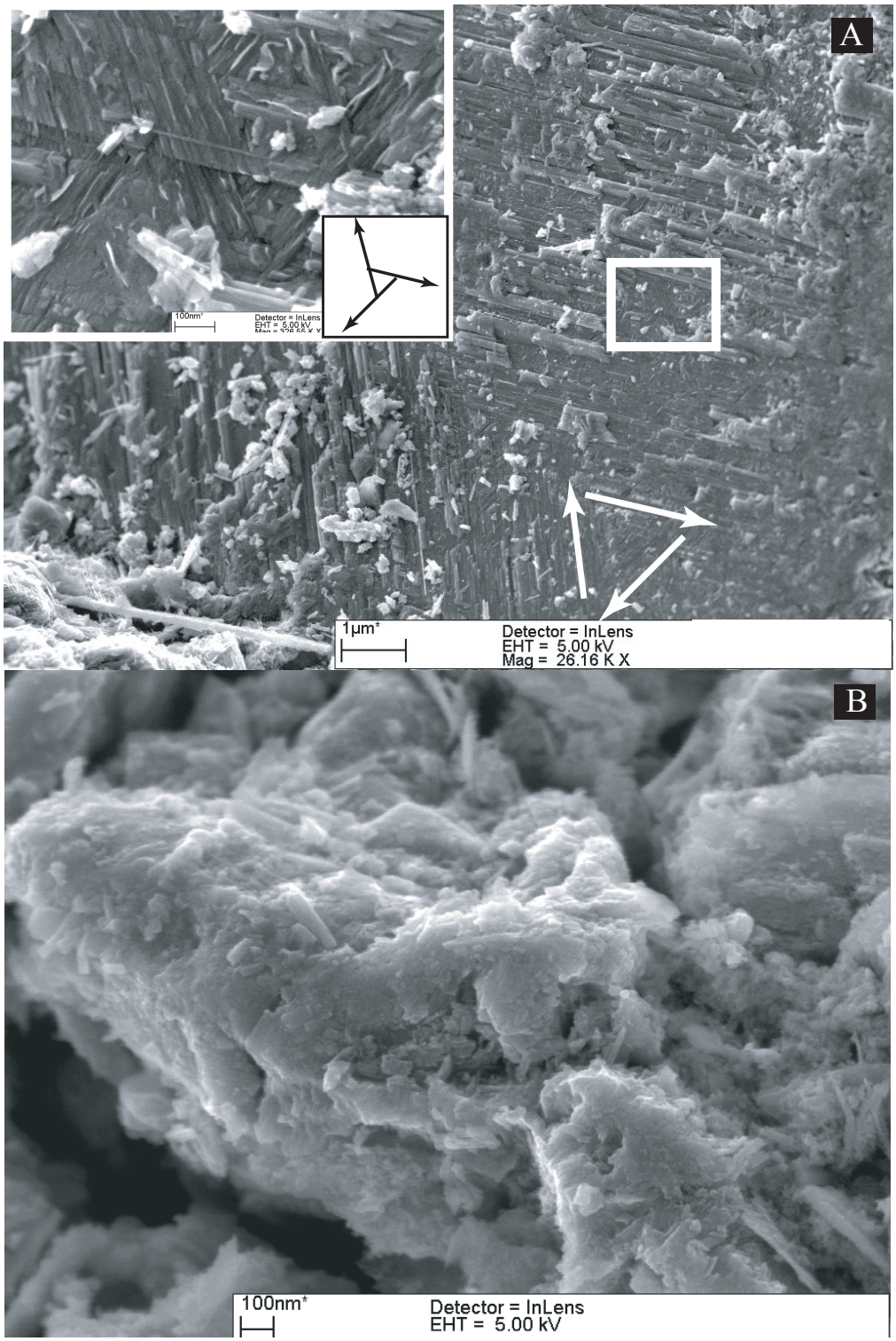

Figure 5. FESEM images of hausmannite after reaction with pH 5.2, 10^{-4} M Cr^{III}_{aq}, for 10 hr. Images a) and b) depict the two typical types of surface morphologies seen after acidic or reductive dissolution. a) Extensive and anisotropic dissolution produces a surface with intersecting ridges which parallel crystallographic directions. The inset shows a surface with three set of ridges directed 120 degrees relative to each other. Hausmannite is tetragonal and should not exhibit a hexagonal etching pattern, unless it is a pseudomorph. b) Randomly dissolved surface covered with particles that probably contain some sorbed or precipitated chromium. XPS spectra of hausmannite reacted under these conditions always showed Cr. Under these conditions, it is likely that both homogeneous and surface-catalyzed precipitation of Cr-hydroxyhydrate is occurring.

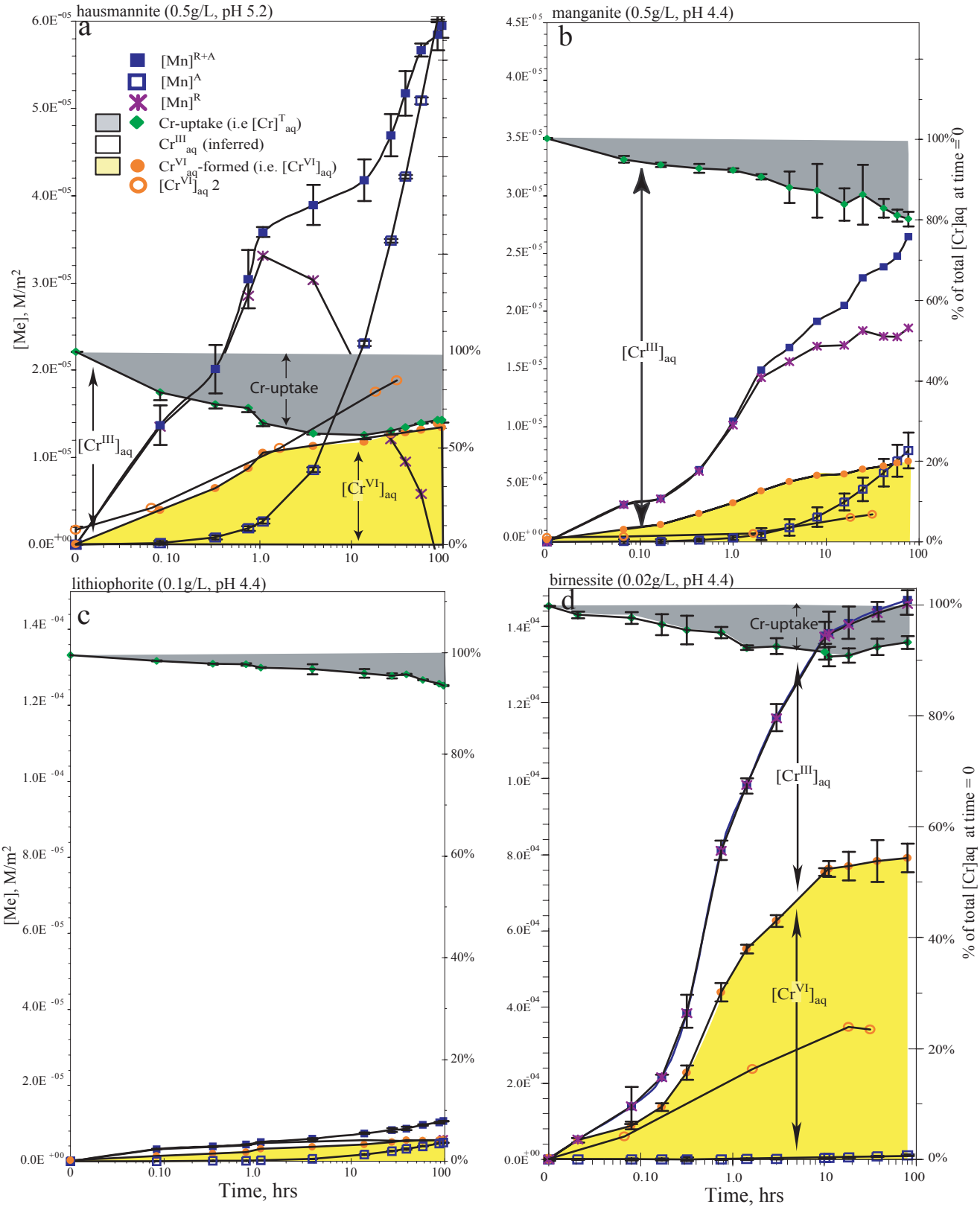

Figure 6. a-h) Batch reactor data for reductive dissolution of Mn-oxides. Aqueous Cr and Mn concentrations are normalized to surface area. The percent scale on the right side y-axis only applies to the chromium concentrations. On this scale, 100% corresponds to the initial $[Cr^{III}]_{aq}$ (i.e. 10^{-4} M). Shading is used to illustrate the relative amounts of each form of chromium as a function of time. The dark gray 'Cr-uptake' region illustrates the amount of Cr removed from solution (i.e. $[Cr]^{T}_{aq}$, ICP data, diamonds). The light gray region illustrates $[Cr^{VI}]_{aq}$. The intervening unshaded region illustrates the amount of CrIIIaq still available for oxidation. The open circles show the chromate produced when the Mn-oxide was reacted a second time in fresh Cr^{III}_{aq} (Note, no results for c or e). The errors bars show plus or minus one S.D. of the mean for the three replicate runs, not analytical uncertainty. (Figure continued on next page).

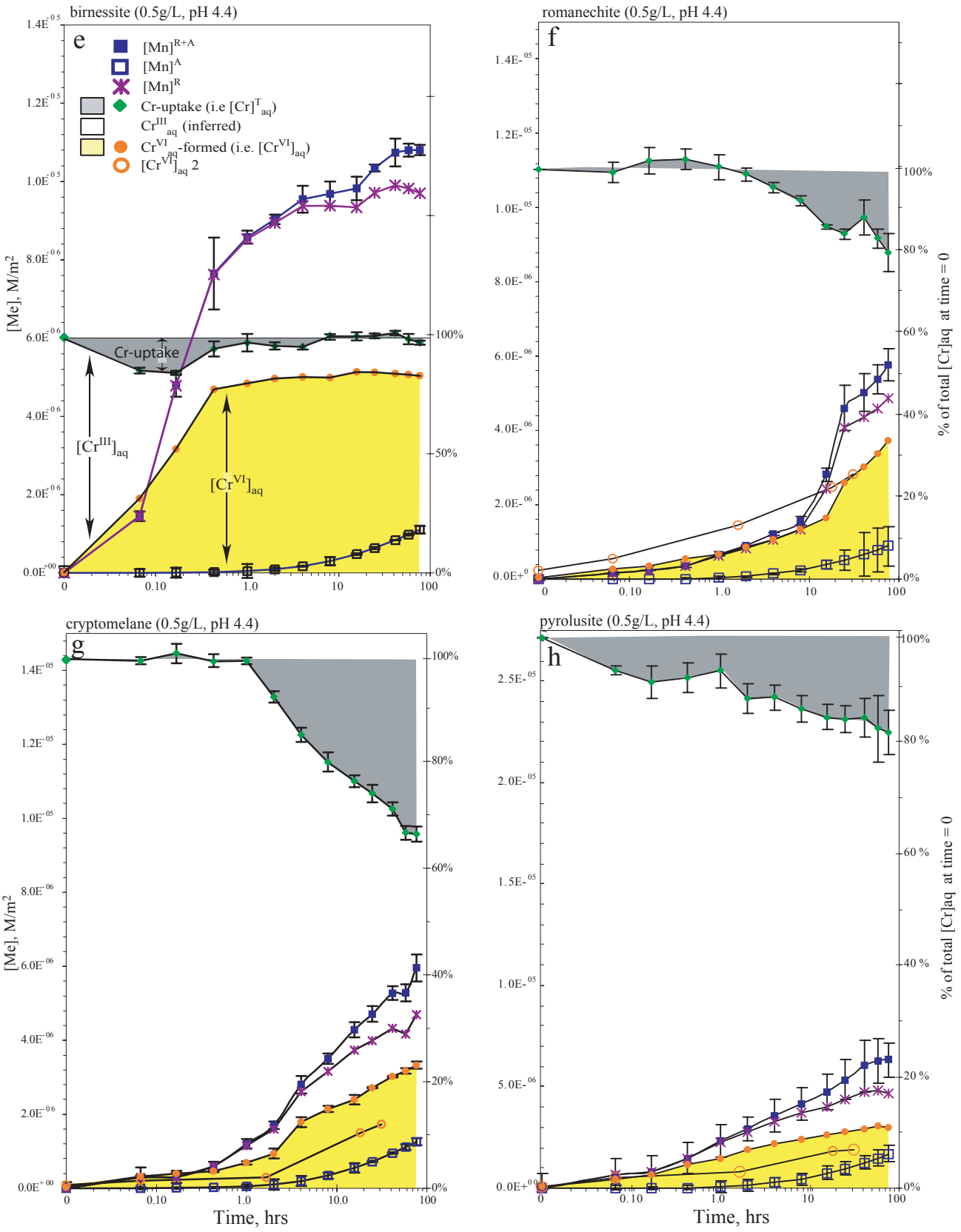

Figure 6 (conti.)

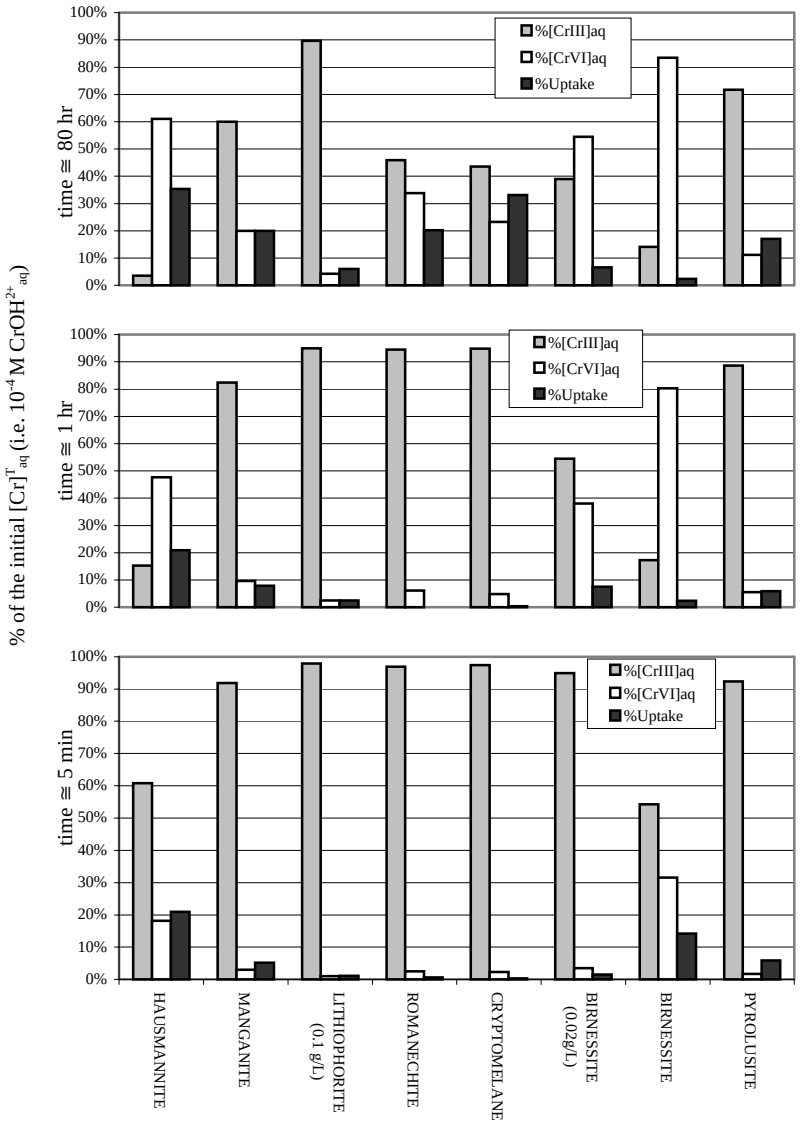

Figure 7. Relative amounts of chromium occurring as Cr^{III}_{aq}, Cr^{VI}_{aq} or removed from solution by uptake onto the Mn-oxide surface for three different times (i.e. 5 min, 1 hr and 80 hr). For example, it can be seen that at time = 5 min, hausmannite has already oxidized ~20% of the initial Cr^{III}_{aq} to Cr^{VI}_{aq}, there was ~20% uptake and ~60% still occurs as Cr^{III}_{aq}. After 80 hr, 60% of the initial Cr^{III}_{aq} has been oxidized to Cr^{VI}, ~35% is missing (i.e. sorbed or precipitated) and ~5% still occurs as Cr^{III}_{aq}.

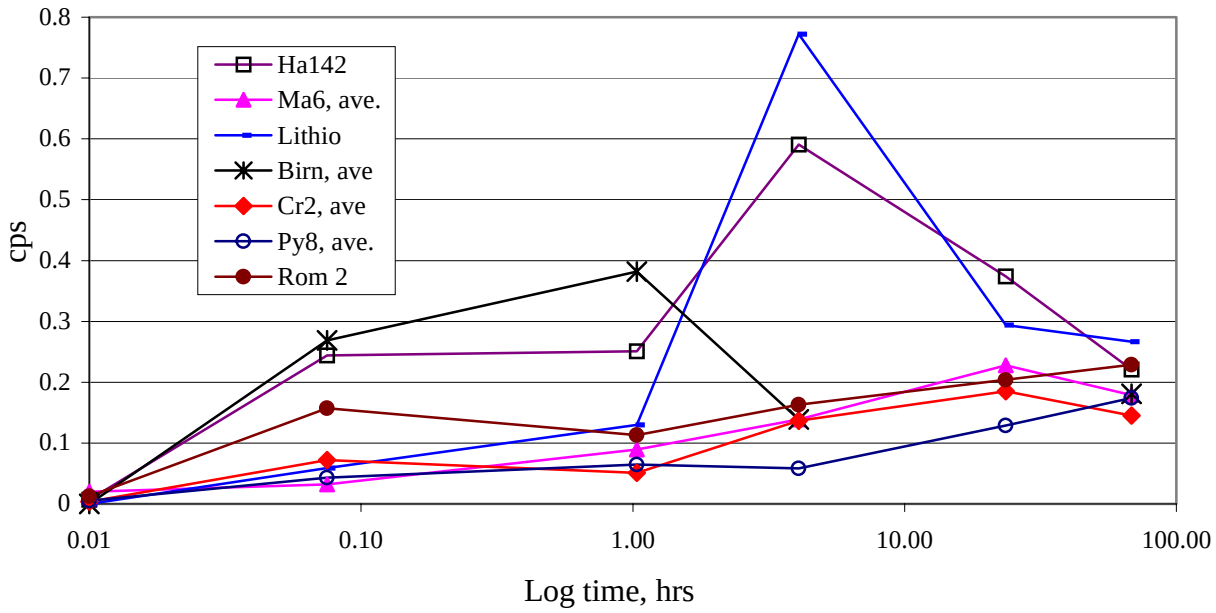

Figure 8. The relative amounts of chromium present on the different Mn-oxides as a function of time, as measured by WDS. The relative concentrations are in qualitative agreement with the concentrations expected from the total aqueous chromium data. Note that the chromium concentrations of hausmannite and the layer Mn-oxides (i.e. birnessite and lithiophorite), are generally higher and also show a subsequent decrease probably due to desorption (see discussion). All of the other Mn-oxides show a gradual increase in chromium. Chromium concentrations on unreacted samples were below the detection limit of ~0.03 weight percent and uncertainty was ± 0.05 cps.

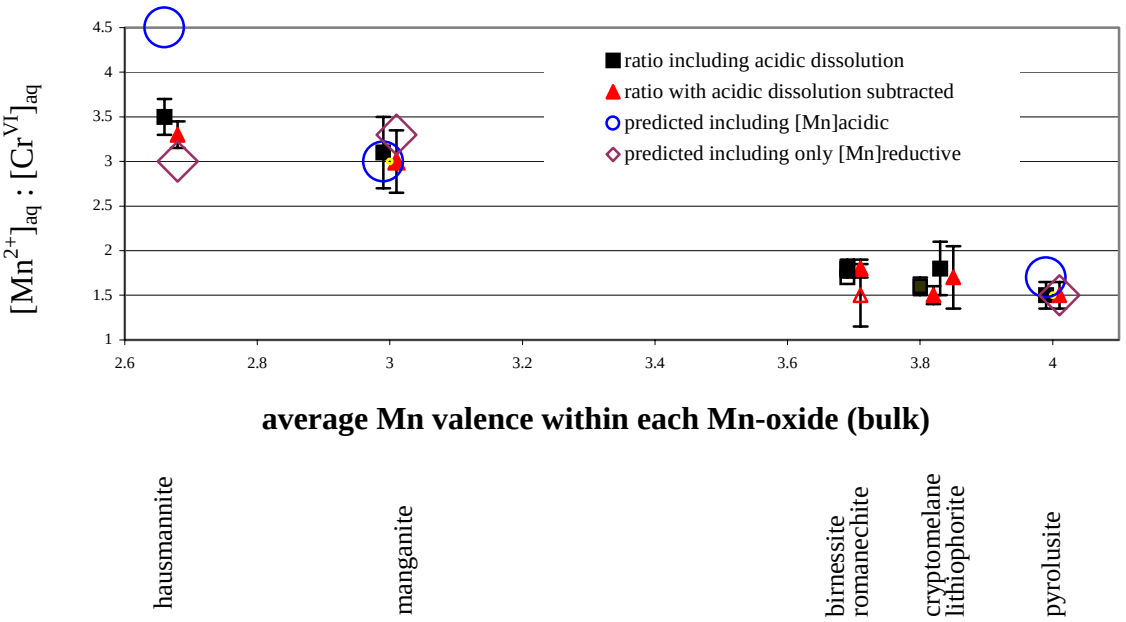

Figure 9. Comparison of experimentally measured $[Mn]^{T}_{aq} : [Cr^{VI}]_{aq}$ ratios with ratios predicted from the proposed reaction stoichiometries for hausmannite, manganite and pyrolusite (see Table 2). The ratios are plotted versus the average Mn valence in each Mn-oxide. For each mineral ratios were calculated for the case of neglecting the acidic dissolution (triangles) component and including it (squares). The measured ratios are generally very close to the predicted. Open symbols are used for romanechite to distinguish it from birnessite.

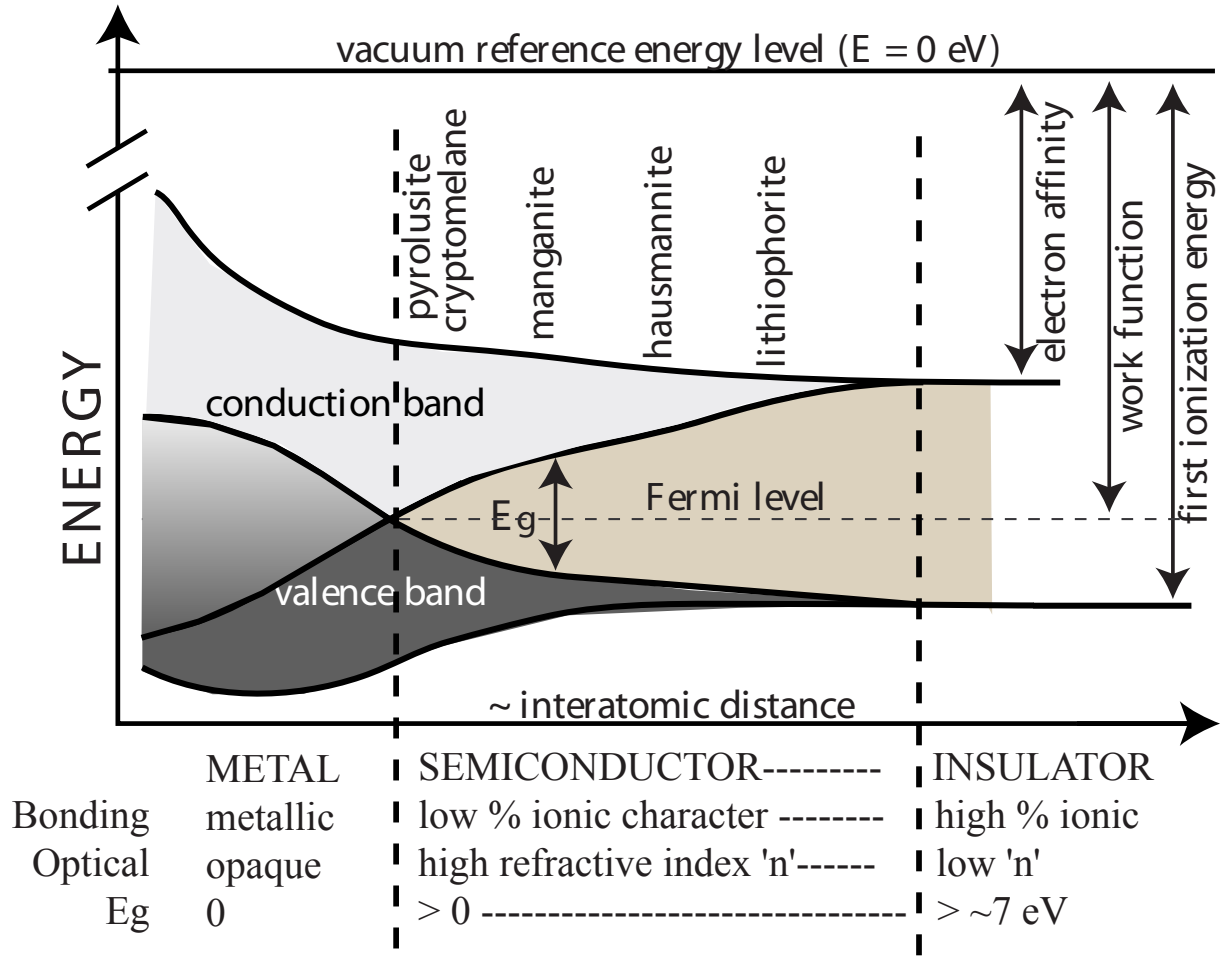

Figure 10. General energy band structure for metals, semiconductors and insulators. Semiconductors and insulators are distinguished from metals in that the valence band (VB) and conduction band (CB) are separated by a band gap (Eg). In a metal where the electrons are highly delocalized (i.e. free to move from nuclei to nuclei) the CB and VB overlap. As a consequence of the band structure there is a corresponding change in the type of bonding, optical and electronic properties. Terminology used for energy transitions between different energy levels is denoted. Mn-oxides are shown in relative positions (modified after Bard and Faulkner, 2001).

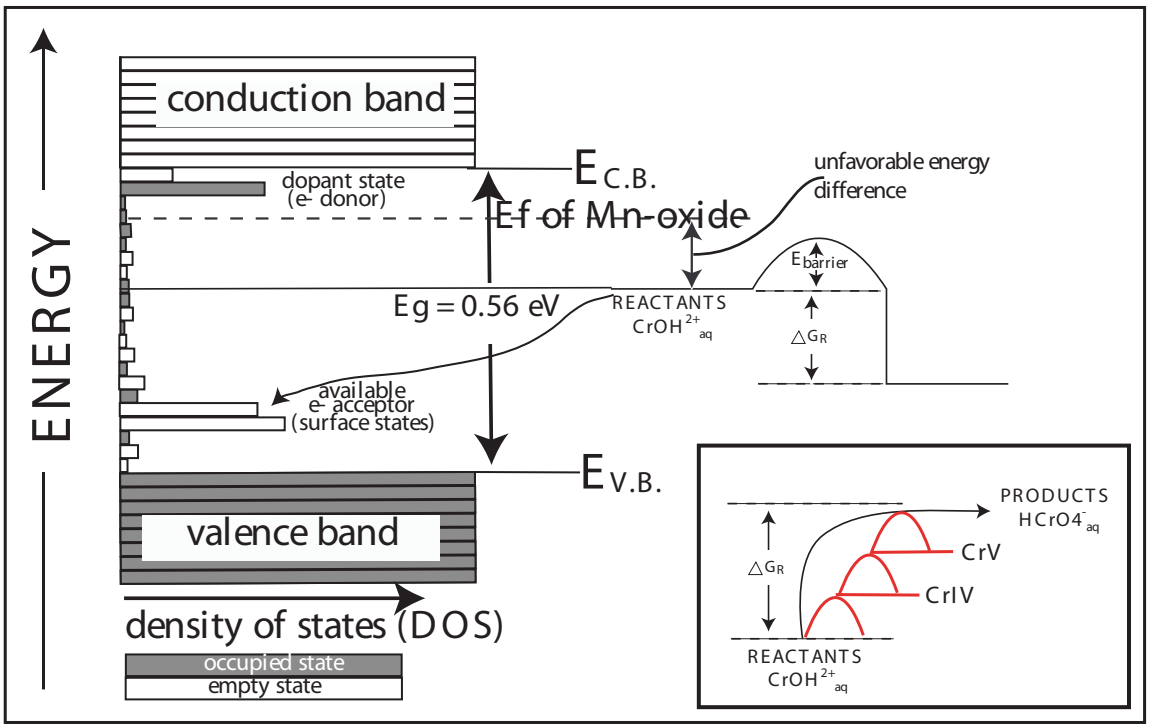

Figure 11. Illustration of a mechanism by which electron transfer may be accomplished between Cr^{III} and a Mn-oxide even if the Fermi level of the Mn-oxide is greater than the redox potential of the Cr^{III}/Cr^{VI} redox couple. If electron acceptor states are present at an energy less than the redox potential then electrons may flow preferentially into these unoccupied states. The inset schematically shows how the redox potential of the Cr^{III}/Cr^{VI} couple may be more accurately depicted as three single electron transfer events.

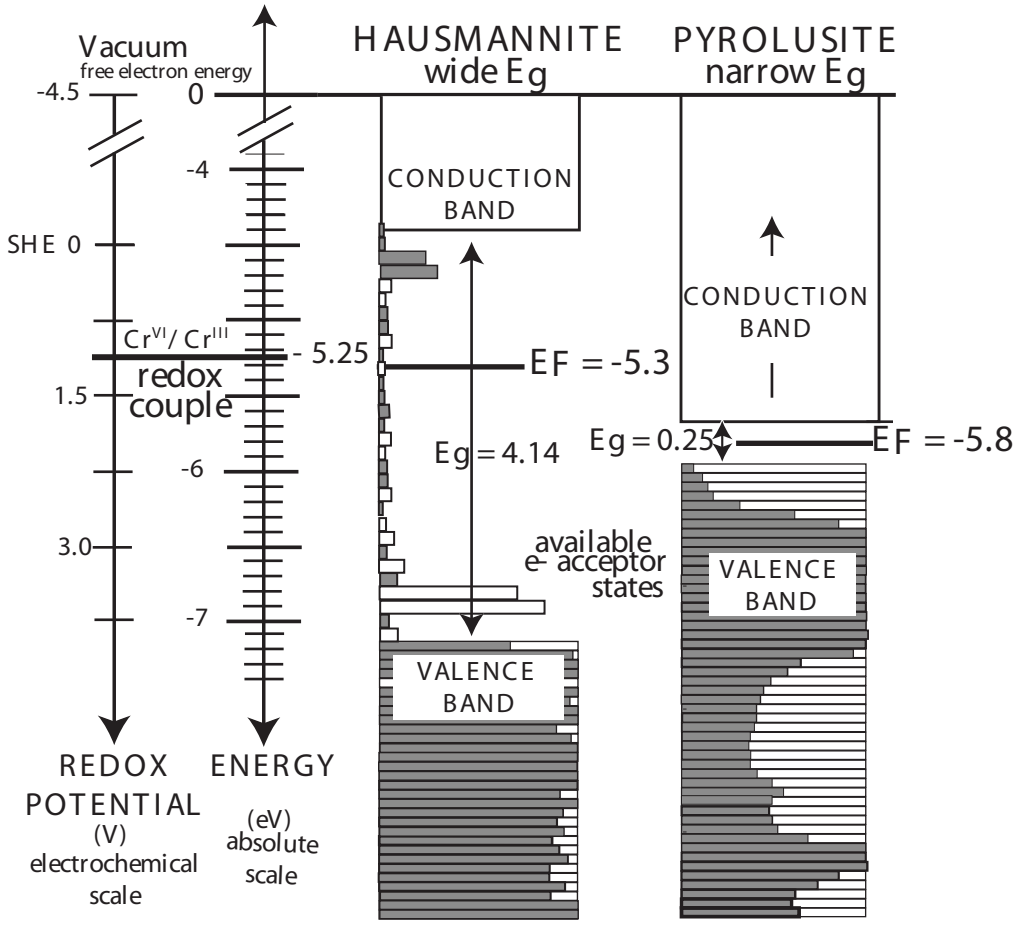

Figure 12. Band diagram showing the energy level of the Cr^{III}/Cr^{VI} redox couple relative to that of the Fermi level of hausmannite and pyrolusite. The Cr^{III}/Cr^{VI} energy (i.e. -5.25 eV) is slightly greater than the Fermi level of hausmannite (-5.3 eV) and significantly greater than the Fermi level of pyrolusite (-5.8 eV). These energy differences suggest that electrons may be spontaneously transferred from Cr^{III} to the Mn-oxide. Depicted in the band structure of hausmannite is a band of available electron acceptor states. Although no direct evidence for these states exists, the experimental results strongly suggests that these states exist and are responsible for the rapid initial and continued oxidation of Cr^{III}_{aq}.